Lack of CCDC146, a ubiquitous centriole and microtubule-associated protein, leads to non-syndromic male infertility in human and mouse

Jana Muroňová[1,2,3,†], Zine-Eddine Kherraf[1,2,3,4,†], Elsa Giordani[1,2,3], Emeline Lambert[1,2,3], Simon Eckert[5], Caroline Cazin[1,2,3,4], Amir Amiri-Yekta[1,2,3,6], Magali Court[1,2,3], Geneviève Chevalier[1,2,3], Guillaume Martinez[1,2,3,7], Yasmine Neirijnck[8], Francoise Kühne[8], Lydia Wehrli[8], Nikolai Klena[9,10], Virginie Hamel[9], Lisa De Macedo[1,2,3], Jessica Escoffier[1,2,3], Paul Guichard[9], Charles Coutton[1,2,3,7], Selima Fourati Ben Mustapha[11], Mahmoud Kharouf[11], Anne-Pascale Bouin[1,2,3], Raoudha Zouari[11], Nicolas Thierry-Mieg[12], Serge Nef[8], Stefan Geimer[5], Corinne Loeuillet[1,2,3], Pierre Ray[1,2,3,4,‡], Christophe Arnoult[1,2,3,‡,*]

[1]Institute for Advanced Biosciences, (IAB), INSERM 1209,

[2] Institute for Advanced Biosciences, (IAB) CNRS UMR 5309

[3] Institute for Advanced Biosciences, (IAB) Université Grenoble Alpes

[4]UM GI-DPI, CHU Grenoble Alpes, F-38000 Grenoble, France

[5] Cell Biology/ Electron Microscopy, University of Bayreuth, 95440 Bayreuth, Germany

[6]Department of Genetics, Reproductive Biomedicine Research Center, Royan Institute for Reproductive Biomedicine, ACECR, Tehran-Iran. 16635-148

[7]UM de Génétique Chromosomique, Hôpital Couple-Enfant, CHU Grenoble Alpes, F-38000 Grenoble, France

[8]Department of Genetic Medicine and Development, University of Geneva Medical School, Geneva 1211, Switzerland

[9] University of Geneva, Department of Molecular and Cellular Biology, Sciences III, Geneva, Switzerland

[10]Present address: Human Technopole, 20157 Milan, Italy

[11]Polyclinique les Jasmins, Centre d'Aide Médicale à la Procréation, Centre Urbain Nord, 1003 Tunis, Tunisia

30 [12] Laboratoire TIMC/MAGe, CNRS UMR 5525, Pavillon Taillefer, Faculté de Medecine, 38700 La
31 Tronche, France

32

33 †These authors contributed equally to this work
34 ‡These authors contributed equally to this work as senior authors
35 *Correspondence: christophe.arnoult@univ-grenoble-alpes.fr or PRay@chu-grenoble.fr

36

37 Abstract

38 Genetic mutations are a recurrent cause of male infertility. Multiple morphological abnormalities of
39 the flagellum (MMAF) syndrome is a heterogeneous genetic disease, with which more than 50 genes
40 have been linked. Nevertheless, for 50% of patients with this condition, no genetic cause is identified.
41 From a study of a cohort of 167 MMAF patients, pathogenic bi-allelic mutations were identified in the
42 *CCDC146* gene in two patients. This gene encodes a poorly characterized centrosomal protein which
43 we studied in detail here. First, protein localization was studied in two cell lines. We confirmed the
44 centrosomal localization in somatic cells and showed that the protein also presents multiple
45 microtubule-related localizations during mitotic division, suggesting that it is a microtubule-associated
46 protein (MAP). To better understand the function of the protein at the sperm level, and the molecular
47 pathogenesis of infertility associated with *CCDC146* mutations, two genetically modified mouse
48 models were created: a *Ccdc146* knock-out (KO) and a knock-in (KI) expressing a HA-tagged CCDC146
49 protein. KO male mice were completely infertile, and sperm exhibited a phenotype identical to our
50 two MMAF patient's phenotype with *CCDC146* mutations. No other pathology was observed, and the
51 animals were viable. CCDC146 expression starts during late spermiogenesis, at the time of flagellum
52 biogenesis. In the spermatozoon, the protein is conserved but is not localized to centrioles, unlike in
53 somatic cells, rather it is present in the axoneme at the level of microtubule doublets. Expansion
54 microscopy associated with the use of the detergent sarkosyl to solubilize microtubule doublets,
55 suggest that the protein may be a microtubule inner protein (MIP). At the subcellular level, the absence
56 of CCDC146 affected the formation, localization and morphology of all microtubule-based organelles
57 such as the manchette, the head–tail coupling apparatus (HTCA), and the axoneme. Through this study,
58 we have characterized a new genetic cause of infertility, identified a new factor in the formation and/or
59 structure of the sperm axoneme, and demonstrated that the CCDC146 protein plays several cellular
60 roles, depending on the cell type and the stages in the cell cycle.

61 Introduction

62 Infertility is a major health concern, affecting approximately 50 million couples worldwide [1], or
63 12.5% of women and 10% of men. It is defined by the World Health Organization (WHO) as the "failure
64 to achieve a pregnancy after 12 months or more of regular unprotected sexual intercourse". In almost
65 all countries, infertile couples have access to assisted reproductive technology (ART) to try to conceive
66 a baby, and there are now 5 million people born as a result of ART. Despite this success, almost half of
67 the couples seeking medical support for infertility fails to successfully conceive and bear a child by the
68 end of their medical care. The main reason for these failures is that one member of the couple
69 produces gametes that are unable to support fertilization and/or embryonic development. Indeed,
70 ART does not specifically treat or even try to elucidate the underlying causes of a couple's infertility,
71 rather it tries to bypass the observed defects. Consequently, when defects in the gametes cannot be
72 circumvented by the techniques currently proposed, ART fails. To really treat infertility, a first step
73 would be to gain a better understanding of the problems with gametogenesis for each patient. This
74 type of approach should increase the likelihood of adopting the best strategy for affected patients, and
75 if necessary, should guide the development of innovative therapies.

76 Male infertility has several causes, such as infectious diseases, anatomical defects, or a genetic
77 disorder including chromosomal or single gene deficiencies. Genetic defects play a major role in male
78 infertility, with over 4000 genes thought to be involved in sperm production, of which more than 2000
79 are testis-enriched and almost exclusively involved in spermatogenesis [2]. Mutations in any of these
80 genes can negatively affect spermatogenesis and produce one of many described sperm disorders. The
81 characterization and identification of the molecular bases of male infertility is thus a real challenge.
82 Nevertheless, thanks to the emergence of massively parallel sequencing technologies, such as whole
83 exome sequencing (WES) and whole genome sequencing (WGS), the identification of genetic defects
84 has been greatly facilitated in recent years. As a consequence, remarkable progress has been made in
85 the characterization of numerous human genetic diseases, including male infertility.

86 Today, more than 120 genes are associated with all types of male infertility [3], including
87 quantitative and qualitative sperm defects. Qualitative spermatogenesis defects impacting sperm
88 morphology, also known as "teratozoospermia"[4, 5], are a heterogeneous group of abnormalities
89 covering a wide range of sperm phenotypes. Among these phenotypes, some relate to the morphology
90 of the flagellum. These defects are usually not uniform, and patients' sperm show a wide range of
91 flagellar morphologies such as short and/or coiled and/or irregularly sized flagella. Due to this
92 heterogeneity, this phenotype is now referred to as multiple morphological abnormalities of the sperm
93 flagellum (MMAF) [5]. Sperm from these patients are generally immotile, and patients are sterile.

94 Given the number of proteins present in the flagellum and necessary for its formation and

95 functioning, many genes have already been linked to the MMAF phenotype. Study of the MMAF
96 phenotype in humans has allowed the identification of around 50 genes [6] coding for proteins
97 involved in axonemal organization, present in the structures surrounding the axoneme – such as the
98 outer dense fibers and the fibrous sheath – and involved in intra-flagellar transport (IFT). Moreover,
99 some genes have been identified from mouse models, and their human orthologs are very good gene
100 candidates for MMAF, even if no patient has yet been identified with mutations in these genes. Finally,
101 based on the remarkable structural similarity of the axonemal structure of motile cilia and flagella,
102 some MMAF genes were initially identified in the context of primary ciliary dyskinesia (PCD). However,
103 this structural similarity does not necessarily imply a molecular similarity, and only around half (10 of
104 the 22 PCD-related genes identified so far [7]) are effectively associated with male infertility. However,
105 in most cases, the number of patients is very low and the details of the sperm tail phenotype are
106 unknown [7].

107 We have recruited 167 patients with MMAF. Following whole exome sequencing, biallelic
108 deleterious variants in 22 genes were identified in 83 subjects. The genes identified are *AK7*[8], *ARMC2*
109 [9], *CFAP206* [10], *CCDC34* [11], *CFAP251* [12], *CFAP43* and *CFAP44* [13], *CFAP47* [14], *CFAP61* [15],
110 *CFAP65* [16], *CFAP69* [17], *CFAP70* [18], *CFAP91* [19], *CFAP206* [10], *DNAH1* [20], *DNAH8* [21], *FSIP2*
111 [22], *IFT74* [23], *QRICH2* [24], *SPEF2* [25], *TTC21A* [26] and *TTC29* [27]. Despite this success, a molecular
112 diagnosis is obtained in half of the patients (49.7%) with this sperm phenotype, suggesting that novel
113 candidate genes remain to be identified. We have pursued our effort with this cohort to identify
114 further mutations that could explain the patient MMAF phenotype. As such, we have identified bi-
115 allelic truncating mutations in *CCDC146* in two unrelated infertile patients displaying MMAF. *CCDC146*
116 is known to code for a centrosomal protein when heterologously expressed in HeLa cells [28, 29], but
117 minimal information is available on its distribution within the cell, or its function when naturally
118 present. Moreover, this gene has never been associated with any human disease.

119 The centrosome, located adjacent to the nucleus, is a microtubule-based structure composed of a
120 pair of orthogonally-oriented centrioles surrounded by the pericentriolar material (PCM). The
121 centrosome is the major microtubule-organizing center (MTOC) in animal cells, and as such regulates
122 the microtubule organization within the cell. Therefore, it controls intracellular organization and
123 intracellular transport, and consequently regulates cell shape, cell polarity, and cell migration. The
124 centrosome is also crucial for cell division as it controls the assembly of the mitotic/meiotic spindle,
125 ensuring correct segregation of sister chromatids in each of the daughter cells [30]. The importance of
126 this organelle is highlighted by the fact that 3% (579 proteins) of all known human proteins have been
127 experimentally detected in the centrosome
128 (https://www.proteinatlas.org/humanproteome/subcellular/centrosome). Centrioles also play

129 essential roles in spermatogenesis and particularly during spermiogenesis. In round spermatids, the
130 centriole pair docks to the cell membrane, whereas the distal centriole serves as the basal body
131 initiating assembly of the axoneme. The proximal centriole then tightly attaches to the sperm nucleus
132 and gradually develops the head-to-tail coupling apparatus (HTCA), linking the sperm head to the
133 flagellum [31]. In human and bovine sperm, the proximal centriole is retained and the distal centriole
134 is remodeled to produce an 'atypical' centriole [32]; in contrast, in rodents, both centrioles are
135 degenerated during epididymal maturation [33]. Despite the number of proteins making up the
136 centrosome, and its importance in sperm differentiation and flagellum formation, very few
137 centrosomal proteins have been linked to MMAF in humans – so far only CEP135 [34], CEP148 [35] or
138 DZIP1 [36]. Moreover, some major axonemal proteins with an accessory location in the centrosome,
139 such as CFAP58 [37] and ODF2 [38, 39], have also been reported to be involved in MMAF syndrome.
140 Other centrosomal proteins lead to MMAF in mice, these include CEP131 [40] and CCDC42 [41]. The
141 discovery that MMAF in humans is linked to CCDC146, known so far as a centrosomal protein, adds to
142 our knowledge of proteins important for axoneme biogenesis.

143 In this manuscript, we first evaluated the localization of endogenous CCDC146 during the cell cycle
144 in two types of cell cultures, immortalized HEK-293T cells and primary human foreskin fibroblasts. To
145 validate the gene candidate and improve our knowledge of the corresponding protein, we also
146 generated two mouse models. The first one was a *Ccdc146* KO model, with which we studied the
147 impact of lack of the protein on the general phenotype, and in particular on male reproductive function
148 using several optical and electronic microscopy techniques. The second model was a HA-tagged
149 CCDC146 model, with which we studied the localization of the protein in different cell types. Data from
150 these genetically modified mouse models were confirmed in human sperm cells.

151

152

153 ## Results

154 ### 1/ WES identifies *CCDC146* as a gene involved in MMAF

155 We performed whole exome sequencing (WES) to investigate a highly-selected cohort of 167 MMAF
156 patients previously described in [9]. The WES data was analyzed using an open-source bioinformatics
157 pipeline developed in-house, as previously described [42]. From these data, we identified two patients
158 with homozygous truncating variants in the *CCDC146* (coiled-coil domain containing 146) gene,
159 NM_020879.3 (Figure 1A), which contains 19 exons in human. Sperm parameters of both patients are
160 presented in Figure 1—Figure supplement 1. No other candidate variants reported to be associated
161 with male infertility was detected in these patients. Despite an ubiquitous expression, this gene is
162 highly transcribed in human testes (Figure 1—Figure supplement 2A). The first identified mutation is
163 located in exon 9 and corresponds to c.1084C>T, the second is located in exon 15 and corresponds to
164 c.2112Del (Figure 1A). The c.1084C>T variant is a nonsense mutation, whereas the single-nucleotide
165 deletion c.2112Del is predicted to induce a translational frameshift. Both mutations were predicted to
166 produce premature stop codons: p.(Arg362Ter) and p.(Arg704serfsTer7), respectively, leading either
167 to the complete absence of the protein, or to the production of a truncated and non-functional protein.
168 These variants are annotated with a high impact on the protein structure (MoBiDiC prioritization
169 algorithm (MPA) score = 10) [43]. The two mutations are therefore most-likely deleterious. Both
170 variants were absent in our control cohort and their minor allele frequencies (MAF), according to the
171 gnomAD v3 database, were 6.984×10^{-5} and 6.5×10^{-06} respectively. The presence of these variants and
172 their homozygous state were verified by Sanger sequencing, as illustrated in Figure 1B. Taken together,
173 these elements strongly suggest that mutations in the *CCDC146* gene could be responsible for the
174 infertility of these two patients and the MMAF phenotype.

175 ### 2/ *Ccdc146* knock-out mouse model confirms that lack of CCDC146 is associated with MMAF

176 Despite a lower expression in mouse testes compared to human (the level of expression is only
177 medium, Figure 1—Figure supplement 2B), we produced by CRISPR/Cas9 two mouse lines carrying
178 each a frameshift mutation in *Ccdc146* (ENSMUST00000115245). One line (line 1) has a deletion of 4-
179 bp (Figure 2—Figure supplement 1AB) and the other (line 2) an insertion of 250-bp, both in exon 2. We
180 used these lines to address the hypothesis that CCDC146 deficiency leads to MMAF and male infertility.
181 We analyzed the reproductive phenotype of the gene-edited mice from the F2 generation and found
182 that homozygous males reproduced the MMAF phenotype, like the two patients carrying the
183 homozygous variants in the orthologous gene (Figure 2 for line 1 and Figure 2—Figure supplementary

184 1CD for line 2). Based on these findings, we restricted our study to a strain with a 4-bp deletion in exon
185 2 (c.164_167delTTCG).

186 The *Ccdc146* KO mice were viable without apparent defects. The reproductive phenotypes of male
187 and female mice were explored. WT or heterozygous animals and KO females were fertile, whereas
188 KO males were completely infertile (Figure 2A). This infertility is associated with a 90% decrease in
189 epididymal sperm concentration (from ~30- to ~3-million) (Figure 2B) and a significant decrease of
190 testicle weight relative to whole body weight (Figure 2C), suggesting a germ cell rarefaction in the
191 seminiferous epithelia due to high apoptosis level. A study of spermatogenic cell viability by TUNEL
192 assay confirmed this hypothesis, with a significant increase in the number of fluorescent cells in
193 *Ccdc146* KO animals (Figure 2—Figure supplement 2). Closer examination revealed sperm morphology
194 to be strongly altered, with a typical MMAF phenotype and marked defects in head morphology (Figure
195 2D) indicative of significantly impaired spermiogenesis. The percentage of abnormal form, flagellum
196 and head anomalies is 100% (Figure 2E). Moreover, an almost complete absence of motility was
197 observed (Figure 2F),

198 Comparative histological studies (Figure 3) showed that on sections of spermatogenic tubules,
199 structural and shape defects were present from the elongating spermatid stage in *Ccdc146* KO mice,
200 with almost complete disappearance of the flagella in the lumen and very long spermatid nuclei (Figure
201 3A). At the epididymal level, transverse sections of the epididymal tubules from KO males contained
202 almost no spermatozoa, and the tubules were filled with an acellular substance (Figure 3B).

203

204 **3/*CCDC146* codes for a centriolar protein**

205 CCDC146 has been described as a centriolar protein in immortalized HeLa cells [28, 29]. To confirm this
206 localization, we performed immunofluorescence experiments (IF) (Figure 4). First, we validated the
207 specificity of the anti-CCDC146 antibody (Ab) in HEK-293T cells by expressing DDK-tagged CCDC146.
208 We observed a nice colocalization of the DDK and CCDC146 signals in both interphase and mitotic cells,
209 showing that both Abs target the same protein (Figure 4—Figure supplement 1), strongly suggesting
210 that the anti-CCDC146 Ab is specific. Next, we focused on the centrosome (Figure 4A). In HEK-293T
211 cells, using an antibody recognizing centrin (anti-centrin Ab) as a centriole marker and the anti-
212 CCDC146 Ab, CCDC146 was shown to colocalize with centrioles. This colocalization strongly suggests
213 that CCDC146 is a centriolar protein. However, the signal was not strictly localized to centrioles, as
214 peri-centriolar labeling was clearly visible (Figure 4A1d, overlay). As this labeling pattern suggests the
215 presence of centriolar satellite proteins, we next performed co-labeling with an antibody recognizing

216 PCM1, a canonical centriolar satellite marker [44]. Once again, the colocalization was only partial
217 (Figure 4—Figure supplement 2). Finally, the presence of CCDC146 was assessed at the basal body of
218 primary cilia in cells cultured under serum-deprived conditions (Figure 4B). Similarly to centrosome
219 staining, CCDC146 was observed on the basal body by also around it (Figure 4B1d). Based on these
220 observations, CCDC146 has a unique localization profile in somatic cells that may indicate specific
221 functions.

222 **4/ CCDC146 co-localizes with multiple tubulin-based organelles.**

223 We next evaluated the presence of CCDC146 on centrioles during their duplication (Figure 5A). For this
224 purpose, we synchronized HEK-293T cells with thymidine and nocodazole, and CCDC146 labelling was
225 observed by IF. Both centrioles pairs were stained by CCDC146 Ab in cells blocked in the G2 phase
226 (Figure 5A). Because our immunofluorescence experiments revealed that CCDC146 labeling was not
227 strictly limited to centrosomes, we next assessed the presence of CCDC146 on other tubulin-containing
228 cellular substructures, particularly structures emerging during cell division (Figure 5B-E). In non-
229 synchronized cells, the mitotic spindle was labeled at its base and at its ends (Figure 5BC). The co-
230 labeling intensified in the midzone during chromatid separation (Figure 5D). Finally, the separation
231 structure between the two cells, the midbody, was also strongly stained (Figure 5E). As HEK-293T cells
232 are an immortalized cell line, we therefore verified that this labeling pattern was not due to an aberrant
233 expression profile and that it also reflected the situation in primary cell lines. Identical labeling profiles
234 were observed in freshly-prepared Human foreskin fibroblasts (HFF cells) (Figure 5—Figure
235 supplement 1).

236

237 **5/ CCDC146 is present in epididymal sperm and its expression peaks at spermatid elongation stage**
238 **during spermatogenesis.**

239 The presence of CCDC146 in the mature epididymal spermatozoa was assessed by WB (Figure 6A). To
240 overcome a lack of specific antibodies recognizing mouse CCDC146 (the commercial Ab works for
241 human CCDC146 only), a mouse strain expressing a HA-CCDC146 knock-in (KI) was created. Because
242 the functional domains of the protein are unknown, and to limit as such as possible the risk of
243 interfering with the structure of the protein, we choose to insert the hemagglutinin (HA) tag, which
244 contains only 9 amino acids (YPYDVPDYA). HA sequence was inserted by the CRISPR/Cas9 system into
245 the coding sequence of the *Ccdc146* gene between the two first codons to produce a tagged protein
246 at the N-terminus domain (Figure 6—Figure supplement 1). This insertion induced no phenotypic
247 changes, and both female and male mice were viable with normal fertility. Interestingly, the protein

248 was retained in epididymal sperm, where one band was observed around 120 kDa (Figure 6A). The
249 theoretical MW of the tagged protein is around 116.2 kDa (115.1 + 1.1); the observed MW was slightly
250 higher, suggesting that the protein migrates at a different weight or some post-translational
251 modifications. The band is specific because it was observed in HA-CCDC146 sperm only and not in WT
252 epdididymal sperm. The protein is therefore present during spermatid differentiation and conserved
253 in mature sperm. To better characterize the presence of CCDC146 in sperm, sperm flagella and heads
254 were purified after mild sonication (Figure 6B), and protein extracts were analyzed by WB (Figure 6A).
255 In the flagella fraction, the HA Ab revealed a band with an intensity similar to that of the whole sperm
256 at around 120 kDa whereas no staining was observed in head fraction.

257 From our immunofluorescence analysis of somatic cell lines, it was clear that CCDC146 expression is
258 associated with the cell cycle. In the testis, a wide variety of cell types co-exist, including both somatic
259 and germline cells. The germline cells can be further subcategorized into a wide variety of cells, some
260 engaged in proliferation (spermatogonia), others in meiosis (spermatocytes), or in differentiation
261 (spermatids). To better understand the role of CCDC146 in spermatogenesis, and thus how its absence
262 leads to sperm death and malformation, we initially studied its expression during the first wave of
263 spermatogenesis [45]. Results from this study should shed light on when CCDC146 is required for
264 sperm formation. Expression of *Ccdc146* was normalized with two different housekeeping genes, *Actb*
265 and *Hprt* (Figure 6C). Surprisingly, RT-PCR failed to detect *Ccdc146* transcripts on day 9 after birth in
266 proliferating spermatogonia from HA-CCDC146 males. Transcription of *Ccdc146* started on day 18,
267 concomitantly with the initiation of meiosis 2. Expression peaked on day 26, during the differentiation
268 of spermatids.

269 **6/ In sperm, CCDC146 is present in the flagellum, not in the centriole**

270 To attempt to elucidate the function of CCDC146 in sperm cells, we next studied its localization by IF
271 in mouse and human sperm. We focused successively on the anterior segment (head, neck and
272 beginning of the intermediate piece) of the sperm and then on the flagellum.

273 The IF experiments were first performed on murine epididymal spermatozoa. For this study, we used
274 the mouse model expressing HA-tagged CCDC146 protein. In conventional IF, using an HA Tag Alexa
275 Fluor® 488-conjugated Antibody (anti-HA-AF488-C Ab), a punctiform labeling was observed along the
276 whole flagellum (Figure 7A) on HA-CCDC146 only. We validated the specificity of the punctiform
277 staining by performing a statistical comparison of the density of dots in the principal piece of WT and
278 HA-CCDC146 sperm (Figure 7B). This study was carried out by analyzing 58 WT spermatozoa and 65
279 HA-CCDC146 spermatozoa coming from 3 WT and 3 KI males. We found a highly significant difference,
280 with a p-value <0.0001, showing that the signal obtained on spermatozoa expressing the tagged

281 protein is highly specific. To enhance resolution, ultrastructure expansion microscopy (U-ExM), an
282 efficient method to study in detail the ultrastructure of organelles [46], was used. We observed the
283 same punctiform staining all along the axoneme, including the midpiece (Figure 7C), using another
284 anti-HA Ab (#2). Unexpectedly, the mouse flagellum presented breaks that most likely resulted from
285 the expansion procedure (Figure 7D). Interestingly, strong HA-labeling was observed at the level of
286 these breaks suggesting that CCDC146 epitopes are buried inside the axonemal structure and become
287 accessible mostly on blunt or broken microtubule doublets. The same pattern was observed with a
288 third different anti-HA Ab (#3) (Figure 7—Figure supplement 1).

289 In humans, the spermatozoon retains its two centrioles [32], and they are observable in the neck, as
290 shown by anti-centrin and anti-tubulin labeling (Figure 8A1ac, A2ac and A3ac). No colocalization of the
291 CCDC146 label with centrin was observed on human sperm centrioles (Figure 8A1d, A2d and A3d),
292 suggesting that the protein is not present in or around this structure. However, two unexpected
293 labeling events were observed: sub-acrosomal labeling and labeling of the midpiece (Figure 8A1b, A2b
294 and A3b). At the flagellum level, faint staining was observed along the whole length (Figure 8A4b). To
295 enhance resolution, U-ExM was also used (Figure 8B). The localization of the two centrioles was
296 perfectly visible following anti-tubulin labeling, and was confirmed by co-labeling with an anti-POC5
297 Ab (Figure 8—Figure supplement 1A). Once again, no CCDC146 labeling was observed on sperm
298 centrioles (Figure 8B6 merge), confirming the conventional IF results. Moreover, U-ExM unveiled that
299 the observed CCDC146 midpiece staining (Figure 8A) seems in fact associated with isolated structures,
300 which we hypothesize could be mitochondria, now visible by expansion (Figure 8B1). This suggests that
301 the labeling on the midpiece observed in IF corresponds to non-specific mitochondrial labeling. This
302 conclusion is supported by the fact that the same isolated structures were also labeled with anti-POC5
303 Ab (Figure 8—Figure supplement 1B). In contrast, at the flagellum level, clear punctiform labeling was
304 observed along the whole length of the principal piece (Figure 8B1 and B5), confirming that the protein
305 is present in the sperm flagellum.

306 The study of CCDC146 localization was made in two species and with two different Abs. We observed
307 slight differences in the CCDC146 staining between human and mouse. However, the antibodies do
308 not target the same part of the CCDC146 protein (the tag is placed at the N-terminus of the protein,
309 and the HPA020082 Ab targets the last 130 amino acids of the Cter), a difference that may change their
310 accessibility to the antigenic site and explain the difference. Nevertheless, overall, the results are fairly
311 consistent and both antibodies target the flagellum. It should be noted that unlike in humans, in mice,
312 centrioles are no longer present in epididymal spermatozoa [33]. Therefore, the WB result, showing
313 the presence of the protein in sperm flagella fraction in mouse sperm, demonstrate unequivocally that
314 the protein is located in the flagellum.

315 **7/ CCDC146 labeling associates with microtubule doublets**

316 We next wanted to determine whether CCDC146 staining was associated with the axoneme or
317 accessory structures of the flagellum (outer dense fibers or fibrous sheath), and if yes, whether it was
318 associated with microtubule doublets or the central pair. To do so, we used U-ExM on human sperm
319 and quantified the relative position of each CCDC146 dot observed (outside the axoneme, outer left
320 and right; microtubule doublets left and right and central pair – Figure 9A-C). The different parts of the
321 flagellum were identified from the tubulin staining (Figure 9B). The distribution of localizations was
322 summarized in a bar graph, generated for two distinct sperm cells. Labeling was preferentially located
323 on the right and left doublets (Figure 9D), indicating that CCDC146 associates more with microtubule
324 doublets. Analysis of protein distribution in mice was not easy, because signal tended to concentrate
325 at breaks. Nevertheless, using U-ExM, on some spermatozoa with frayed microtubule doublets, i.e.
326 with the flagellum taking on the shape of a hair, we could find that isolated doublets carried the
327 punctiform labeling confirming the results of analyses on human spermatozoa (Figure 9E). Taken
328 together, these results from mouse and human sperm demonstrate that CCDC146 is an axonemal
329 protein, probably associated with microtubule doublets.

330 **8/ CCDC146 is solubilized by the sarkosyl detergent**

331 The presence of extensive labeling at axoneme breaks suggests that the antigenic site is difficult to
332 access in an intact flagellum. We therefore hypothesized that CCDC146 could be a MIP. MIPs are
333 generally resistant to solubilization by detergents. However, N-lauroylsarcosine (sarkosyl) can
334 solubilize microtubule doublets, with increasing concentrations destabilizing first the A-tubule, then
335 the B-tubule [47, 48]. Microtubule solubilization allows release of the MIPs contained within the
336 tubules, and the method is recognized [49, 50]. To test whether our hypothesis that CCDC146 may be
337 a MIP, we treated spermatozoa from HA-tagged CCDC146 mice with sarkosyl and performed a WB on
338 the supernatant (Figure 10A). The protein was effectively solubilized, leading to the appearance of
339 bands at around 120 kDa on an SDS-PAGE gel following migration of extracts from sperm treated with
340 0.2 and 0.4% sarkosyl concentrations. Interestingly, a second band around 90 kDa was also
341 immunodecorated by anti-HA antibody in the sarkosyl treated sample, a band not present in the
342 protein extracts from WT males. This band may correspond to proteolytic fragment of CCDC146, the
343 solubilization of microtubules by sarkosyl may have made CCDC146 more accessible to endogenous
344 proteases. The other detergents and buffers tested – RIPA, CHAPS or Tris-HCl – barely solubilized
345 CCDC146 or led to no solubilization (Figure 10B). This result confirms the unique action of sarkosyl on
346 CCDC146 and strengthens the hypothesis that the protein is associated with the doublets of
347 microtubules. To confirm the action of sarkosyl on the accessibility of the antigenic site, murine

348 spermatozoa were labeled with an anti-HA antibody after treatment with sarkosyl or no treatment.
349 CCDC146 labeling in the principal piece was significantly increased in the presence of sarkosyl (Figure
350 10C). The full image panel can be found in Figure 10—Figure supplement 1A. The presence of the
351 protein in the midpiece was difficult to assess because non-specific staining was observed in this area,
352 the non-specific staining being due to secondary antibodies as showed in Figure 10—Figure
353 supplement 1B, where they were used alone. Despite all these results, the CCDC146 localization in the
354 lumen of microtubules requires at this stage more proofs.

355 **9/ KO models show defects in tubulin-made organelles**

356 To better characterize the function of CCDC146 in mouse sperm, we went on to perform a detailed
357 morphological analysis of tubulin-made organelles by IF and scanning microscopy, and examined the
358 morphological defects induced by the absence of CCDC146 at the subcellular level by transmission
359 electron microscopy. This work was performed on immature testicular sperm and on seminiferous
360 tubule sections from adult WT and *Ccdc146* KO males. Mouse testicular sperm were used because they
361 still contain centrioles that become disassembled as sperm transit through the epididymis [51]. We
362 mainly focused our analyses on the centrioles, the manchette, and the axoneme.

363 The connecting piece between the head and the flagellum, known as the sperm head-tail coupling
364 apparatus (HTCA), is a complex structure containing several substructures including both centrioles,
365 the capitulum and the segmented columns [31]. The distal centriole is embedded in the segmented
366 column and the axoneme emerges from the distal centriole. This structure has a specific shape when
367 observed by scanning electron microscopy (Figure 11A). In *Ccdc146* KO sperm, there was a great
368 variability in the morphological defects of the connecting piece, some were almost intact (Figure
369 11A2), whereas others were severely damaged (Figure 11A3 and A4). In WT testicular sperm, IF
370 experiments show that the centrioles, identified by anti-tubulin Ab, are very close to each other and
371 adjacent to the nucleus (Figure 11B1). For *Ccdc146* KO males, although some sperm cells presented
372 centrioles with almost normal localization (Figure 11B2), centriole separation was visible in numerous
373 spermatozoa (Figure 11B3, B4), with the structures located far away from the connecting piece (Figure
374 11B5) or duplicated (Figure 11B6). These defects were not observed in WT sperm, demonstrating that
375 these defects were caused by the lack of CCDC146. Interestingly, the overall structure of the HTCA
376 under construction in spermatids, observed by TEM, was conserved in *Ccdc146* KO spermatids, with
377 the presence of both centrioles, containing nine triplets of microtubules, as well as accessory
378 cytoskeletal structures, including the capitulum and the segmented columns (Figure 12A1 for WT and
379 A2 for *Ccdc146* KO). The adjunct of the proximal centriole was also normal in *Ccdc146* KO spermatids
380 (Figure 12B) and no difference were observed with adjunct of WT spermatids (Figure 12—Figure

381 supplement 1). Remarkably, in a very large proportion of sections, no singlet or doublet of
382 microtubules emerged from the distal KO centriole, suggesting that the process of tubulin
383 polymerization is somehow hampered in these cells (Figure 12A2). The absence of microtubules at the
384 end of the distal centriole was confirmed by analysis of serial sections of the sperm centrioles (Figure
385 12C). Moreover, the defects observed in IF experiments, such as duplication, or defective attachment
386 to the nuclear membrane, were frequently confirmed in TEM images (Figure 12—Figure supplement
387 2). Such defects were not observed in WT spermatids.

388 Manchette formation – which occurs from the round spermatid to fully-elongated spermatid stages –
389 was next studied by IF using β-tubulin Ab. Simultaneously, we monitored formation of the acrosome
390 using an antibody binding to DPY19L2 (Figure 13). Initial acrosome binding at step 3 spermatid was not
391 disrupted (not shown), and we observed no differences in covering of the anterior portion of spermatid
392 nucleus at steps 7-8 spermatids (Figure 13A1/A2). The development of the manchette in between
393 steps 9-12 spermatids was not hampered, but noticeable defects appeared indicating defective
394 manchette organization– such as a random orientation of the spermatids (Figure 13B1/B2) and
395 abnormal acrosome shapes (Figure 13C1/C2). Finally, at steps 13-15 spermatids, the manchette was
396 clearly longer and wider than in WT cells (Figure 13D1/D2 and Figure 13—Figure supplement 1A),
397 suggesting that the control of the manchette dynamic is defective: in KO spermatids, the reduction
398 and disappearance of the manchette is hampered and contrary to WT continue to expand (Figure 13—
399 Figure supplement 1B). In the mean time, the acrosome is strongly remodeled, as shown in Figure 16H,
400 and is detached from the nucleus. This latter morphological defect is associated with a loss of the
401 DPY19L2 staining (Figure 13D2). In TEM, microtubules of the manchette were clearly visible
402 surrounding the compacting nucleus of elongating spermatids in both WT and KO. The manchette
403 normally anchors on the perinuclear ring, which is itself localized just below the marginal edge of the
404 acrosome and separated by the groove belt (Figure 14 A-B blue arrows) [52]. In KO spermatids, many
405 defects such as marked asymmetry and enlargement were visible (Figure 14C-F). The perinuclear ring
406 was no longer localized in the vicinity of the acrosome (Figure 14 C-F red arrows) and was often spread
407 into the cytoplasm, providing a large nucleation structure for the manchette (Figure 14 D-F, black
408 double arrows), which explains its width and irregularity.

409 Numerous defects were also observed in the axoneme. These axoneme defects were generally similar
410 to the defects observed in other MMAF mouse models, with disorganization of the axoneme structure
411 (Figure 15A) accompanied by fragmentation of the dense fibers and their random arrangement in cell
412 masses anchored to the sperm head (Figure 15B). The absence of emerging singlet or doublet
413 microtubules at the base of the distal centriole leads to a complete disorganization of the flagellum
414 and the presence of notably dense fiber rings devoid of internal tubulin elements (Figure 15BC, red

415 squares and enlargements). Typical cross sections of the midpiece and principal piece of WT sperm are
416 shown in Figure 15—Figure supplement 1

417 Finally, the shape of the nucleus presented numerous abnormalities during elongation (Figure 16). The
418 emergence of head defects was concomitant to the implantation of the manchette (Figure 16E, red
419 arrow), with no defects observed on round spermatids at stages III-VIII. Unexpectedly, a distortion was
420 created in the center of the nucleus at the anterior pole, causing the formation of a bilobed compacted
421 nucleus (Figure 16E-F, red arrows) and likeky responsible of the presence of visible vacuoles inside the
422 nuclei (Figure 16G-H, white arrows). Moreover, acrosomes were severely impacted at steps13-15
423 spermatid, with strong deformations and detachment (Figure 16H, blue arrow heads).

424

425 Discussion

426 This study allowed us to identify and validate the involvement of a new candidate gene in male
427 infertility, *CCDC146*. This gene was first described in mice by our team earlier this year, in the context
428 of a research project on the different types of genetic causes of sperm abnormalities in mouse [53].
429 However, no data other than the sperm phenotype (MMAF) was presented in this initial report. In this
430 paper, we present for the first time, the evidence of the presence of mutations in humans and a
431 description of the localization of the protein in somatic and germ cells. We also examined the lesion
432 spectrum at the subcellular level, to obtain a detailed view of the molecular pathogenesis associated
433 with defects in this gene.

434 1/ Genetic complexity of MMAF

435 The question of how to interpret and annotate the mutations identified by high-throughput
436 sequencing is an important issue in clinical genetics. The most difficult step is certainly the
437 identification of genes associated with a given disease. Beyond pure genetic data and the pathogenicity
438 of mutations, a fundamental element is the reproduction of the disease when the gene is absent in an
439 animal model. When these two elements are combined – KO photocopying disease and pathogenicity
440 of the identified mutations - the probability of mutation causality in the studied disease is very high.
441 Both mutations are predicted to produce a premature stop codons: p.Arg362Ter and
442 p.Arg704serfsTer7, leading either to the complete absence of the protein in case of non-sense
443 mediated mRNA decay or to the production of a truncated protein missing almost two third or one
444 fourth of the protein respectively. *CCDC146* is very well conserved throughout evolution (Figure
445 supplementary 1), including the 3' end of the protein which contains a large coil-coil domain (Figure

446 1). In view of the very high degree of conservation, it is most likely that the 3' end of the protein, absent
447 in both subjects, is critical for the CCDC146 function and hence that both mutations are deleterious.
448 These results combined with the fact that the absence of CCDC146 is deleterious in mice and induces
449 an infertility similar to that observed in the human, enable us to associate *CCDC146* with MMAF
450 syndrome in humans .

451 It is essential to characterize all genes involved in male infertility. Therefore, the characterization of a
452 new gene involved in MMAF syndrome is not just "one more gene". First, it further confirms that
453 MMAF syndrome is a heterogeneous recessive genetic disease, currently associated with defects in
454 more than 50 genes. Second, it helps direct the diagnostic strategy to be directed during genome-wide
455 searches. The type of profiling required for MMAF is very different from that performed for instance
456 for cystic fibrosis, where one mutation is responsible for more than 50% of cases. Third, the discovery
457 of all genes involved in MMAF is important in the context of oligogenic heterozygous inheritance of
458 sperm abnormalities in human [53]. Indeed, a homozygous deleterious mutation is found in only half
459 of all MMAF patients, suggesting that other modes of inheritance must be involved. Only by
460 establishing an extended list of genes linked to MMAF will it be possible to determine whether
461 oligogenic heterozygous inheritance is a relevant cause of this syndrome in humans. Finally, some of
462 the genes involved in MMAF syndrome are also involved in ciliary diseases [7]. By further exploring
463 MMAF-type infertility, we can hope to enhance our understanding of another underlying pathology.
464 Although the vast majority of patients with PCD are diagnosed before 5 years of age [54], one study
465 showed that in a cohort of 240 adults with a mean age of 36 years (36 ± 13) presenting with chronic
466 productive cough and recurrent chest infections, PCD was identified for the first time in 10% of patients
467 [55]. This result suggests that infertility diagnosis can occur before PCD diagnosis, and consequently
468 that infertility management might improve PCD diagnosis and care.

469 **2/ CCDC146 is present in flagellum and absent of in sperm centriole**

470 Several proteomics studies of the sperm centriole identified CCDC146 as a centrosome-associated
471 protein in bovine sperm [28, 56], a species where centrioles are present in ejaculated sperm. Using a
472 different methodological approach, based on IF with conventional and expansion microscopy, we
473 observed no CCDC146 signal in centrioles from testicular mouse and ejaculated human sperm. The
474 same result was obtained with two different types of antibodies: with human sperm, we used a
475 commercial anti-CCDC146 Ab, whereas with mouse sperm we used several anti-HA antibodies. The
476 same IF approach allowed us to clearly identify the sperm centrosome using a number of antibodies
477 such as anti-POC5 and anti-beta tubulin, ruling out a possible failure of our IF protocol. It is worth
478 noting that centrosomal proteins were isolated from whole flagella using several strategies including

479 sequential use of multiple detergents, and that the centrosomal proteins were purified in the last
480 fractions. These results indicate that CCDC146 is in fact barely soluble in conventional buffers, which
481 could explain why it is co-purified with the centrosomal fraction in proteomics studies.

482 In epididymal mouse sperm, the biochemical analyses showed the presence of the protein in the
483 flagellum only, and not in the head fractions: the detection of the band appeared very quickly at
484 visualization and became very strong after few minutes, demonstrating that the protein is abundant
485 in the flagella. It is important to note that epididymal sperm do not have centrioles and therefore this
486 signal is not a centriolar signal. We also performed a statistical analysis showing that the immuno-
487 staining observed in the principal piece of mouse sperm is very specific (Figure 7B). Altogether, these
488 results demonstrate unequivocally the intracellular localization of CCDC146 in the flagellum of mouse
489 sperm. In human, we obtained very similar results, with a flagellar localization. Using expansion
490 microscopy, we show that the protein is associated with the microtubule doublets in both mouse
491 sperm (Figure 9E) and human sperm (Figure 9 B-D).

492 Moreover, CCDC146 was solubilized with the sarkosyl detergent only, known to destabilize
493 microtubules and generally used to identify microtubule inner proteins (MIP) and the CCDC146
494 fluorescent signal was enhanced when sperm were treated with this peculiar detergent. Expansion
495 microscopy also revealed a strong signal in mouse sperm at the point of axoneme rupture. Taken
496 together, these elements strongly suggest that CCDC146 is a microtubule associate protein (MAP) and
497 may be a MIP. However more experiments need to be performed to validate the inner localization of
498 CCDC146 because there are other proteins, located in the peri-axonemal structure of the axoneme,
499 that are difficult to solubilize as well.

500 Finally, in human sperm, staining was observed on acrosome and in the midpiece. Staining on
501 acrosome should always be taken with caution in sperm. Indeed, numerous glycosylated proteins are
502 present at the surface of the plasma membrane regarding the outer acrosomal membrane for sperm
503 attachment, and are responsible to numerous non-specific staining. Moreover this acrosomal staining
504 was not observed in mouse sperm, strongly suggesting that it is not specific.

505 Concerning the staining in the midpiece observed in both conventional and Expansion microscopy, it
506 also seems to be nonspecific and associated with secondary Abs. In Figure 8—Figure supplement 1B
507 showing the localization of POC5, a very similar staining of the midpiece was also observed, although
508 POC5 was never described to be present in the midpiece, therefore questioning the specificity of the
509 signal observed with the anti-CCDC146 antibody in the midpiece. POC5 and CCDC146 staining
510 experiments shared the same secondary Ab and the midpiece signal was likely due to it. For midpiece
511 staining observed in Figure 10C and Figure 10—Figure supplement 1A by IF, it is worth to note that a

512 similar staining was observed when secondary Ab were used alone (see Figure 10—Figure supplement
513 1B). The strong fluorescent signal is clearly due to secondary Abs, likely masking the punctuate staining
514 of the axoneme.

515 **3/ Functional complexity of CCDC146**

516 The results presented in this report show striking differences in localization of CCDC146 between
517 somatic and germ cells. Our results show that the protein displays several subcellular localizations,
518 which vary according to the cell cycle, and the cell nature. In somatic cells, the protein is mostly
519 associated with the centrosome and other microtubular structures – in particular the mitotic spindle –
520 at the end of microtubules and at the level of the kinetochore and the midbody. These observations
521 also identify CCDC146 as a MAP. In contrast, in spermatozoa, our results indicate that CCDC146 is an
522 axonemal protein that seems to be associated with the microtubule doublets. Despite its broad cellular
523 distribution, the association of CCDC146 with tubulin-dependent structures is remarkable. However,
524 centrosomal and axonemal localizations in somatic and germ cells, respectively, have also been
525 reported for CFAP58 [37, 57], thus the re-use of centrosomal proteins in the sperm flagellar axoneme
526 is not unheard of. In addition, 80% of all proteins identified as centrosomal are found in multiple
527 localizations (https://www.proteinatlas.org/humanproteome/subcellular/centrosome). The ability of
528 a protein to home to several locations depending on its cellular environment has been widely
529 described, in particular for MAP. The different localizations are linked to the presence of distinct
530 binding sites on the protein. For example, MAP6 binds and stabilizes microtubules, through Mc
531 modules, and associates with membranes and neuroreceptors through palmitoylated cysteines. MAP6
532 can also localize in the microtubule lumen, in its role as MIP, thanks to its Mn modules. Finally, in
533 addition to its associations with subcellular compartments and receptors, the presence of proline-rich
534 domains (PRD) in the MAP6 sequence, allows it to bind to SH3-domain-containing proteins, and thus
535 triggering activation of signaling pathways [58]. Another example of a protein with multiple
536 localizations is CFAP21, which is a MIP but also a cytosolic calcium sensor. In the latter capacity, CFAP21
537 modulates the interaction of STIM1 and ORAI1 upon depletion of calcium stores [59, 60]. These
538 examples illustrate the complexity of function of some multiple-domain proteins.

539 The fact that CCDC146 can localize to multiple subcellular compartments suggests that it also contains
540 several domains. Interestingly, a PF05557 motif (Pfam mitotic checkpoint protein,
541 https://www.ebi.ac.uk/interpro/protein/UniProt/E9Q9F7/) has been identified in the mouse CCDC146
542 sequence between amino acids 130 and 162. Proteins belonging to the "mitotic spindle checkpoint"
543 monitor correct attachment of the bipolar spindle to the kinetochores. The presence of this motif likely
544 explains the ability of CCDC146 to localize to cell cycle-dependent subcellular compartments

545 containing tubulin. However, the most important structural motifs identified in CCDC146 are the
546 coiled-coil domains. Although coiled-coil domains play a structural role in a variety of protein
547 interactions, their presence in CCDC146 remains mysterious, and how they contribute to its function
548 remains to be elucidated. Nevertheless, this motif is compatible with a MIP function for this protein,
549 since several MIP proteins including CCDC11 (FAP53), CCDC19 (FAP45), and CCDC173 (FAP210) are
550 coiled-coil proteins [59]. It is worth noting that the ortholog of *CCDC146* in *Chlamydomonas*, *MBO2*,
551 codes for a protein required for the beak-like projections of doublets 5 and 6, located inside the lumen
552 of the tubule B [61], in the proximal part of the *Chlamydomonas* flagellum. Although no beak-like
553 projections are present in the mammalian axoneme, the location inside the tubule seems to be
554 evolutionarily conserved. A more recent study of MBO2 showed that the protein is also present all
555 along the flagellum of *Chlamydomonas* and is tightly associated with microtubule doublets [62]. These
556 observations support our results showing association of CCDC146 with this axonemal structure.

557 The results presented here also show a striking difference in the phenotype induced by the lack of the
558 protein in somatic and male germ cells. This protein is essential for spermatogenesis, and its absence
559 leads to immotile non-functional sperm and to complete infertility in both humans and mice.
560 Conversely, both patients and *Ccdc146* KO mice seem to be healthy and present no other conditions
561 such as primary ciliary dyskinesia (PCD). CCDC146, despite its wide expression profile in many tissues
562 therefore seems to be dispensable except during spermatogenesis. Nevertheless, because this protein
563 is localized on the tips of the spindle and may be involved in mitotic checkpoints, its absence may lead
564 to late proliferative disorders. This hypothesis is supported by the fact that *CCDC146* is reported to be
565 down-regulated in thyroid cancer [63]. The link between infertility and risk of cancer was recently
566 underlined, with mutations found in genes like *FANCM* [64]. Therefore, it would be interesting to
567 monitor aging in *Ccdc146* KO mice and to study their life expectancy and cancer rates compared to WT
568 mice.

569

570 **4/ TEM reveals that lack of CCDC146 severely impacts microtubule-based organelles**

571 No morphological defects were observed before the elongating spermatid stage, and in round
572 spermatids, the acrosome started to spread on the nucleus in a normal way (Figure 13). Morphological
573 defects appeared clearly from the onset of spermatid elongation. This result indicates that the protein
574 is only necessary for late spermiogenesis, from the phase corresponding to flagellum biogenesis. All
575 the organelles composed mainly of tubulin were strongly affected by the absence of the protein.

576 The manchette structure in elongating *Ccdc146* KO spermatids was asymmetric, abnormally broad,
577 and ectopic, leading to the formation of aberrantly-shaped sperm heads. So far, manchette defects
578 have been associated with defects in intra-flagellar transport (IFT), and intra-manchette transport
579 (IMT) [65]. CCDC146 was only localized to the sperm axoneme by IF, and no signal was observed in the
580 manchette, suggesting that CCDC146 is probably not involved in the transport machinery. Moreover,
581 our results indicated that the manchette was remarkably long in elongated spermatids. A similar
582 phenotype was observed in Katanin80-deficient animals [66]. Katanin80 is a microtubule-severing
583 enzyme that is important for manchette reduction. Interestingly, the absence of WDR62, a scaffold
584 protein involved in centriole duplication, leads to defective katanin80 expression, and the presence of
585 elongated manchettes in mice [67]. In combination with our results, this detail suggests that the
586 manchette's structure and its reduction are influenced by centrosomal proteins, possibly through
587 katanin80 defects. The precise molecular link between CCDC146 and manchette assembly and
588 reduction remains to be identified.

589 The HTCA was also aberrant in *Ccdc146* KO spermatids. Centrioles in elongating spermatids were
590 frequently displaced from their implantation fossa at the nuclear envelope. We observed some
591 correctly lodged centrioles in round spermatids; however, we are unable to determine with certainty
592 whether the majority of centrioles failed to correctly attach or whether they detached from the nuclear
593 envelope during spermatid elongation. Defects in cohesion of the HTCA have been associated with the
594 acephalic spermatozoa syndrome, and were shown to involve a number of proteins such as SUN5,
595 SPATA6 and ODF1 [4, 68-70]. Here, we did not observe any sperm decapitation, suggesting that
596 CCDC146 is involved in a different pathway controlling the HTCA. Moreover, elongating *Ccdc146* KO
597 spermatids displayed supernumerary centrioles. Abnormal centriole numbers have also been reported
598 in the absence of a few other centrosome-associated proteins including DZIP1 [36] and CCDC42 [41],
599 and of microtubule-regulating proteins such as katanin like-2 [71] and tubulin deglutamylase CCP5
600 [72].

601 Overall, these results suggest a relationship between the manchette and the centrioles. In the
602 literature there are limited information about this relationship. Studies of the spermiogenesis defects
603 observed in different models deficient for centrosomal proteins show some common features such as
604 abnormal manchette and duplicated centrosomes. The absence of these proteins does not appear to
605 be directly responsible for these defects, rather it seems to modify the expression of microtubule
606 regulatory proteins such as katanins [66, 67, 71]. Moreover, there is a report showing that both
607 organelles share molecular components [73].These modifications could explain the pleiotropic effect
608 of the absence of CCDC146 on microtubule-based organelles.

609 In conclusion, by characterizing the genetic causes of human infertility, we not only improve
610 the diagnosis and prognosis of these pathologies but also pave the way for the discovery of new players
611 in spermatogenesis. We are constantly adding to the number of proteins present in the flagella of the
612 mammalian spermatozoa that are necessary for its construction and functioning. This study showed
613 that CCDC146, a protein previously described as a centrosomal protein in somatic and germ cells,
614 localizes in spermatozoa's axonemal microtubule doublets. The presence of CCDC146 in somatic cells'
615 centrosomes gives weight to the idea of a centrosome with a dynamic composition, allowing it to fulfill
616 its multitude of functions throughout all the phases of cellular life.

617

618 ## Material and methods

619 Human subjects and controls

620 We analyzed WES data from a cohort of 167 MMAF individuals previously established by our team [9].
621 All individuals presented with a typical MMAF phenotype characterized by severe asthenozoospermia
622 (total sperm motility below 10%) with at least three of the following flagellar abnormalities present in
623 >5% of the spermatozoa: short, absent, coiled, bent or irregular flagella. All individuals had a normal
624 somatic karyotype (46,XY) with normal bilateral testicular size, normal hormone levels and secondary
625 sexual characteristics. Sperm analyses were carried out in the source laboratories during routine
626 biological examination of the individuals according to World Health Organization (WHO) guidelines
627 [74]. Informed and written consents were obtained from all the individuals participating in the study
628 and institutional approval was given by the local medical ethical committee (CHU Grenoble Alpes
629 institutional review board). Samples were stored in the Fertithèque collection declared to the French
630 Ministry of health (DC-2015-2580) and the French Data Protection Authority (DR-2016-392).

631 Sanger sequencing

632 *CCDC146* single nucleotide variants identified by exome sequencing were validated by Sanger
633 sequencing as previously described [9]. PCR primers used for each individual are listed in Table
634 supplementary 1.

635

636 Cell culture

637 HEK-293T (Human Embryonic Kidney) and HFF (Human Foreskin Fibroblasts) cells were grown in D10
638 medium consisting in DMEM with GlutaMAX (Dulbecco's Modified Eagle's Medium, Sigma Aldrich)
639 supplemented with 10% heat-inactivated fetal bovine serum (FBS, Life Technologies) and 10% of
640 penicillin-streptomycin (Sigma Aldrich) in a 5% CO_2 humidified atmosphere at 37 °C. HEK-293T cells
641 were divided twice weekly by 1/10 dilution. HFFs cells were divided 1/5 one time a week.

642 Ethics statement

643 Breeding and experimental procedures were carried out in accordance with national and international
644 laws relating to laboratory animal welfare and experimentation (EEC Council Directive 2010/63/EU,
645 September 2010). Experiments were performed under the supervision of C.L. (agreement 38 10 38) in
646 the Plateforme de Haute Technologie Animale (PHTA) animal care facility (agreement
647 C3851610006 delivered by the Direction Départementale de la Protection des Populations) and were

648 approved by the ethics committee of the PHTA and by the French government (APAFlS#7128-
649 2016100609382341.v2).

650 Generation of *Ccdc146* KO and HA-tagged CCDC146 mice

651 *Ccdc146* KO mice were generated using the CRISPR/Cas9 technology as previously described [53].
652 Briefly, to maximize the chances of generating deleterious mutations, two gRNAs located in two
653 distinct coding exons located at the beginning of the targeted gene were used. For each gene, the two
654 gRNAs (5'-CCT ACA GTT AAC ATT CGG G-3' and 5'-GGG AGT ACA ATA TTC AGT AC-3'), respectively
655 targeting exons 2 and 4, were inserted into two distinct plasmids, each plasmid also contained the Cas9
656 sequence. The Cas9 gene was controlled by a CMV promoter and the gRNA and its RNA scaffold by a
657 U6 promoter. Full plasmids (pSpCas9 BB-2A-GFP (PX458)) containing the specific sgRNA were ordered
658 from Genescript (https://www.genscript.com/crispr-synthetic-sgrna.html). Both plasmids were co-
659 injected into the zygotes' pronuclei at a concentration of 2.5 ng/mL. Plasmids were directly injected as
660 delivered by the supplier, without in vitro production and purification of Cas9 proteins and sgRNA.

661 *HA-Ccdc146* knock-in mice were also generated by CRISPR/Cas9. Twenty-seven nucleotides encoding
662 the HA (hemagglutinin) tag (5'-TAC CCA TAC GAT GTT CCA GAT TAC GCT TAG-3') were inserted
663 immediately after the start codon of *Ccdc146*. One plasmid containing one sgRNA (5'-TAC TTT AGA ACT
664 GTG AAA AA-3') and Cas9 was injected (5 ng/µL) with a single-stranded DNA (150 nucleotides, 50 ng/µl)
665 as a template for the homology directed repair (HDR) Figure 6—Figure supplement 1. PCR primers used
666 for genotyping are listed in Table supplementary 1. Genetically modified *Ccdc146* strains were bred in
667 the Grenoble university animal platform (HTAG) and housed under specific-pathogen-free conditions.
668 Animals were euthanized by cervical dislocation at the indicated ages.

669

670 Phenotypic analysis of *Ccdc146* KO mice

671 Fertility test – Three adult males of each genotype were housed individually with two fertile
672 WT B6D2 females for 12 weeks. The date of birth and the number of pups were recorded.

673 Sperm analysis – Epididymal sperm were obtained by making small incisions in the mouse
674 caudae epididymides placed in 1 mL of warm M2 medium (Sigma Aldrich), and the sperm were allowed
675 to swim up for 10 min at 37 °C. Sperm samples (10 µL) were used for Computer-assisted semen analysis
676 (CASA, Hamilton Thorn Research, Beverley, MA, USA) using a 100-µm-deep analysis chamber (Leja
677 Products B.V., Nieuw-Vennep, the Netherlands). A minimum of 100 motile sperm was recorded in each
678 assay. The remaining sperm samples were washed in 1X phosphate buffered saline (PBS, Life
679 technologies), 10 µL were spread onto slides pre-coated with 0.1% poly-L-lysine (Epredia), fixed in 70%
680 ethanol (Sigma Aldrich) for 1 h at room temperature (RT) and submitted to a papanicolaou staining

681 (WHO laboratory manual) to assess sperm morphology. Images were obtained using a Zeiss AxioImager
682 M2 fitted with a 40X objective (color camera AxioCam MRc) and analyzed using ZEN (Carl Zeiss, version
683 3.4).

684

685 Testis and epididymides histology

686 Testis and epididymides samples from 8-16-week-old mice were fixed for 24 h in PBS/4% PFA
687 (Electron Microscopy Sciences), dehydrated in a graded ethanol series, embedded in paraffin wax,
688 sectioned at 5 µm and placed onto Superfrost slides (Fischer scientific). For both, slides were
689 deparaffinated and rehydrated prior to use. Tissue morphology and structure were observed after
690 coloration by Mayer's hematoxylin and eosin phloxine B (WHO protocols) using a Zeiss AxioImager M2
691 (color camera AxioCam MRc).

692 Terminal deoxynucleotidyl transferase dUTP nick-end labeling (TUNEL) assay on testes

693 Testes samples from three adult individuals for each genotype were analyzed. Apoptotic cells
694 in testis sections were identified using the Click-iT™ Plus TUNEL Assay kit (Invitrogen) in line with the
695 manufacturer's instructions. DNA strand breaks for the positive control were induced by DNase I
696 treatment. Each slide contained up to eight testis sections. DNA was stained with Hoechst (2 µg/mL).
697 Images were acquired and reconstituted using a Zeiss Axioscan Z1 slide scanner and analyzed by Fiji
698 [75]. The total number of seminiferous tubules and the number of tubules containing at least one
699 TUNEL-positive cell were counted in each testis section.

700 Conventional Immunofluorescence (IF)

701 Somatic Cells – HEK-293T or HFFs (10 000 cells) were grown on 10-mm coverslips previously
702 coated with poly-D-lysine (0.1 mg/mL, 1 h, 37 °C, Gibco) placed in a well on a 24-well plate. For cell
703 synchronization experiments, cells underwent S-phase blockade with thymidine (5 mM, Sigma-Aldrich)
704 for 17 h followed by incubation in a control culture medium for 5 h, then a second blockade at the G2-
705 M transition with nocodazole (200 nM, Sigma-Aldrich) for 12 h. Cells were then fixed with cold
706 methanol (Sigma Aldrich) for 10 min at different times for IF labelling. After washing twice in PBS, non-
707 specific sites were blocked with PBS/5% FBS/5% NGS (normal goat serum, Life technologies) for 1 h at
708 RT. After washing three times in PBS/1% FBS, primary antibody was added in PBS/1% FBS and
709 incubated overnight at 4°C. Coverslips were washed three times in PBS/1% FBS before adding
710 secondary antibody in PBS/1% FBS and incubating for 2 h at RT. After washing three times in PBS, nuclei
711 were stained with 2 µg/mL Hoechst 33342 in PBS (Sigma Aldrich). Coverslips were once again washed

712 three times in PBS, then carefully placed on Superfrost slides (cells facing the slide) and sealed with
713 nail polish.

714 Spermatogenic cells – Seminiferous tubules were isolated from mouse testes (8–16 weeks old).
715 After removing of the tunica albuginea, the testes were incubated at 37 °C for 1 h in 3 mL of a solution
716 containing (mM): NaCl (150), KCl (5), CaCl2 (2), MgCl2 (1), NaH2PO4 (1), $NaHCO_3$ (12), D-glucose (11),
717 Na-lactate (6), HEPES (10) pH 7.4, and collagenase type IA (1 mg/mL – Sigma Aldrich). Tubules were
718 rinsed twice in collagenase-free medium and cut into 2-mm sections. Spermatogenic cells were
719 obtained by manual trituration and filtered through a 100-µm filter. The isolated cells were centrifuged
720 (10 min, 500 g), resuspended in 500 µL PBS and 50 µL was spread onto slides pre-coated with 0.1%
721 poly-L-lysine (Epredia) and allowed to dry. Dried samples were fixed for 5 min in PBS/4% PFA. After
722 washing twice in PBS, slides were placed in PBS/0.1% Triton/5% BSA (Euromedex) for 90 min at RT.
723 Following two washes in PBS, the primary antibody was added in PBS/1% BSA overnight at 4 °C. After
724 washing three times in PBS/1% BSA, secondary antibody was added in PBS/1% BSA for 2 h at RT. After
725 washing three times in PBS, nuclei were stained with 2 µg/mL Hoechst 33342 in PBS (Sigma Aldrich)
726 and slides were mounted with DAKO mounting media (Agilent).

727 Testis sections – After deparaffination and rehydration, testis sections were subjected to heat
728 antigen retrieval for 20 min at 95 °C in a citrate-based solution at pH 6.0 (VectorLabs). Tissues were
729 then permeabilized in PBS/0.1% Triton X-100 for 20 min at RT. After washing three times in PBS (5 min
730 each), slides were incubated with blocking solution (PBS/10% BSA) for 30 min at RT. Following three
731 washes in PBS, slides were incubated with primary antibodies in PBS/0.1% Tween/5% BSA overnight
732 at 4 °C. Slides were washed three times in PBS before applying secondary antibodies in blocking
733 solution and incubating for 2 h at RT. After washing in PBS, nuclei were stained with 2 µg/mL Hoechst
734 33342 in PBS (Sigma Aldrich) for 5 min at RT. Slides were washed once again in PBS before mounting
735 with DAKO mounting media (Agilent).

736 Spermatozoa - Mouse spermatozoa were recovered from the caudae epididymides. After their
737 incision, sperm were allowed to swim in 1 mL of PBS for 10 min at 37 °C. They were washed twice with
738 1 mL of PBS 1X at 500 g for 5 min, and 10 µL of each sample was smeared onto slides pre-coated with
739 0.1% poly-L-lysine (Epredia). Sperm were fixed in PBS/4% PFA for 45 s, washed twice in PBS and
740 permeabilized in PBS/0.1% Triton for 15 min at RT. After incubation in PBS/0.1% Triton/2% NGS for 2 h
741 at RT, primary antibody was added in PBS/0.1% Triton/2% NGS overnight at 4 °C. After washing three
742 times in PBS/0.1% Triton, the secondary antibody was applied in PBS/0.1% Triton/2% NGS for 90 min
743 at RT. Slides were washed three times in PBS before staining nuclei with 2 µg/mL Hoechst 33342 in PBS

744 (Sigma Aldrich). Slides were washed once in PBS before mounting with DAKO mounting media
745 (Agilent).

746 For human spermatozoa, the protocol was based on that of Fishman *et al.* [32]. Straws were
747 thawed at RT for 10 min and resuspended in PBS. Sperm were washed twice in 1 mL of PBS (10 min,
748 400 g), 50 µL was spread onto slides pre-coated with 0.1% poly-L-lysine and left to dry. Dry slides were
749 fixed in 100% ice-cold methanol for 2 min and washed twice in PBS. Cells were permeabilized in PBS/3%
750 Triton X-100 (PBS-Tx) for 1 h at RT. Slides were then placed in PBS-Tx/1% BSA (PBS-Tx-B) for 30 min at
751 RT. Sperm were then incubated with primary antibodies in PBS-Tx-B overnight at 4 °C. After washing
752 three times in PBS-Tx-B for 5 min each, slides were incubated with secondary antibodies for 1 h at RT
753 in PBS-Tx-B. After washing three times in PBS, nuclei were stained with 2 µg/mL Hoechst 33342 in PBS
754 (Sigma Aldrich) and slides were mounted with DAKO mounting media (Agilent).

755 Sarkosyl protocol for mouse sperm - Mouse sperm from caudae epididymides were collected
756 in 1 mL PBS 1X, washed by centrifugation for 5 min at 500 g and then resuspended in 1 mL PBS 1X.
757 Sperm cells were spread onto slides pre-coated with 0.1% poly-L-lysine (Epredia), treated or not for
758 5 min with 0.2% sarkosyl (Sigma) in Tris-HCl 1 mM, pH7.5 at RT and then fixed in PBS/4% PFA for 45 s
759 at RT. After washing twice for 5 min with PBS, sperm were permeabilized with PBS/0.1% Triton X-100
760 (Sigma Aldrich) for 15 min at RT and unspecific sites were blocked with PBS/0.1% Triton X-100/2% NGS
761 for 30 min at RT. Then, sperm were incubated overnight at 4 °C with primary antibodies diluted in
762 PBS/0.1% Triton X-100/2% NGS. Slides were washed three times with PBS/0.1% Triton X-100 before
763 incubating with secondary antibody diluted in PBS/0.1% Triton X-100/2% NGS for 90 min at RT. Finally,
764 sperm were washed three times in PBS/0.1% Triton X-100, adding 2 µg/mL Hoechst 33342 (Sigma
765 Aldrich) during the last wash to counterstain nuclei. Slides were mounted with DAKO mounting media
766 (Agilent).

767 Image acquisition – For all immunofluorescence experiments, images were acquired using 63X
768 oil objectives on a multimodal confocal Zeiss LSM 710 or Zeiss AxioObserver Z1 equipped with
769 ApoTome and AxioCam MRm or NIKON eclipse A1R/Ti2. Images were processed using Fiji [75] and
770 Zeiss ZEN (Carl Zeiss, version 3.4). Figures for cultured cells were arranged using QuickFigures [76].

771 Image analysis – To quantify the number of spots in the flagella the brightfield and fluorescent
772 images were preprocessed with a home-made macro in ImageJ (https://imagej.net/ij/) to improve the
773 contrast and decrease noise. Masks of whole cells, midpieces and head were then realised using Ilastik
774 [77] on brightfield and fluorescent images. The masks of midpieces and head were then subtracted
775 from the mask of the whole cell to obtain a mask of the flagella. This mask was used as an ROI to
776 quantify intensity maxima in the flagella of control and CCDC146 expressing cells. To compare the

777 number of spots in images with a random distribution, we quantified the total number of intensity
778 maxima in the fluorescent image and a new image was generated with a random distribution of the
779 same number of spots. Subsequently, the same quantification of intensity maxima in the flagella was
780 carried out on the random images. A second home-made macro in ImageJ allows to automatize these
781 two steps. Both macros are available on demand.

782

783 Expansion microscopy (U-ExM)

784 Coverslips used for either sample loading (12 mm) or image acquisition (24 mm) were first
785 washed with absolute ethanol and dried. They were then coated with poly-D-lysine (0.1 mg/mL) for
786 1 h at 37 °C and washed three times with ddH2O before use. Sperm from cauda epididymides or human
787 sperm from straws were washed twice in PBS. $1x10^6$ sperm cells were spun onto 12-mm coverslips for
788 3 min at 300 g. Crosslinking was performed in 1 mL of PBS/1.4% formaldehyde/2% acrylamide
789 (ThermoFisher) for 5 h at 37 °C in a wet incubator. Cells were embedded in a gel by placing a 35-µL
790 drop of a monomer solution consisting of PBS/19% sodium acrylate/10% acrylamide/0.1% N,N'-
791 methylenbisacrylamide/0.2% TEMED/0.2% APS (ThermoFisher) on parafilm and carefully placing
792 coverslips on the drop, with sperm facing the gelling solution. Gelation proceeded in two steps: 5 min
793 on ice followed by 1 h at 37 °C. Coverslips with attached gels were transferred into a 6-well plate for
794 incubation in 5 mL of denaturation buffer (200 mM SDS, 200 mM NaCl, 50 mM Tris in ddH2O, pH 9) for
795 20 min at RT until gels detached. Then, gels were transferred to a 1.5-mL microtube filled with fresh
796 denaturation buffer and incubated for 90 min at 95 °C. Gels were carefully removed with tweezers and
797 placed in beakers filled with 10 mL ddH2O to cause expansion. The water was exchanged at least twice
798 every 30 min. Finally, gels were incubated in 10 mL of ddH2O overnight at RT. The following day, a 5-
799 mm piece of gel was cut out with a punch. To remove excess water, gels were placed in 10 mL PBS for
800 15 min, the buffer was changed, and incubation repeated once. Subsequently, gels were transferred
801 to a 24-well plate and incubated with 300 µL of primary antibody diluted in PBS/2% BSA at 37 °C for
802 3 h with vigorous shaking. After three washes for 10 min in PBS/0.1% Tween 20 (PBS-T) under agitation,
803 gels were incubated with 300 µL of secondary antibody in PBS/2% BSA at 37 °C for 3 h with vigorous
804 shaking. Finally, gels were washed three times in PBS-T for 10 min with agitation. Hoechst 33342
805 (2 µg/mL) was added during the last wash. The expansion resolution was between 4X and 4.2X
806 depending on sodium acrylate purity. For image acquisition, gels were placed in beakers filled with
807 10 mL ddH2O. Water was exchanged at least twice every 30 min, and then expanded gels were
808 mounted on 24-mm round poly-D-lysine-coated coverslips, placed in a 36-mm metallic chamber for
809 imaging. Confocal microscopy was performed using either a Zeiss LSM 710 using a 63x oil objective or

widefield was performed using a Leica THUNDER widefield fluorescence microscope, using a 63x oil objective and small volume computational clearing.

Ccdc146 expression

Testis from HA-CCDC146 pups were collected at days 9, 18, 26 and 35 after birth and directly cryopreserved at -80 °C before RNA extraction (n=3 for each day). RNA was extracted as follow. Frozen testes were placed in RLT buffer (Qiagen)/1% β-mercaptoethanol (Sigma), cut in small pieces and lysis performed for 30 min at RT. After addition of 10 volumes of TRIzol (5 min, RT, ThermoFisher) and 1 volume of chloroform (2 min, RT, Sigma Aldrich), the aqueous phase was recovered after centrifugation at 12 000 g, 15 min, 4 °C. RNA was precipitated by the addition of one volume of isopropanol (Sigma) and of glycogen (20 mg/mL, ThermoFisher) as a carrier, tube was placed overnight at -20 °C. The day after, after centrifugation (15 min, 12 000 g, 4 °C), RNA pellet was washed with ethanol 80%, air-dried and resuspended in 30 µl of ultrapure RNAse free water (Gibco). RNA concentrations were determined by using the Qubit RNA assay kit (ThermoFisher). 800 ng of total RNA were used to perform the RT step using the iScript cDNA synthesis kit (Bio-Rad) in a total volume of 20 µL. Gene expression was assessed by qPCR (1 µL of undiluted cDNA in a final volume of 20 µL with the appropriate amount of primers, see table 1) using the SsoAdvanced Universal SYBR Green Supermix (Bio-Rad). The qPCR program used was 94 °C 15 min, (94 °C 30 s, 58 °C 30 s, 72 °C 30 s) x40 followed by a melt curve analysis (58 °C 0.05 s, 58–95 °C 0.5-°C increment 2–5 s/step). Gene expression was calculated using the $2^{-\Delta CT}$ method. Results are expressed relative to *Ccdc146* expression on day 9.

	Forward primer		Reverse primer	
Genes	Sequence	Concentration (nM)	Sequence	Concentration (nM)
Ccdc146	5'-TGCTGCATGACGCCGTGATG-3'	750	5'-GGAGACCTCCGTGGAGAATGCTTC-3'	500
Hprt	5'-CCTAATCATTATGCCGAGGATTTGG-3'	500	5'-TCCCATCTCCTTCATGACATCTCG-3'	250
Actb	5'-CTTCTTTGCAGCTCCTTCGTTGC-3'	250	5'-AGCCGTTGTCGACGACCAGC-3'	250

829

830 CCDC146 detection by WB

831 Protein extraction from whole sperm head and sperm flagella – Spermatozoa from HA-
832 CCDC146 males (9 weeks old) were isolated from both epididymis in 1 mL PBS and washed twice with
833 PBS by centrifugation at RT (5 min, 500 g). Half of the sperm were incubated with 1X protease inhibitor
834 cocktail (mini Complete EDTA-free tablet, Roche Diagnostic), incubated for 15 min on ice and
835 sonicated. Separated flagella were isolated by centrifugation (600 g, 20 min, 4 °C) in a Percoll gradient.
836 Percoll concentrations used were 100%, 80%, 60%, 34%, 26%, 23%, and sperm flagella were isolated
837 from the 60% fraction and heads form the 100% fraction. Samples were washed with PBS by
838 centrifugation (500 g, 10 min, 4 °C). Whole sperm or sperm flagella were incubated in 2X Laemmli
839 buffer (Bio-Rad), heated at 95 °C for 10 min and centrifuged (15 000 g, 10 min, 4 °C). The supernatants
840 were incubated with 5% β-mercaptoethanol, boiled (95 °C, 10 min), cooled down and placed at -20 °C
841 until use.

842

843 Proteins solubilization from total sperm – HA-CCDC146 sperm were recovered from caudae
844 epididymides in 1 mL PBS and washed twice in 1 mL PBS by centrifugation 500 g, 5 min. Lysis was then
845 performed for 2 h at 4 °C on wheel in either Chaps buffer (10 mM Chaps / 10 mM HEPES / 137 mM
846 NaCl / 10% Glycerol), in RIPA Buffer (Pierce IP Lysis buffer, ThermoFisher), in Tris 10 mM / HCl 1 M
847 buffer or in Tris 10 mM / HCl 1 M / 0.2 to 0.8% sarkosyl buffer. After centrifugation 15 000 g, 4 °C,
848 15 min, the supernatants were recovered and 5% of β-mercaptoethanol added. After boiling (95 °C,
849 10 min), the samples were cooled down and placed at -20 °C until use.

850 Western blot – The different protein lysates were fractionated on 5-12% SDS-PAGE precast
851 gels (Bio-Rad) and transferred onto Trans-Blot Turbo Mini 0.2 µm PVDF membranes using the Trans-
852 Blot Turbo Transfer System (Bio-Rad) and the appropriate program. Membranes were then blocked in
853 PBS/5% milk/0.1% Tween 20 (PBS-T) for 2 h at RT before incubating with the primary antibody in PBS-
854 T overnight at 4 °C with agitation. Membranes were then washed three times for 5 min in PBS-T and
855 incubated with the secondary HRP-antibody in PBS-T for 1 h at RT. After three washes (PBS-T, 10 min),
856 the membrane was revealed by chemiluminescence using the Clarity ECL substrate (Bio-Rad) and
857 images were acquired on a Chemidoc apparatus (Bio-Rad).

858 Transmission electron microscopy

859 Testis from adult mice were fixed in PBS/4% paraformaldehyde (PFA). They were then decapsulated
860 from the tunica albuginea and the seminiferous tubules were divided into three to four pieces using a

861 razor blade (Gillette Super Sliver). The seminiferous tubules were incubated for 60 min at RT in fixation
862 buffer (100 mM HEPES pH7.4, 4 mM CaCl2, 2.5% glutaraldehyde, 2% PFA, all from Sigma Aldrich) and
863 then the buffer was exchanged with fresh fixation buffer and the samples left overnight fixed at 4 °C.
864 After washing three times for 10 min in 100 mM HEPES pH 7.4, 4 mM CaCl2, samples were post-fixed
865 in 1% osmium tetroxide (Carl Roth, Karlsruhe, DE) in distilled water for 120 min at 4 °C. After three
866 additional 10-min washes in distilled water, the tissue pieces were embedded in 1.5% DifcoTM Agar
867 noble (Becton, Dickinson and Company, Sparks, MD, US) and dehydrated using increasing
868 concentrations of ethanol. The samples were then embedded in glycidyl ether 100 (formerly Epon 812;
869 Serva, Heidelberg, Germany) using propylene oxide as an intermediate solvent according to the
870 standard procedure. Ultrathin sections (60-80 nm) were cut with a diamond knife (type ultra 35°;
871 Diatome, Biel, CH) on the EM UC6 ultramicrotome (Leica Microsystems, Wetzlar, Germany) and
872 mounted on single-slot pioloform-coated copper grids (Plano, Wetzlar, Germany). Finally, sections
873 were stained with uranyl acetate and lead citrate [78]. The sectioned and contrasted samples were
874 analyzed under a JEM-2100 transmission electron microscope (JEOL, Tokyo, JP) at an acceleration
875 voltage of 80 kV. Images were acquired using a 4080 x 4080 charge-coupled device camera (UltraScan
876 4000 - Gatan, Pleasanton, CA, US) and Gatan Digital Micrograph software. The brightness and contrast
877 of images were adjusted using the ImageJ program.

878 Scanning electron microscopy

879 The two epididymides of mature males were recovered in 1 mL of 0.1 M sodium cacodylate buffer (pH
880 7.4, Electron Microscopy Sciences) and the sperm were allowed to swim for 15 min at 37 °C. After
881 centrifugation for 10 min, 400 g, RT, the supernatant was discarded and the pellet resuspended in
882 primary fixating buffer (2% glutaraldehyde/0.1 M sodium cacodylate buffer, pH 7.4, Electron
883 Microscopy Sciences) for 30 min at 4 °C. After washing three times in 0.1 M sodium cacodylate buffer
884 (400 g, 10 min), the pellet was submitted to post fixation using 1% Osmium tetroxide 2% (OsO4,
885 Electron Microscopy Sciences) in 0.1 M sodium cacodylate buffer for 30 min at 4 °C. Fixed cells were
886 washed three times in 0.1 M sodium cacodylate buffer (400 g, 5 min), the sample was then placed on
887 a coverslip and treated with Alcian blue 1% (Electron Microscopy Sciences) to improve attachment.
888 The sample was then dehydrated in graded ethanol series: 50%, 70%, 80%, 90%, 96% and 100%
889 (10 min, once each). Final dehydration was performed for 10 min in a v/v solution of 100%
890 ethanol/100% Hexamethyldisilazane (HMDS) followed by 10 min in 100% HMDS. Samples were left to
891 dry overnight before performing metallization. Samples were analyzed using a Zeiss Ultra 55
892 microscope at the C.M.T.C. – Consortium des Moyens Technologiques Communs (Material
893 characterization platform), Grenoble INP.

894 Statistical analysis

895 Statistical differences were assessed by applying unpaired t tests, Mann-Whitney tests or one-way
896 ANOVA using GraphPad Prism 8 and 9. Histograms show mean ± standard deviation, and p-values were
897 considered significant when inferior to 0.05.

898 Antibodies used

Primary antibodies				
Target	**Host species**	**Reference**		**Dilution**
CCDC146	Rabbit	Atlas Antibodies	HPA020082	IF: 1/200 U-ExM: 1/200
Centrin, 20H5	Mouse	Merck	04-1624	IF: 1/200
γ-tubulin	Mouse	Santa Cruz Biotechnology	sc-17787	IF: 1/500
β-tubulin	Guinea pig	Geneva Antibody Facility	AA344-GP	IF: 1/500
β-tubulin	Rabbit	Cell Signaling Technology	2128	IF: 1/100
PCM1 (G-6)	Mouse	Santa Cruz Biotechnology	sc-398365	IF: 1/200
α-tubulin	Mouse	Geneva Antibody Facility	AA-345	U-ExM: 1/250
β-tubulin *			AA-344	IF: 1/500
POC5	Rabbit	Bethyl	A303-341A	IF: 1/250 U-ExM: 1/200
High Affinity (HA)	Rat	Roche	11867423001	IF: 1/400 U-ExM: 1/400 WB: 1/2500

High Affinity (HA)	Rabbit	Cell Signaling Technology	3724	U-ExM: 1/100
High Affinity (HA)	Rabbit	Sigma Aldrich	H6908	U-ExM: 1/200
HA Tag Alexa Fluor®-488-conjugated Antibody		Cell Signalling	28427	IF:1/400
Dpy19L2	Rabbit	**		IF: 1/100

899

Target	**Fluorophore**	**Reference**		**Dilution**
Goat anti-Rabbit	Alexa Fluor 488	Jackson ImmunoResearch	111-545-144	IF: 1/800 U-ExM: 1/250
Goat anti-Mouse	DyLight 549	Jackson ImmunoResearch	115-505-062	IF: 1/400
Goat anti-Guinea Pig	Alexa Fluor 647	Invitrogen	A-21450	IF: 1/800
Goat anti-Rabbit	Alexa Fluor 568	Life Technologies	A11036	U-ExM: 1/250
Goat anti-Mouse	Alexa Fluor 488	Life Technologies	A11029	U-ExM: 1/250
Goat anti-Rat	Alexa Fluor 549	Jackson ImmunoResearch	112-505-175	IF: 1/800
Goat Anti-Rat	HRP conjugate	Merck	AP136P	1/10 000

900

901 *α-tubulin and β-tubulin were used together and noted as α+β-tubulin

902 **Dpy19l2 antibodies are polyclonal antibodies produced in rabbit that were raised against
903 RSKLREGSSDRPQSSC and CTGQARRRWSAATMEP peptides corresponding to amino acids 6-21 and 21-
904 36 of the N-terminus of mouse Dpy19l2, as described in [79].

905 **Acknowledgments.**

906 This work was supported by INSERM, CNRS, Université Grenoble Alpes, the French Agence Nationale
907 pour la Recherche (ANR) grants ‘‘MAS-Flagella’’ (ANR-19-CE17-0014), and “FLAGELOME” (ANR-19-

CE17-0014) to P.F.R., “MIP-MAP” (ANR-20-CE13-0005) to CA, the Direction Générale de l’Offre de Soin (DGHOS) for the program PRTS 2014 to P.F.R., the Fondation Maladies Rares (FMR)- grant ‘‘Whole genome sequencing of subjects with Flagellar Growth Defects (FGD)’’ financed by for the program Séquençage à haut débit 2012 to P.F.R. and the European Research Council (ERC) ACCENT Starting Grant 715289 to P.G.

915 # Figure legends

916 **Figure 1: Identification of two *CCDC146* gene variants in MMAF patients**

917 (A) Structure of the canonical *CCDC146* gene transcript showing the position of the variants and their
918 impact on translation. Variants are annotated according to HGVS recommendations. Position of the
919 observed variants in both probands. (B) Electropherograms indicating the homozygous state of the
920 identified variant: variant c.1084C>T is a nonsense mutation, and c.2112Del is a single-nucleotide
921 deletion predicted to induce a translational frameshift.

922 **Figure 2: *Ccdc146* KO mice are infertile and KO sperm exhibit a typical "multiple morphological**
923 **abnormalities of the flagellum (MMAF)" phenotype.**

924 (A) Number of pups produced by wild-type (+/+, WT), *CCDC146* heterozygote (+/-) and *Ccdc146* knock-
925 out (-/-, KO) males (3 males per genotype) after mating with fertile WT females (2 females per male)
926 over a period of three months. (B) Sperm concentration and (C) Comparison of testis weights (mg).
927 (D) Illustration of WT and KO sperm morphologies stained with Papanicolaou and observed under optic
928 microscopy. Scale bars of images represents 10 µm. (E) Histograms showing proportions of total, head
929 and flagella morphological anomalies (mean ± SD) for each *Ccdc146* genotype (n=5). (F) sperm mobility.
930 (A-D, F) Statistical comparisons were based on ordinary one-way ANOVA tests and (E) statistical
931 significance was assessed by applying an unpaired t-test; p-values: **** $p<0.0001$; *** $p<0.001$,
932 ** $p<0.01$, * $p<0.05$.
933

934 **Figure 3: Histological evidence that spermiogenesis is disrupted in *Ccdc146* KO males and leads to a**
935 **strong decrease in sperm concentration in the epididymis.**
936 (A) Transversal sections of WT and KO testes stained with hematoxylin and eosin. The upper images
937 show the sections at low magnification (Scale bars 50 µm) and the lower images are an enlargement
938 of the dotted square (scale bars 10 µm). In the KO, spermatid nuclei were very elongated and
939 remarkably thin (green arrow heads) and no flagella were visible within the seminiferous tubule lumen.
940 (B) Transversal sections of WT and KO epididymides stained with hematoxylin and eosin. Despite
941 similar epididymis section diameters in WT and KO testes, KO lumen were filled with round cells and
942 contained few spermatozoa with abnormally-shaped heads and flagella. The upper images show the
943 sections at low magnification (scale bars 50 µm) and the lower images are an enlargement of the
944 dotted square (scale bars 10 µm).
945

946 **Figure 4: CCDC146 has a centriolar and pericentriolar localization in interphase somatic HEK-293T**
947 **cells.**

948 HEK-293T cells were immunolabeled for β-tubulin (green), centrin (yellow) and CCDC146 (magenta).
949 DNA was stained with Hoechst (blue). (A) CCDC146 localized to centrioles and/ or to the pericentriolar
950 material in interphase cells. The centrosome area of two cells are shown enlarged in A1 and A2. (B) In
951 serum starved cells with primary cilia, CCDC146 localized to the basal body of primary cilia. The basal
952 body of two cells are shown enlarged in B1 and B2. CCDC146 was also present as dotted signal
953 resembling the pattern for centriolar satellite proteins. Scale bars µm and 2 µm on zoomed images.

954 **Figure 5: CCDC146 is a microtubule-associated protein (MAP) associating with microtubule-based**
955 **structures throughout the cell cycle.**

956 HEK-293T cells were immunolabeled with anti-β-tubulin (panels A-E, green), anti-γ tubulin (yellow,
957 panel A), anti-centrin (yellow panels C-E), and anti-CCDC146 (panels A-E, magenta) Abs. DNA was
958 stained with Hoechst (blue). (A) In synchronized HEK-293T cells, CCDC146 is observed associated with
959 mother centrioles and their corresponding procentrioles during centriole duplication. (B-E) In non-
960 synchronized cells, CCDC146 is observed associated with spindle poles (B-E) and with microtubule
961 (MT) tips during metaphase (B), with the central spindle during anaphase (C), with the midzone during
962 telophase (D), and with the midbody during cytokinesis (E). Images on the right show the enlargement
963 of the dotted square in the left image. Scale bar of zoomed images 2 µm.

964 **Figure 6: CCDC146 protein is present in epididymal spermatozoa in mouse and *Ccdc146* mRNA is**
965 **expressed in late spermatocyte and in spermatids;**

966 (A) CCDC146 is retained in epididymal sperm. Western blot of HA-tagged epididymal whole sperm
967 shows a band (arrow) corresponding to HA-tagged CCDC146 (HA-CCDC146), whereas no band was
968 observed with WT epididymal sperm, demonstrating the specificity of the band observed in HA-
969 CCDC146 sperm lane. Sperm extracts obtained from flagella and head fractions of WT and HA-CCDC146
970 were also analysed and the presence of HA-CCDC146 was revealed by an anti-HA Ab in flagella fraction
971 from HA-CCDC146 sperm only. Loading control (ponceau staining) of the gel is shown on the right. (B)
972 Image of heads and flagella fractions. (C) mRNA expression levels of *Ccdc146* relative to *Actb* and *Hprt*
973 in HA-CCDC146 mouse pups' testes during the first wave of spermatogenesis (n=3). Extremely low
974 *Ccdc146* expression was detected at day 9, corresponding to testes containing spermatogonia and
975 Sertoli cells only. *Ccdc146* expression was observed from postnatal day 18 (formation of secondary
976 spermatocytes), peaked at day 26 (formation of elongated spermatids), and subsequently decreased

977 from day 35 (formation of spermatozoa), suggesting that *Ccdc146* is particularly expressed in
978 elongated spermatids during spermatogenesis.

979 **Figure 7: CCDC146 localizes to the flagellum of mouse epididymal spermatozoa.**

980 (A) Mouse epididymal spermatozoa observed with conventional IF. WT and HA-CCDC146 sperm were
981 labeled with anti-HA Tag Alexa Fluor® 488-conjugated 3 (green) Abs (anti-HA #1). DNA was stained
982 with Hoechst (blue). The upper image shows the staining of a WT sperm and the lower images, the
983 staining of a HA-CCDC146 sperm. A punctuate signal is observed in HA-CCDC146 sperm (Scale bars
984 5 µm). (B) Quantification of the density of dots per square µm (μm^2) and statistical significance
985 between WT and HA-CCDC146 sperm was assessed by Mann-Whitney test, p value as indicated. (C)
986 Mouse epididymal spermatozoa observed with expansion microscopy. HA-CCDC146 sperm were
987 immunolabeled with anti-β-tubulin (red), anti-HA #2 (green) Abs and DNA was stained with Hoechst
988 (blue). The right image shows the sperm with merged immunostaining. (Scale bars 5 µm) (D) Mouse
989 epididymal spermatozoa observed with expansion microscopy. The lower images show the staining,
990 HA-CCDC146 (red), tubulin (green) and merge observed in the principal piece of the flagellum. Strong
991 red punctiform signals were observed at the level of axonemal breakages induced by the expansion
992 process. White arrows indicate the zones of the micro breaks. Scale bars 10 µm.

993 **Figure 8: CCDC146 localizes to the flagellum but not to the centrioles of ejaculated human**
994 **spermatozoa.**

995 (A) Human ejaculated sperm were immunolabeled with Abs recognizing centrin (yellow), CCDC146
996 (magenta), and β-tubulin (green). DNA was stained with Hoechst (blue). (A1-A3) enlargement of dotted
997 square focused on sperm neck: no colocalization between CCDC146 and centrin. (A4) A faint signal for
998 CCDC146 is present along the length of the sperm flagellum. Scale bar of zoomed images: 1 µm. (B)
999 Human ejaculated sperm observed by expansion microscopy. Sperm were immunolabeled with anti-
1000 CCDC146 (magenta) and anti-β-tubulin (green) abs, and DNA was stained with Hoechst (blue). B1 and
1001 B5 show strong staining for CCDC146 in the axoneme, B3 shows the localization of the axoneme
1002 through tubulin staining. B2, B4 and B6 show enlargements of the dotted squares focused on the
1003 sperm neck. CCDC146 did not colocalize with the centrioles at the base of the axoneme. The CCDC146
1004 staining observed probably corresponds to non-specific labeling of mitochondria, as suggested by
1005 Figure 8—figure supplement 1. Scale bars 5 µm.

1006 **Figure 9: CCDC146 localizes to the microtubule doublets of the axoneme in human and mouse**

1007 (A) Sperm was double-stained with anti-tubulin (green) and anti-CCDC146 (magenta) Abs and observed
1008 by expansion microscopy. Scale bar 10 µm. (B) Measurement of the green-tubulin signal intensity

1009 perpendicularly to the axoneme is quite characteristic with two peaks corresponding to the left and
1010 right microtubule doublet. It identifies five axonemal compartments (left outer, left doublet (Tub1),
1011 central pair (CP), right doublet (Tub2), and right outer). To determine the CP area, the distance (d)
1012 between the center of the flagella and the peak of Tub2 was measured, and all fluorescent dots located
1013 in between -d/4 to +d/4 from the center were counted as CP dots. (C) Example of the measurement of
1014 the tubulin (green) and the CCDC146 signal intensities measured at the white rectangle (2). The image
1015 corresponds to the orange rectangle in A. In this example, the CCDC146 signal is localized in the right
1016 doublet of microtubules (Tub2). (D) The position of the CCDC146 signal with respect to the tubulin
1017 signal was measured along the entire flagellum. Each CCDC146 signal was assigned to a different
1018 compartment of the axoneme, allowing to obtain an histogram showing the distribution of CCDC146
1019 labeling in ejaculated human sperm (n=2, 38 dots analysed). (E) Flagellum of a mouse epididymal
1020 spermatozoa observed with expansion microscopy. HA-CCDC146 sperm were immunolabeled with
1021 anti-HA #2 (red) and anti-β-tubulin (green). The upper image shows the sperm with merged
1022 immunostaining, and the lower images, the staining (red, green, and merge) observed in the principal
1023 piece of the flagellum. Scale bars 10 µm.

1024 **Figure 10: CCDC146 is solubilized by sarkosyl and sarkosyl treatment enhances IF signal**

1025 (A) Western blot of WT and HA-CCDC146 sperm extract solubilized with N-lauroylsarcosine (sarkosyl),
1026 an anionic detergent. Sarkosyl was used at increasing concentrations (0.2 and 0.4%). The presence of
1027 HA-CCDC146 was detected by an anti-HA Ab. (B) Western blot of WT and HA-CCDC146 sperm extracts
1028 solubilized with alternative detergents (RIPA, CHAPS, Tris-HCl) and whole sperm extract solubilized in
1029 Laemmli. The presence of HA-CCDC146 was revealed by an anti-HA Ab. (C) Epididymal HA-CCDC146
1030 sperm (C1-C2) and WT sperm (C3-C4), treated with sarkosyl (5 min, 0.2% sarkosyl) or not (NT), were
1031 immunostained to reveal the HA-tag (red) and counterstained with Hoechst (blue). (C1) Without
1032 treatment, a faint CCDC146 signal (white arrow heads) is observed along the flagellum from HA-
1033 CCDC146 sperm. (C2) Treatment with sarkosyl enhanced the HA-CCDC146 signal along the sperm
1034 flagellum. (C3) The HA signal present the midpiece is likely non-specific since it is present in WT non-
1035 treated (NT) sperm. See also Figure 10—Figure supplement 1B suggesting that this signal is due to
1036 secondary Abs. (C4) The HA signal in WT sperm is not enhanced by sarkosyl treatment. Scale bars
1037 10 µm.

1038 **Figure 11: The absence of CCDC146 causes defects of the head-tail coupling apparatus in epididymal**
1039 **spermatozoa and duplication and mislocalization of centriole in testicular sperm.**

1040 (A) Scanning electron microscopy of WT and *Ccdc146* KO epididymal spermatozoa showed aberrant
1041 head morphologies and irregular head-tail coupling apparatus (HTCA) linking the sperm head with the

1042 flagellum. There is a great variability in the morphological damage, with sperm presenting almost intact
1043 HTCA (A2) whereas other were strongly impacted by the absence of the protein (A3-4). Scales bars 200
1044 nm. (B) Testicular spermatozoa from WT (B1) and *Ccdc146* KO (B2-B6) mice immunolabeled with anti-
1045 β-tubulin (magenta) and anti-centrin (B1-B3) or anti-γ-tubulin (B4-B6) (green) Abs. Centrioles appeared
1046 to be normal (B2) in some spermatozoa, separated but partially attached to the head (B3, B4),
1047 completely detached from the sperm head (B5) or duplicated (B6). Scale bar 10 µm.

1048 **Figure 12: Absence of elongation of axonemal microtubules at the base of the distal centriole.**

1049 (A) In WT spermatids (A1), the proximal centriole (PC) is linked to the base of the compacting nucleus
1050 (Nu) through the basal plate (BP) and the capitulum (Ca), and the distal centriole (DC) is embedded in
1051 the segmented column (SC). All these sperm-specific cytoskeletal structures make up the HTCA. At the
1052 base of the distal centriole, axonemal microtubules (Ax) grow. In *Ccdc146* KO elongating spermatids
1053 (A2), the overall structure of the HTCA is conserved, with the presence of the centrioles and the
1054 accessory cytoskeletal structures. However, no axonemal microtubules are visible, emerging from the
1055 DC. (B) The adjunct (Ad) of the proximal centriole is also preserved in *Ccdc146* KO spermatids. (C) Serial
1056 sections of the HTCA of a *Ccdc146* KO spermatid confirm the absence of axonemal microtubules at the
1057 base of the DC during spermatid elongation. Scale bars 1 µm.

1058 **Figure 13: Analysis of stages of spermatogenesis by IF reveals acrosome formation and manchette**
1059 **elongation defects in *Ccdc146* KO spermatids.**

1060 Cross sections of WT (A1-D1) and *Ccdc146* KO (A2-D2) testes showing different stages of mouse
1061 spermatogenesis (I, VII-XII). Stages were determined by double immunostaining for β-tubulin (red;
1062 manchette elongation) and DPY19L2 (green; acrosome localization), and DNA was stained with
1063 Hoechst (blue). (A1/A2) At stage VII-VIII, acrosome spreading on round spermatids appeared similar
1064 between WT and KO. However, very few mature spermatozoa lined the lumen in the KO. (B1/B2) Cell
1065 orientations appeared random from stage IX-X in the KO and the tubules contained more advanced
1066 spermatid stages. Random orientations of cells are evidenced by manchette cross-sections in various
1067 planes. (C2) Abnormal acrosomes of elongating KO spermatids are observed by stage XII. (D1/D2) The
1068 manchette of elongated spermatids at stage I-III was longer in the KO compared with the WT. Insets in
1069 A1-D1 and A2-D2 show typical spermatids from stages I-XII from WT and KO males, respectively,
1070 showing details of acrosome formation (green) and manchette elongation (red). Scale bars stages VII-
1071 VIII 20 µm, scale bars IX-X, XII and I-III 10 µm.

1072 **Figure 14: TEM of elongating spermatids from *Ccdc146* KO male shows ultrastructural defects of the**
1073 **manchette.**

1074 (A, B) Ultrastructural analysis of the manchette in WT elongating spermatids shows the normal thin
1075 perinuclear ring, anchored below the acrosome (blue arrows) and allowing a narrow array of
1076 microtubules to anchor. (C-F) In elongating spermatids from *Ccdc146* KO animals, the perinuclear ring
1077 was abnormally broad, usually located on one side of the spermatid (red arrows), creating an
1078 asymmetric and wide bundle of microtubules. The resulting manchette was wider and often longer
1079 than in WT animals (black double arrows). (F) The tubulin nucleation location was sometimes ectopic
1080 in the KO (red arrow) and coincided with irregularly shaped sperm heads. Scale bars 1µm.

1081 **Figure 15: The axonemes of *Ccdc146* KO spermatids present multiple defects visible under TEM.**

1082 (A1) A longitudinal section of a WT flagellum shows a typical structure of the principal piece, with outer
1083 dense fibers (ODF) at the periphery, microtubules (MT) in the center, and mitochondria (Mi) aligned
1084 along the flagellum. (A2) A longitudinal section of a *Ccdc146* KO flagellum shows a disorganized
1085 midpiece, with altered mitochondria, the presence of an amorphous fibrous sheath (FS) and altered
1086 microtubules. (B) Longitudinal section of a *Ccdc146* KO sperm showing dispersed and non-assembled
1087 flagellar material in a cytoplasmic mass. The right-hand image is the enlargement of the red square,
1088 showing the presence of an external ring of mitochondria surrounding an outer dense fiber ring devoid
1089 of microtubular material. (C) Longitudinal section of another *Ccdc146* KO sperm showing a similar
1090 abnormal midpiece structure. The right-hand image is the enlargement of the red square, showing the
1091 presence of an external ring of mitochondria surrounding an outer dense fiber ring devoid of
1092 microtubular material. Scale bars as indicated.

1093 **Figure 16. Spermatid head shape is aberrant in the absence of CCDC146.**

1094 Comparative ultrastructural analysis of the spermatid head in WT (A-D) and *Ccdc146* KO (E-H) testis
1095 sections. (A, E) Spermatid nuclei at the beginning of elongation. KO spermatid nuclei showing nuclear
1096 membrane invaginations and irregular shape that were not present in the WT (red arrow). The
1097 acrosome of KO spermatids appeared intact. (B, F) Morphology of nuclei in elongating spermatids.
1098 Whereas nucleus elongation is symmetric in the WT, in the *Ccdc146* KO, more pronounced head
1099 invaginations are observed (red arrow). (C, G) Elongated spermatids. Although nuclear condensation
1100 appeared normal in both WT and KO nuclei, vacuolization is observed in KO nucleus (white arrow). (D,
1101 H) Elongated KO spermatids showed malformed elongated nuclear shapes with frequent invaginations
1102 (white arrow) and absence of flagella (H) compared to the WT (D). The acrosome of KO spermatids
1103 showed numerous defects such as detachment induced by swelling/bubbling of the plasma membrane
1104 (blue arrow heads). Scale bars 1 µm.

1105 **Figure 1—Figure supplement 1. Detailed semen parameters of both MMAF individuals harboring a**
1106 ***CCDC146* variant.**
1107 Values are percentages unless specified otherwise. NA: not available, Reference limits (5th centiles
1108 and their 95% confidence intervals) according to World Health Organization (WHO) standards (Cooper
1109 et al., 2010). Patient 08IF39 variant c.1084C>T and patient O9IF26 variant c.2112Del.
1110

1111 **Figure 1—Figure supplement 2. Relative mRNA expression levels for human and mouse *Ccdc146***
1112 **transcripts.**

1113 (A) *Ccdc146* mRNA levels measured in different tissues/cells in humans using Affymetrix microarrays
1114 (data available from the Genevestigator database, https://genevestigator.com). Red rectangles
1115 highlight the high expression level in male reproductive organs. (B) Similar data for mice. The level of
1116 expression is medium in mice. Data were generated with Genevestigator (Hruz T, Laule O, Szabo G,
1117 Wessendorp F, Bleuler S, Oertle L, Widmayer P, Gruissem W and P Zimmermann (2008) Genevestigator
1118 V3: a reference expression database for the meta-analysis of transcriptomes. Advances in
1119 Bioinformatics 2008, 420747)

1120 **Figure 2—Figure supplement 1. Molecular strategy used to generate *Ccdc146* KO mice by**
1121 **CRISPR/Cas9.**

1122 (A) The exonic structure of mouse *Ccdc146* is shown and the coding sequence indicated in black. (B)
1123 Exon 2, the first coding sequence, was targeted by an RNA guide (5'-CCT ACA GTT AAC ATT CGG G-3)
1124 and the Cas9 induced in line 1 a deletion of four nucleotides upstream the PAM sequence, as indicated
1125 by the red box. Electropherogram presenting the WT and the homozygote deletion are shown. (C) In
1126 line 2, the Cas9 induced an insertion of 250 nucleotides. Sperm morphology of F2 males from line 2
1127 was severely damaged. Scale bars 30 µm. (D) Comparison of sperm parameters in WT, heterozygote
1128 and KO animals from line 2; ND not determined.

1129 **Figure 2—Figure supplement 2. Increased levels of apoptosis in testes from *Ccdc146* KO mice.** The
1130 TUNEL assay was used to visualize double-strand DNA breaks, as an indication of the level of apoptosis
1131 during WT and KO spermatogenesis. (A) Comparison of the % of tubules per testis cross-section
1132 containing at least one fluorescent (TUNEL-positive) cell in WT, heterozygote, and *Ccdc146* KO animals.
1133 Number of sections counted per genotype n=13-20, 3 different mice per genotype. (B) Control testis
1134 section treated with H_20_2. (C) The majority of TUNEL-positive cells in the WT corresponded to
1135 pachytene cells undergoing meiosis (C, WT zoomed image) whereas the localization of TUNEL-positive
1136 cells in KO was more scattered. Statistical comparisons according to ordinary one-way ANOVA test
1137 (**** $p<0.0001$; *** $p<0.001$, ** $p<0.01$, * $p<0.05$). Scale bars of zoomed images 50 µm.

1138 **Figure 4—Figure supplement 1. DDK and CCDC146 Abs immunodecorate the same cellular**
1139 **components.**

1140 HEK-293T cells were transfected with a plasmid containing the sequence of DDK-CCDC146 (human).
1141 After cell fixation, cells were double immunolabeled for CCDC146 (red) and DDK (green) with the
1142 corresponding Abs. (A) Immunostaining of interphase and mitotic cells. Both antibodies stain the
1143 centrosome. (B) Same experiment with secondary Ab only. Scale bars as indicated.

1144 **Figure 4—Figure supplement 2. CCDC146 does not colocalize with the centriolar satellite marker**
1145 **PCM1.** (A) HEK-293T cells were double immunolabeled for PCM1 (cyan) and CCDC146 (magenta). (A1-
1146 A4) Images on the right show the enlargement of the dotted squares in the left image. PCM1 surrounds
1147 the CCDC146 signal, but no colocalization is observed, suggesting that CCDC146 is not a centriolar
1148 satellite protein. DNA was stained with Hoechst (blue). Scale bars on zoomed images represent 2 µm.

1149 **Figure 5—Figure supplement 1. CCDC146 shows a similar localization to the centrosome and to the**
1150 **midbody in primary HFF cells.** (A) Primary human foreskin fibroblast (HFF) cells were triple
1151 immunolabeled with anti-β-tubulin (green), anti-centrin (yellow, showing the centrioles) and anti-
1152 CCDC146 (magenta). (A1) The right-hand images show the enlargement of the dotted squares in the
1153 left-hand image. CCDC146 localized to and around the centrioles. (B) Staining of the centrosome area
1154 (B1) and (B2) shows co-localization of the CCDC146 staining with the midbody during cytokinesis. Scale
1155 bars of zoomed images 2 µm.

1156 **Figure 6—Figure supplement 1. Molecular strategy used to generate HA-tagged CCDC146 mice by**
1157 **CRISPR/Cas9**

1158 (A) Exon 2, the first coding sequence, was targeted by an RNA guide (5'- TAC TTT AGA ACT GTG AAA
1159 AAT GG -3'). (B) Using a single-stranded DNA (ssDNA) template, the HA sequence (5'-TAC CCA TAC GAT
1160 GTT CCA GAT TAC GCT-3') was inserted upstream of the PAM sequence.

1161 **Figure 7—Figure supplement 1. Staining by Anti-HA Abs of axonemal breaks induced by expansion.**
1162 Mouse epididymal spermatozoa observed with expansion microscopy. HA-CCDC146 sperm were
1163 immunolabeled with anti-β-tubulin (green) and anti-HA #3 (red) Abs. The right image shows the sperm
1164 with merged immunostaining. Expansion induced axonemal breaks associated with strong HA-
1165 CCDC146 staining (red). Scale bars correspond to 10 µm.

1166 **Figure 8—Figure supplement 1. Centrioles are identified by anti-POC5 Abs in expanded human**
1167 **ejaculated spermatozoa.** Human control sperm were co-stained, after expansion, with anti- α+β-
1168 tubulin (green) and anti-POC5 (magenta) Abs. (A) The centrosomal protein POC5 locates to centrioles

1169 at the base of the axoneme. (B) Apart the centriole staining, a scattered staining was also observed in
1170 the midpiece around the axoneme (white arrows heads). Scale bars 5 µm.

1171 **Figure 10—Figure supplement 1. Sperm sarkosyl treatment corroborates the presence of CCDC146**
1172 **along the mouse flagellum.** HA-CCDC146 sperm (A1-A2) and epididymal WT (A3-A4) not treated or
1173 treated (5 min, 0.2% sarkosyl), were immunostained with anti-HA Ab (red) and counterstained with
1174 Hoechst (blue). (A1) Without treatment, a faint HA-CCDC146 signal was observed along the HA-
1175 CCDC146 principal piece. The strong staining in the midpiece is not specific (see panel B). (A2) After
1176 treatment with sarkosyl, the HA-CCDC146 signal along the sperm principal piece was enhanced (white
1177 arrows), whereas the signal in the midpiece decreased. (A3) WT untreated (NT) sperm exhibited almost
1178 no HA-CCDC146 signal in the principal piece. The midpiece is stained but it is likely not specific (see
1179 panel B). (A4) The HA signal is not enhanced in WT principal piece by sarkosyl treatment, suggesting
1180 that the enhanced signal observed with sarkosyl on HA-CCDC146 sperm is specific. Scale bars 10 µm.
1181 (B) HA-CCDC146 sperm were only immunolabeled with secondary antibodies used to reveal HA
1182 staining. Strong staining is observed on the midpiece, confirming its non-specific nature. Scale bars
1183 20 µm.

1184 **Figure 12—Figure supplement 1. Ultrastructure of WT sperm showing the head to tail coupling**
1185 **apparatus (HTCA) in elongating spermatids.** The adjunct is connected to the proximal centriole (PC).
1186 The axoneme (Ax) is elongated from the distal centriole (DC). Scale bars 0.5 µm.

1187 **Figure 12—Figure supplement 2. Lack of CCDC146 causes centriole duplication and mislocalization**
1188 **in *Ccdc146* KO spermatids.** Ultrastructural analysis of centrioles in adult mouse WT (A, B) and *Ccdc146*
1189 KO (C-H) testis sections. (A) In WT spermatids, the axoneme is attached to the base of the compacting
1190 nucleus (Nu) through the basal plate (BP) and the capitulum (Ca), and the distal centriole (DC) is
1191 embedded in the segmented column (SC). These sperm-specific cytoskeletal structures make up the
1192 head-to-tail coupling apparatus (HTCA). (B) In WT elongated spermatids, the different components of
1193 the axonemal structures (Ax) and outer dense fibers (ODF) were visible downstream the distal
1194 centriole. (C) In *Ccdc146* KO elongating spermatids, the overall structure of the HTCA was conserved,
1195 with the presence of the centrioles and the accessory cytoskeletal structures. However, the HTCAs
1196 were often duplicated (C, E, F) and separated from their usual nuclear attachment site (C-F, H), and
1197 sometimes misplaced far away from the nucleus (F), the red arrow in F indicating the misplaced
1198 centrioles at the end of the manchette. The axoneme is missing (C-F). In elongated spermatids with
1199 condensed nucleus, malformed and detached centrioles with poorly-assembled or missing flagella
1200 compared to the WT (B) can be seen. Manchette (Ma), Adjunct (Ad), proximal centriole (PC). Scale bars
1201 1µm.

1202 **Figure 13—Figure supplement 1. The manchette of elongating spermatids from *Ccdc146* KO male is**
1203 **longer than those from WT males.** (A) Comparison of the length of the manchette of elongating
1204 spermatids measured in cross-sections of seminiferous tubules at stage I for WT and stages I-III for
1205 *Ccdc146* KO spermatids. Statistical significance between WT and *Ccdc146*-KO spermatids was assessed
1206 by Mann-Whitney test, p value as indicated. (B) Examples of very long manchettes (white arrow heads)
1207 in *Ccdc146* KO cross-sections of seminiferous tubules at stage I-III. WT cross-section is presented Figure
1208 13D1. Scale bars as indicated.

1209 **Figure 15—Figure supplement 1. Cross-sections of the midpiece, principal piece and tail piece of WT**
1210 **elongating spermatids showing the ultrastructure of the different pieces.** In the midpiece cross
1211 section, the axoneme is surrounded by 9 outer dense fibers (ODF) and an external layer of
1212 mitochondria (Mi). In the principal piece, the ODF are surrounded by the fibrous sheet (FS). Scale bar
1213 1 µm.

1214

1215 **Figure Supplementary 1. Amino-acid conservation of CCDC146 orthologs from man to *X. tropicalis*.**
1216 The amino acids altered and missing from the presence of the variant p.Arg704serfsTer7 are
1217 highlighted in yellow.

1218

1219 ## References

1220 1. Boivin, J., et al., *International estimates of infertility prevalence and treatment-seeking:*
1221 *potential need and demand for infertility medical care.* Hum.Reprod., 2007. **22**(6): p. 1506-
1222 1512.
1223 2. Uhlén, M., et al., *Transcriptomics resources of human tissues and organs.* Mol Syst Biol, 2016.
1224 **12**(4): p. 862.
1225 3. Houston, B.J., et al., *A systematic review of the validated monogenic causes of human male*
1226 *infertility: 2020 update and a discussion of emerging gene-disease relationships.* Hum Reprod
1227 Update, 2021. **28**(1): p. 15-29.
1228 4. Beurois, J., et al., *Genetics of teratozoospermia: Back to the head.* Best Pract Res Clin
1229 Endocrinol Metab, 2020. **34**(6): p. 101473.
1230 5. Touré, A., et al., *The genetic architecture of morphological abnormalities of the sperm tail.* Hum
1231 Genet, 2021. **140**(1): p. 21-42.
1232 6. Wang, J., et al., *Clinical detection, diagnosis and treatment of morphological abnormalities of*
1233 *sperm flagella: A review of literature.* Front Genet, 2022. **13**: p. 1034951.
1234 7. Sironen, A., et al., *Sperm defects in primary ciliary dyskinesia and related causes of male*
1235 *infertility.* Cell Mol Life Sci, 2020. **77**(11): p. 2029-2048.
1236 8. Lores, P., et al., *Homozygous missense mutation L673P in adenylate kinase 7 (AK7) leads to*
1237 *primary male infertility and multiple morphological anomalies of the flagella but not to primary*
1238 *ciliary dyskinesia.* Hum Mol Genet, 2018.
1239 9. Coutton, C., et al., *Bi-allelic Mutations in ARMC2 Lead to Severe Astheno-Teratozoospermia*
1240 *Due to Sperm Flagellum Malformations in Humans and Mice.* Am J Hum Genet, 2019. **104**(2):
1241 p. 331-340.
1242 10. Shen, Q., et al., *Bi-allelic truncating variants in CFAP206 cause male infertility in human and*
1243 *mouse.* Hum Genet, 2021. **140**(9): p. 1367-1377.
1244 11. Cong, J., et al., *Homozygous mutations in CCDC34 cause male infertility with*
1245 *oligoasthenoteratozoospermia in humans and mice.* J Med Genet, 2022. **59**(7): p. 710-718.
1246 12. Kherraf, Z.E., et al., *A Homozygous Ancestral SVA-Insertion-Mediated Deletion in WDR66*
1247 *Induces Multiple Morphological Abnormalities of the Sperm Flagellum and Male Infertility.* Am
1248 J Hum Genet, 2018. **103**(3): p. 400-412.
1249 13. Coutton, C., et al., *Mutations in CFAP43 and CFAP44 cause male infertility and flagellum defects*
1250 *in Trypanosoma and human.* Nat Commun, 2018. **9**(1): p. 686.
1251 14. Liu, C., et al., *Deleterious variants in X-linked CFAP47 induce asthenoteratozoospermia and*
1252 *primary male infertility.* Am J Hum Genet, 2021. **108**(2): p. 309-323.
1253 15. Liu, S., et al., *CFAP61 is required for sperm flagellum formation and male fertility in human and*
1254 *mouse.* Development, 2021. **148**(23).
1255 16. Li, W., et al., *Biallelic mutations in CFAP65 cause male infertility with multiple morphological*
1256 *abnormalities of the sperm flagella in humans and mice.* J Med Genet, 2020. **57**(2): p. 89-95.
1257 17. Dong, F.N., et al., *Absence of CFAP69 Causes Male Infertility due to Multiple Morphological*
1258 *Abnormalities of the Flagella in Human and Mouse.* Am J Hum Genet, 2018. **102**(4): p. 636-648.
1259 18. Beurois, J., et al., *CFAP70 mutations lead to male infertility due to severe astheno-*
1260 *teratozoospermia. A case report.* Hum Reprod, 2019. **34**(10): p. 2071-2079.
1261 19. Martinez, G., et al., *Biallelic variants in MAATS1 encoding CFAP91, a calmodulin-associated and*
1262 *spoke-associated complex protein, cause severe astheno-teratozoospermia and male*
1263 *infertility.* J Med Genet, 2020. **57**(10): p. 708-716.
1264 20. Ben Khelifa, M., et al., *Mutations in DNAH1, which encodes an inner arm heavy chain dynein,*
1265 *lead to male infertility from multiple morphological abnormalities of the sperm flagella.*
1266 American Journal of Human Genetics, 2014. **94**(1): p. 95-104.
1267 21. Liu, C., et al., *Bi-allelic DNAH8 Variants Lead to Multiple Morphological Abnormalities of the*
1268 *Sperm Flagella and Primary Male Infertility.* Am J Hum Genet, 2020. **107**(2): p. 330-341.

22. Martinez, G., et al., *Whole-exome sequencing identifies mutations in FSIP2 as a recurrent cause of multiple morphological abnormalities of the sperm flagella.* Hum Reprod, 2018. **33**(10): p. 1973-1984.
23. Lorès, P., et al., *A missense mutation in IFT74, encoding for an essential component for intraflagellar transport of Tubulin, causes asthenozoospermia and male infertility without clinical signs of Bardet-Biedl syndrome.* Hum Genet, 2021. **140**(7): p. 1031-1043.
24. Kherraf, Z.E., et al., *Whole exome sequencing of men with multiple morphological abnormalities of the sperm flagella reveals novel homozygous QRICH2 mutations.* Clin Genet, 2019. **96**(5): p. 394-401.
25. Liu, C., et al., *Homozygous mutations in SPEF2 induce multiple morphological abnormalities of the sperm flagella and male infertility.* J Med Genet, 2020. **57**(1): p. 31-37.
26. Liu, W., et al., *Bi-allelic Mutations in TTC21A Induce Asthenoteratospermia in Humans and Mice.* Am J Hum Genet, 2019. **104**(4): p. 738-748.
27. Lorès, P., et al., *Mutations in TTC29, Encoding an Evolutionarily Conserved Axonemal Protein, Result in Asthenozoospermia and Male Infertility.* Am J Hum Genet, 2019. **105**(6): p. 1148-1167.
28. Firat-Karalar, E.N., et al., *Proteomic analysis of mammalian sperm cells identifies new components of the centrosome.* J Cell Sci, 2014. **127**(Pt 19): p. 4128-4133.
29. Almeida, F., et al., *The Human Centrosomal Protein CCDC146 Binds Chlamydia trachomatis Inclusion Membrane Protein CT288 and Is Recruited to the Periphery of the Chlamydia-Containing Vacuole.* Front Cell Infect Microbiol, 2018. **8**(article 254).
30. Blanco-Ameijeiras, J., P. Lozano-Fernández, and E. Martí, *Centrosome maturation - in tune with the cell cycle.* J Cell Sci, 2022. **135**(2/jcs.259395).
31. Wu, B., et al., *The coupling apparatus of the sperm head and tail†.* Biol Reprod, 2020. **102**(5): p. 988-998.
32. Fishman, E.L., et al., *A novel atypical sperm centriole is functional during human fertilization.* Nat Commun, 2018. **9**(1): p. 2210.
33. Manandhar, G., et al., *Centrosome reduction during mouse spermiogenesis.* Dev Biol, 1998. **203**(2): p. 424-434.
34. Sha, Y.W., et al., *A homozygous CEP135 mutation is associated with multiple morphological abnormalities of the sperm flagella (MMAF).* Gene, 2017. **633**: p. 48-53.
35. Zhang, X., et al., *CEP128 is involved in spermatogenesis in humans and mice.* Nat Commun, 2022. **13**(1): p. 1395.
36. Lv, M., et al., *Homozygous mutations in DZIP1 can induce asthenoteratospermia with severe MMAF.* J Med Genet, 2020. **57**(7): p. 445-453.
37. Sha, Y., et al., *Biallelic mutations of CFAP58 are associated with multiple morphological abnormalities of the sperm flagella.* Clin Genet, 2021. **99**(3): p. 443-448.
38. Zhu, Z.J., et al., *Novel mutation in ODF2 causes multiple morphological abnormalities of the sperm flagella in an infertile male.* Asian J Androl, 2022. **24**(5): p. 463-472.
39. Nakagawa, Y., et al., *Outer dense fiber 2 is a widespread centrosome scaffold component preferentially associated with mother centrioles: its identification from isolated centrosomes.* Mol Biol Cell, 2001. **12**(6): p. 1687-1697.
40. Hall, E.A., et al., *Acute versus chronic loss of mammalian Azi1/Cep131 results in distinct ciliary phenotypes.* PLoS Genet, 2013. **9**(12): p. e1003928.
41. Pasek, R.C., et al., *Coiled-coil domain containing 42 (Ccdc42) is necessary for proper sperm development and male fertility in the mouse.* Dev Biol, 2016. **412**(2): p. 208-18.
42. Kherraf, Z.E., et al., *Whole-exome sequencing improves the diagnosis and care of men with non-obstructive azoospermia.* Am J Hum Genet, 2022. **109**(3): p. 508-517.
43. Yauy, K., et al., *MoBiDiC Prioritization Algorithm, a Free, Accessible, and Efficient Pipeline for Single-Nucleotide Variant Annotation and Prioritization for Next-Generation Sequencing Routine Molecular Diagnosis.* J Mol Diagn, 2018. **20**(4): p. 465-473.

1319 44. Odabasi, E., U. Batman, and E.N. Firat-Karalar, *Unraveling the mysteries of centriolar satellites:*
1320 *time to rewrite the textbooks about the centrosome/cilium complex.* Mol Biol Cell, 2020. **31**(9):
1321 p. 866-872.
1322 45. Zindy, F., et al., *Control of spermatogenesis in mice by the cyclin D-dependent kinase inhibitors*
1323 *p18(Ink4c) and p19(Ink4d).* Mol Cell Biol, 2001. **21**(9): p. 3244-55.
1324 46. Gambarotto, D., et al., *Imaging cellular ultrastructures using expansion microscopy (U-ExM).*
1325 Nat Methods, 2019. **16**(1): p. 71-74.
1326 47. Yanagisawa, H.A., et al., *FAP20 is an inner junction protein of doublet microtubules essential*
1327 *for both the planar asymmetrical waveform and stability of flagella in Chlamydomonas.* Mol
1328 Biol Cell, 2014. **25**(9): p. 1472-83.
1329 48. Witman, G.B., et al., *Chlamydomonas flagella. I. Isolation and electrophoretic analysis of*
1330 *microtubules, matrix, membranes, and mastigonemes.* J Cell Biol, 1972. **54**(3): p. 507-39.
1331 49. Linck, R.W., *Flagellar doublet microtubules: fractionation of minor components and alpha-*
1332 *tubulin from specific regions of the A-tubule.* J Cell Sci, 1976. **20**(2): p. 405-39.
1333 50. Kirima, J. and K. Oiwa, *Flagellar-associated Protein FAP85 Is a Microtubule Inner Protein That*
1334 *Stabilizes Microtubules.* Cell Struct Funct, 2018. **43**(1): p. 1-14.
1335 51. Simerly, C., et al., *Post-Testicular Sperm Maturation: Centriole Pairs, Found in Upper*
1336 *Epididymis, are Destroyed Prior to Sperm's Release at Ejaculation.* Sci Rep, 2016. **6**: p. 31816.
1337 52. Kierszenbaum, A.L., et al., *The acroplaxome is the docking site of Golgi-derived myosin*
1338 *Va/Rab27a/b- containing proacrosomal vesicles in wild-type and Hrb mutant mouse*
1339 *spermatids.* Biol.Reprod., 2004. **70**(5): p. 1400-1410.
1340 53. Martinez, G., et al., *Oligogenic heterozygous inheritance of sperm abnormalities in mouse.*
1341 Elife, 2022. **11**.
1342 54. Collins, S.A., W.T. Walker, and J.S. Lucas, *Genetic Testing in the Diagnosis of Primary Ciliary*
1343 *Dyskinesia: State-of-the-Art and Future Perspectives.* J Clin Med, 2014. **3**(2): p. 491-503.
1344 55. Shoemark, A., L. Ozerovitch, and R. Wilson, *Aetiology in adult patients with bronchiectasis.*
1345 Respir Med, 2007. **101**(6): p. 1163-70.
1346 56. Amargant, F., et al., *The human sperm basal body is a complex centrosome important for*
1347 *embryo preimplantation development.* Mol Hum Reprod, 2021. **27**(11:gaab062).
1348 57. Li, Z.Z., et al., *The novel testicular enrichment protein Cfap58 is required for Notch-associated*
1349 *ciliogenesis.* Biosci Rep, 2020. **40**(1).
1350 58. Cuveillier, C., et al., *Beyond Neuronal Microtubule Stabilization: MAP6 and CRMPS, Two*
1351 *Converging Stories.* Front Mol Neurosci, 2021. **14**: p. 665693.
1352 59. Ma, M., et al., *Structure of the Decorated Ciliary Doublet Microtubule.* Cell, 2019. **179**(4): p.
1353 909-922.e12.
1354 60. Jardin, I., et al., *SARAF and EFHB Modulate Store-Operated Ca(2+) Entry and Are Required for*
1355 *Cell Proliferation, Migration and Viability in Breast Cancer Cells.* Cancers (Basel), 2021. **13**(16).
1356 61. Segal, R.A., et al., *Mutant strains of Chlamydomonas reinhardtii that move backwards only.* J
1357 Cell Biol, 1984. **98**(6): p. 2026-34.
1358 62. Tam, L.W. and P.A. Lefebvre, *The Chlamydomonas MBO2 locus encodes a conserved coiled-coil*
1359 *protein important for flagellar waveform conversion.* Cell Motil Cytoskeleton, 2002. **51**(4): p.
1360 197-212.
1361 63. Shi, Z., et al., *Potential Novel Modules and Hub Genes as Prognostic Candidates of Thyroid*
1362 *Cancer by Weighted Gene Co-Expression Network Analysis.* Int J Gen Med, 2021. **14**: p. 9433-
1363 9444.
1364 64. Kasak, L., et al., *Bi-allelic Recessive Loss-of-Function Variants in FANCM Cause Non-obstructive*
1365 *Azoospermia.* Am J Hum Genet, 2018. **103**(2): p. 200-212.
1366 65. Lehti, M.S. and A. Sironen, *Formation and function of the manchette and flagellum during*
1367 *spermatogenesis.* Reproduction, 2016. **151**(4): p. R43-54.
1368 66. O'Donnell, L., et al., *An essential role for katanin p80 and microtubule severing in male gamete*
1369 *production.* PLoS Genet, 2012. **8**(5): p. e1002698.

1370 67. Ho, U.Y., et al., *WDR62 is required for centriole duplication in spermatogenesis and manchette*
1371 *removal in spermiogenesis.* Commun Biol, 2021. **4**(1): p. 645.
1372 68. Zhu, F., et al., *Biallelic SUN5 Mutations Cause Autosomal-Recessive Acephalic Spermatozoa*
1373 *Syndrome.* Am J Hum Genet, 2016. **99**(4): p. 942-949.
1374 69. Yuan, S., et al., *Spata6 is required for normal assembly of the sperm connecting piece and tight*
1375 *head-tail conjunction.* Proc.Natl.Acad.Sci.U.S.A, 2015. **112**(5): p. E430-E439.
1376 70. Hoyer-Fender, S., *Development of the Connecting Piece in ODF1-Deficient Mouse Spermatids.*
1377 Int J Mol Sci, 2022. **23**(18:10280).
1378 71. Dunleavy, J.E.M., et al., *Katanin-like 2 (KATNAL2) functions in multiple aspects of haploid male*
1379 *germ cell development in the mouse.* PLoS Genet, 2017. **13**(11): p. e1007078.
1380 72. Giordano, T., et al., *Loss of the deglutamylase CCP5 perturbs multiple steps of spermatogenesis*
1381 *and leads to male infertility.* J Cell Sci, 2019. **132**(3).
1382 73. Tapia Contreras, C. and S. Hoyer-Fender, *CCDC42 Localizes to Manchette, HTCA and Tail and*
1383 *Interacts With ODF1 and ODF2 in the Formation of the Male Germ Cell Cytoskeleton.* Front Cell
1384 Dev Biol, 2019. **7**: p. 151.
1385 74. Wang, Y., et al., *Variability in the morphologic assessment of human sperm: use of the strict*
1386 *criteria recommended by the World Health Organization in 2010.* Fertil Steril, 2014. **101**(4): p.
1387 945-9.
1388 75. Schindelin, J., et al., *Fiji: an open-source platform for biological-image analysis.* Nat Methods,
1389 2012. **9**(7): p. 676-82.
1390 76. Mazo, G., *QuickFigures: A toolkit and ImageJ PlugIn to quickly transform microscope images*
1391 *into scientific figures.* PLoS One, 2021. **16**(11): p. e0240280.
1392 77. Berg, S., et al., *ilastik: interactive machine learning for (bio)image analysis.* Nat Methods, 2019.
1393 **16**(12): p. 1226-1232.
1394 78. Reynolds, E.S., *The use of lead citrate at high pH as an electron-opaque stain in electron*
1395 *microscopy.* J Cell Biol, 1963. **17**(1): p. 208-12.
1396 79. Pierre, V., et al., *Absence of Dpy19l2, a new inner nuclear membrane protein, causes*
1397 *globozoospermia in mice by preventing the anchoring of the acrosome to the nucleus.*
1398 Development, 2012. **139**(16): p. 2955-65.

1399

Figure 1

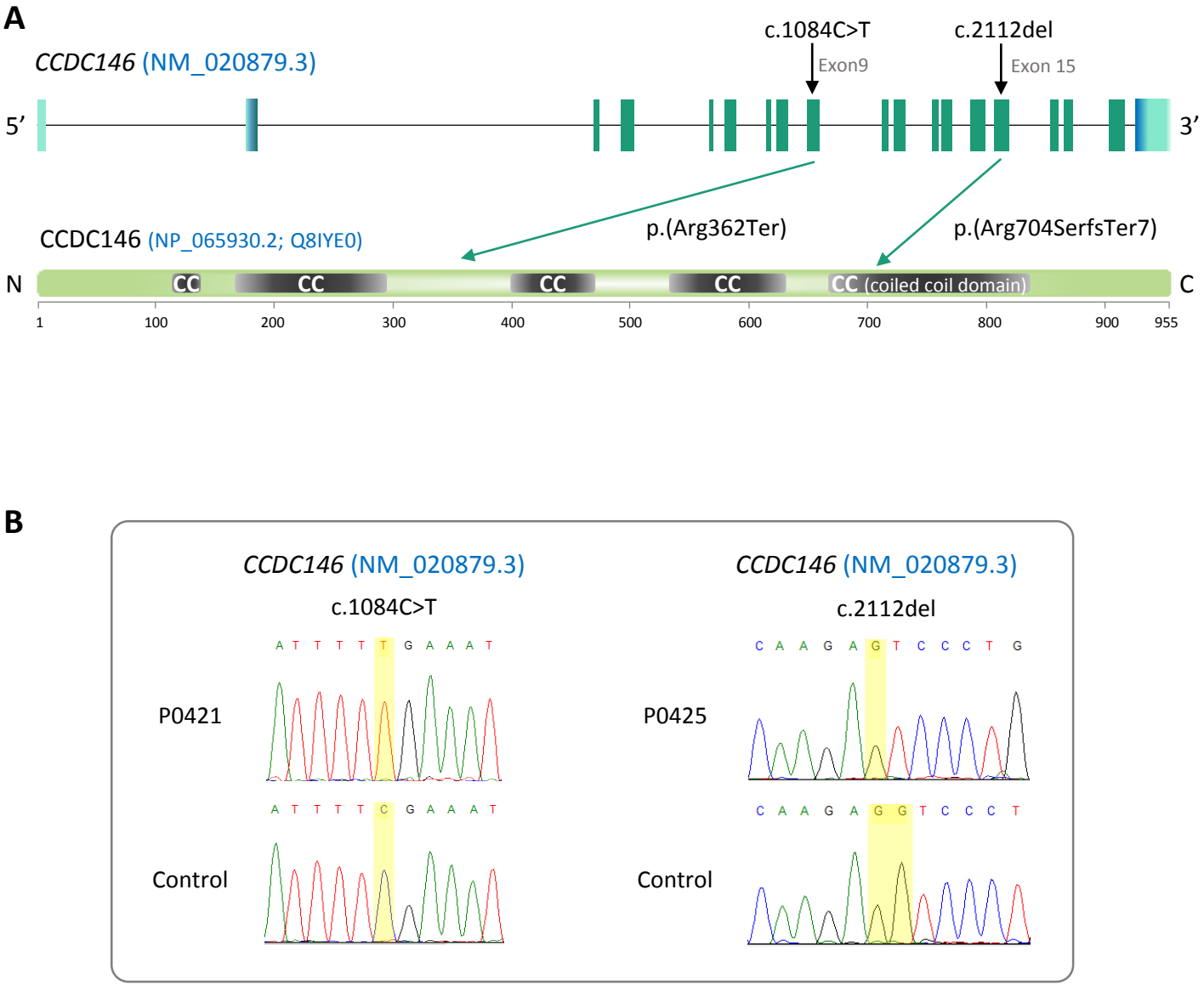
A
CCDC146 (NM_020879.3)
c.1084C>T
Exon9
c.2112del
Exon 15
5'
3'
CCDC146 (NP_065930.2; Q8IYE0)
p.(Arg362Ter)
p.(Arg704SerfsTer7)
N
CC
CC
CC
CC
CC (coiled coil domain)
C
1
100
200
300
400
500
600
700
800
900
955
B
CCDC146 (NM_020879.3)
c.1084C>T
P0421
Control
CCDC146 (NM_020879.3)
c.2112del
P0425
Control

Figure 2

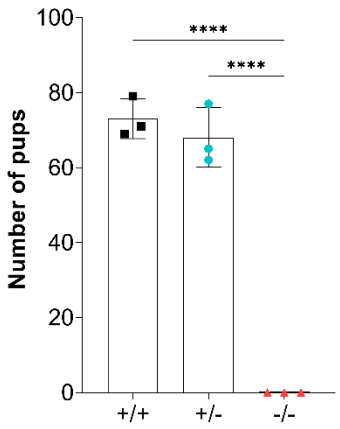
A
Number of pups
100
80
60
40
20
0
****
****
+/+
+/-
-/-

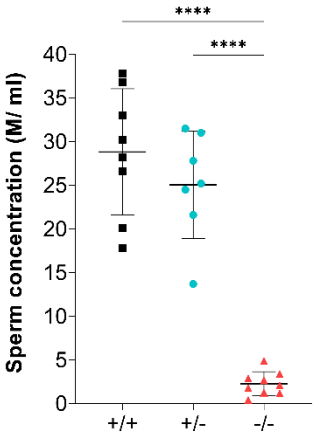
B
Sperm concentration (M/ ml)
40
35
30
25
20
15
10
5
0
****
****
+/+
+/-
-/-

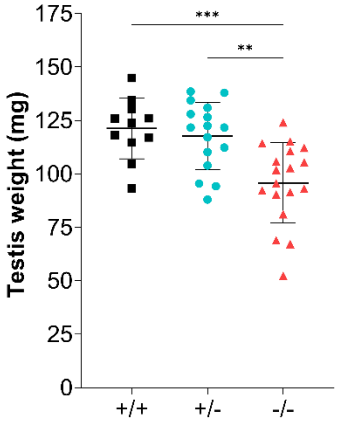
C
Testis weight (mg)
175
150
125
100
75
50
25
0
***
**
+/+
+/-
-/-

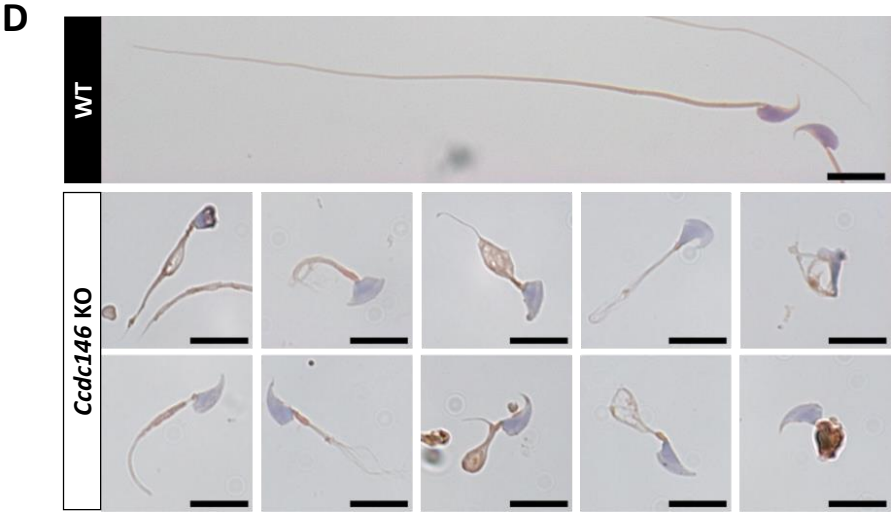
D
WT
Ccdc146 KO

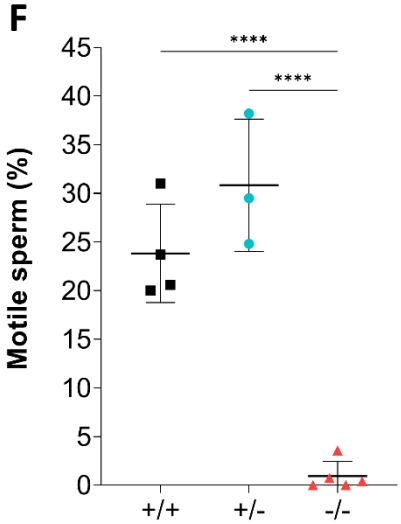
F
Motile sperm (%)
45
40
35
30
25
20
15
10
5
0
****
****
+/+
+/-
-/-

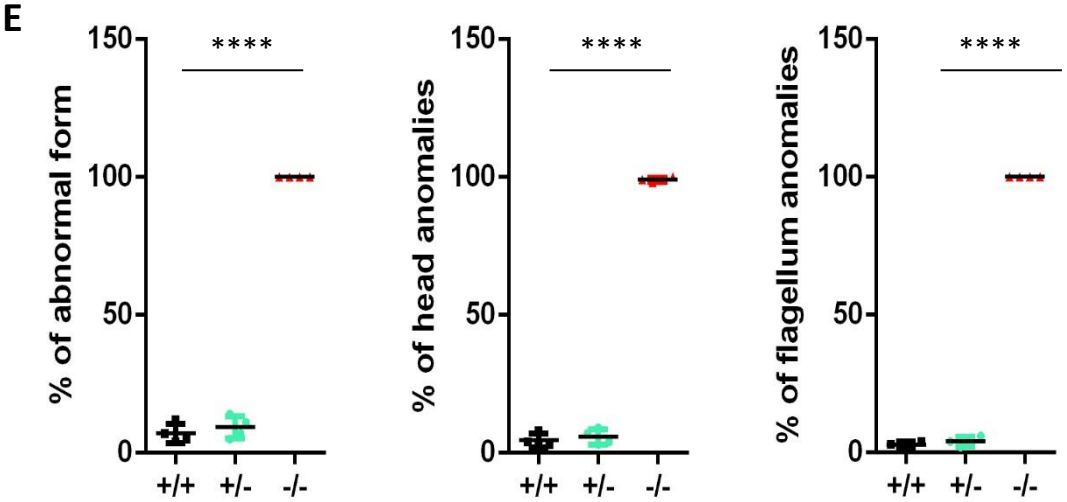
E
% of abnormal form
% of head anomalies
% of flagellum anomalies
150
100
50
0
****
+/+
+/-
-/-

Figure 3

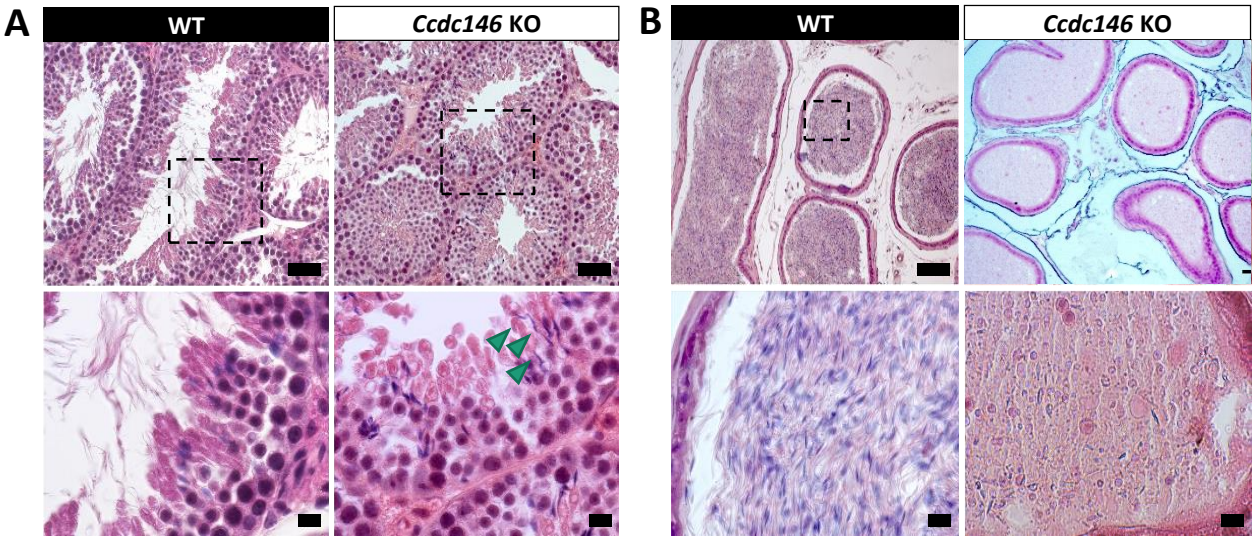

Figure 4

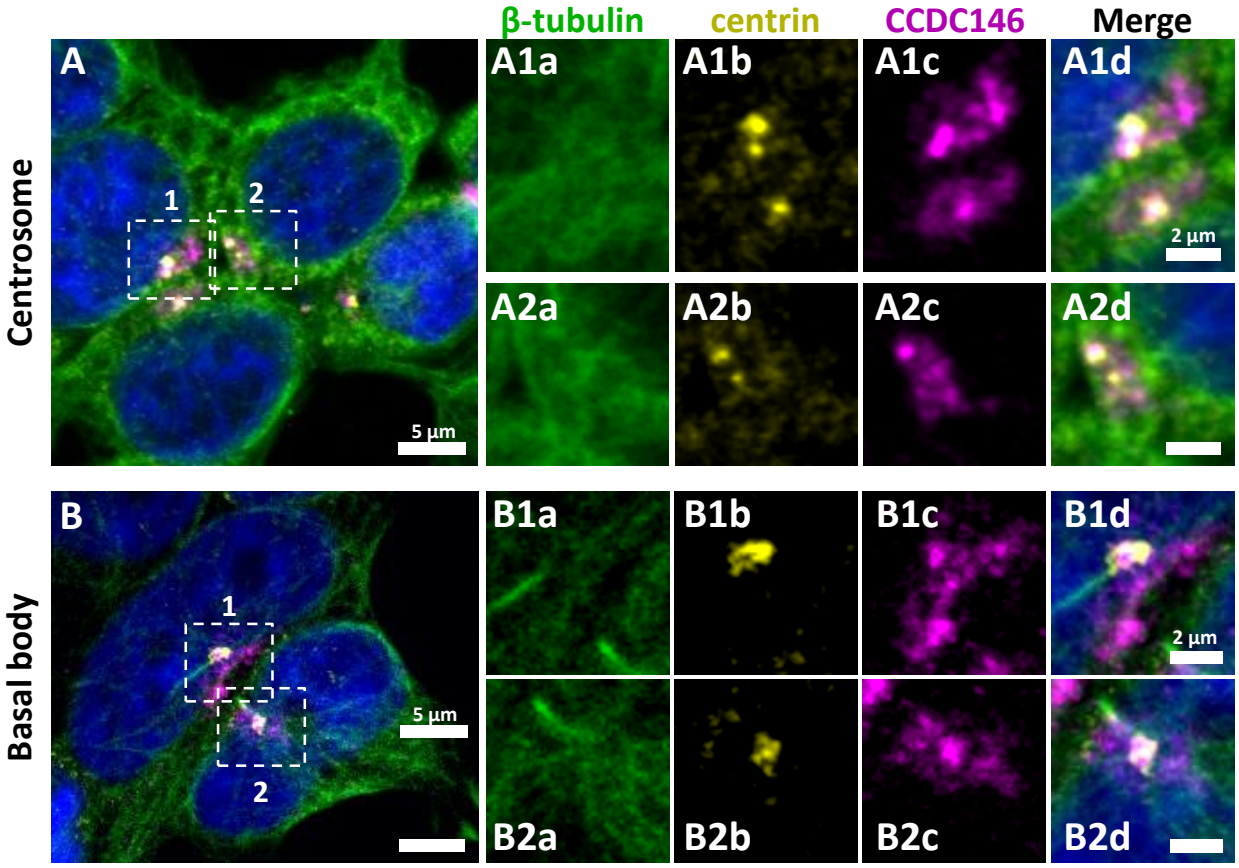
β-tubulin
centrin
CCDC146
Merge
Centrosome
Basal body
A
A1a
A1b
A1c
A1d
A2a
A2b
A2c
A2d
B
B1a
B1b
B1c
B1d
B2a
B2b
B2c
B2d
1
2
5 µm
2 µm

Figure 5

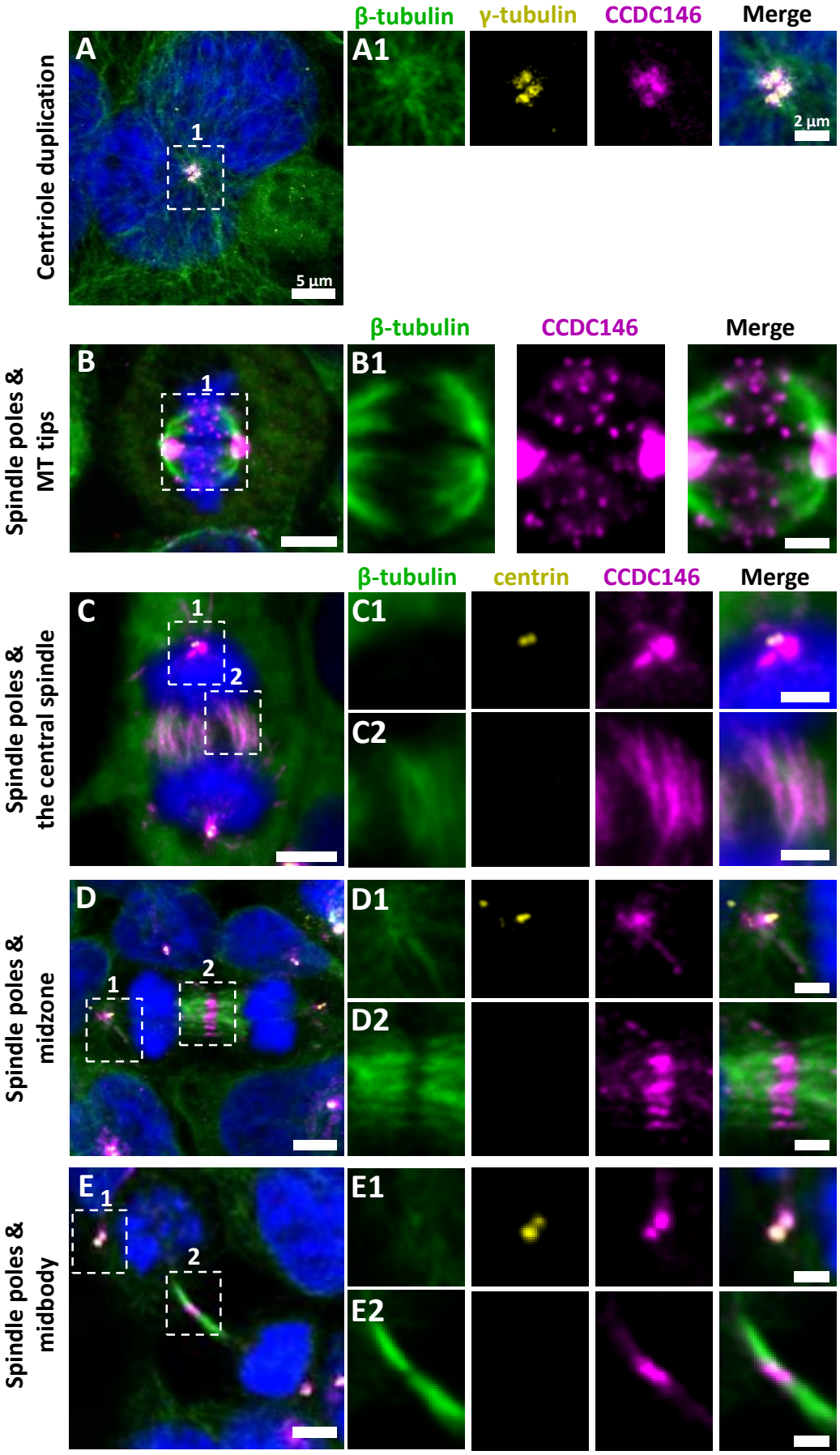
β-tubulin
γ-tubulin
CCDC146
Merge
Centriole duplication
A
A1
1
5 µm
2 µm
β-tubulin
CCDC146
Merge
Spindle poles & MT tips
B
B1
1
β-tubulin
centrin
CCDC146
Merge
Spindle poles & the central spindle
C
C1
C2
1
2
Spindle poles & midzone
D
D1
D2
1
2
Spindle poles & midbody
E
E1
E2
1
2

Figure 6

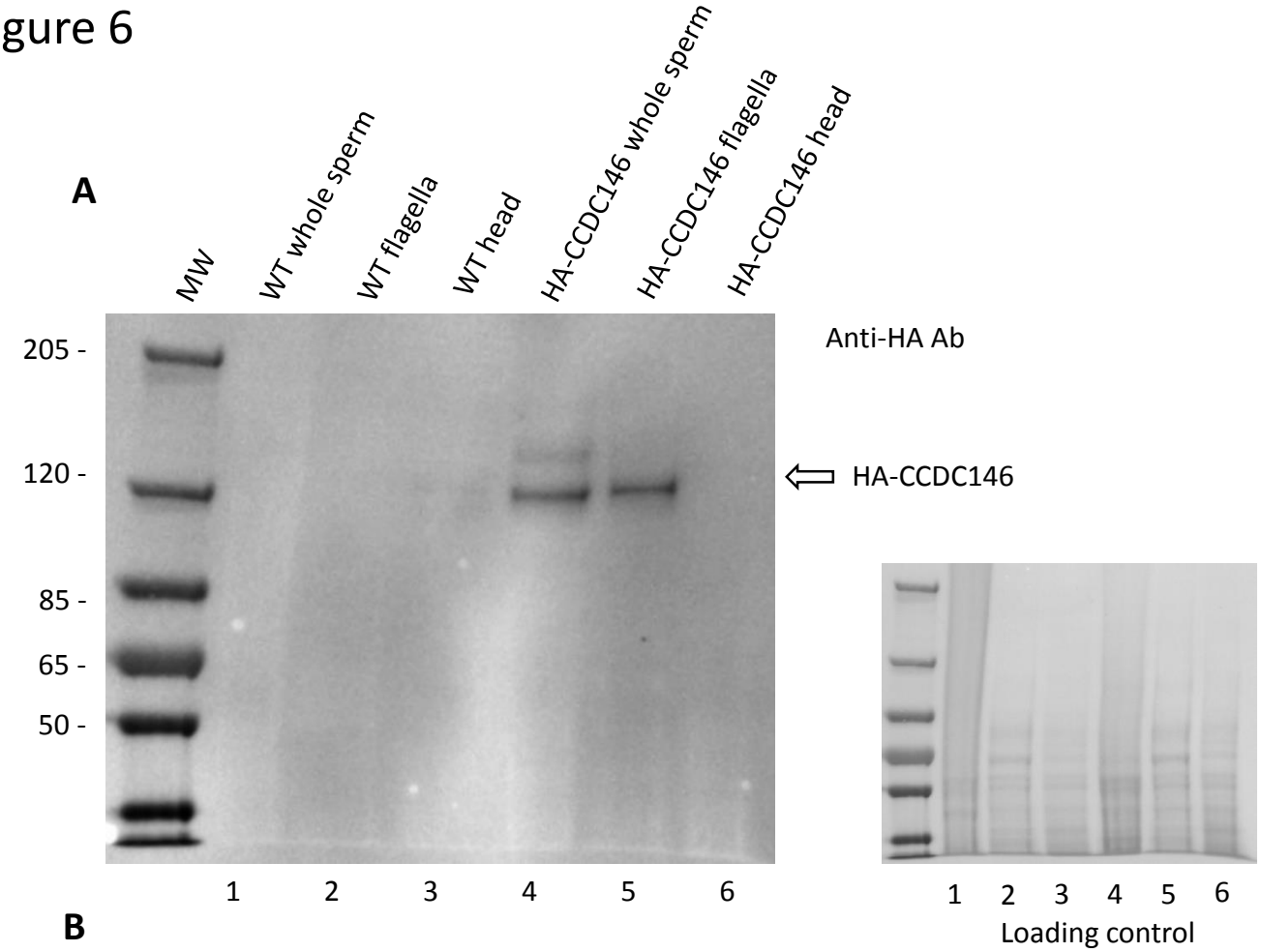
A
MW
WT whole sperm
WT flagella
WT head
HA-CCDC146 whole sperm
HA-CCDC146 flagella
HA-CCDC146 head
205 -
120 -
85 -
65 -
50 -
Anti-HA Ab
HA-CCDC146
1 2 3 4 5 6
1 2 3 4 5 6
Loading control

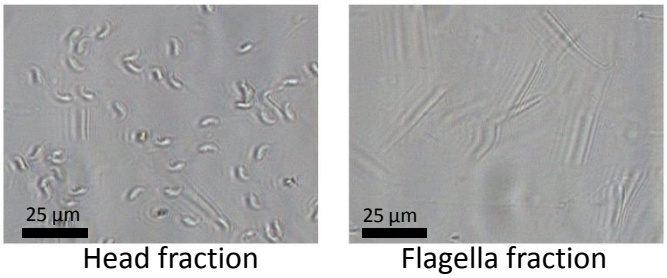
B
25 µm
25 µm
Head fraction
Flagella fraction

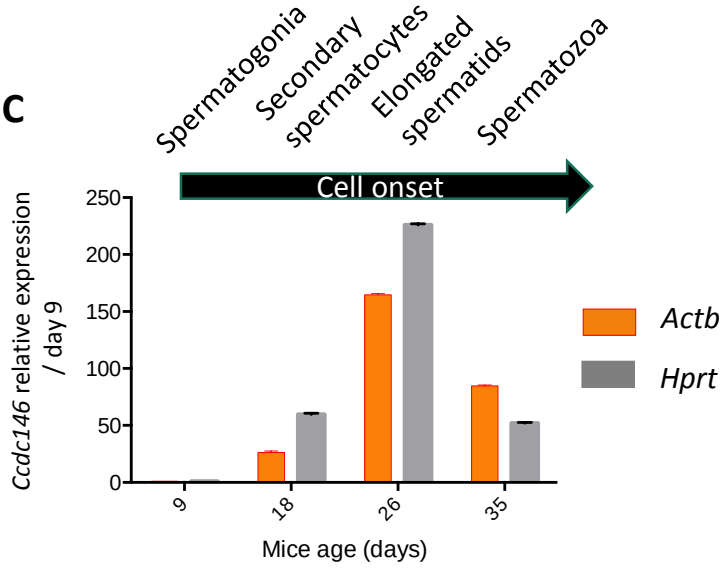
C
Spermatogonia
Secondary spermatocytes
Elongated spermatids
Spermatozoa
Cell onset
Ccdc146 relative expression / day 9
250
200
150
100
50
0
9
18
26
35
Mice age (days)
Actb
Hprt

Figure 7

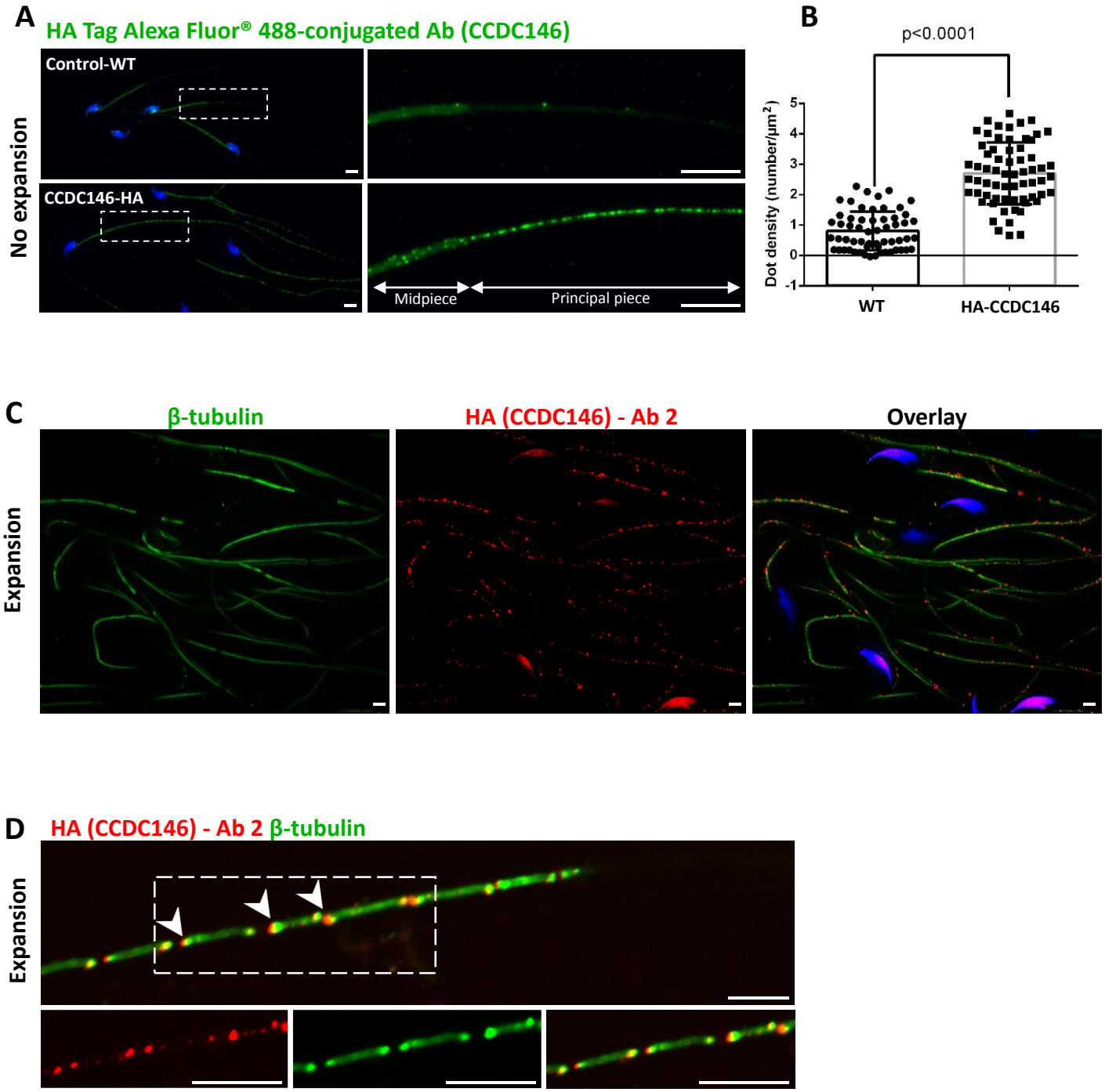
A
HA Tag Alexa Fluor® 488-conjugated Ab (CCDC146)
No expansion
Control-WT
CCDC146-HA
Midpiece
Principal piece
B
p<0.0001
Dot density (number/µm²)
5
4
3
2
1
0
-1
WT
HA-CCDC146
C
Expansion
β-tubulin
HA (CCDC146) - Ab 2
Overlay
D
HA (CCDC146) - Ab 2 β-tubulin
Expansion

Figure 8

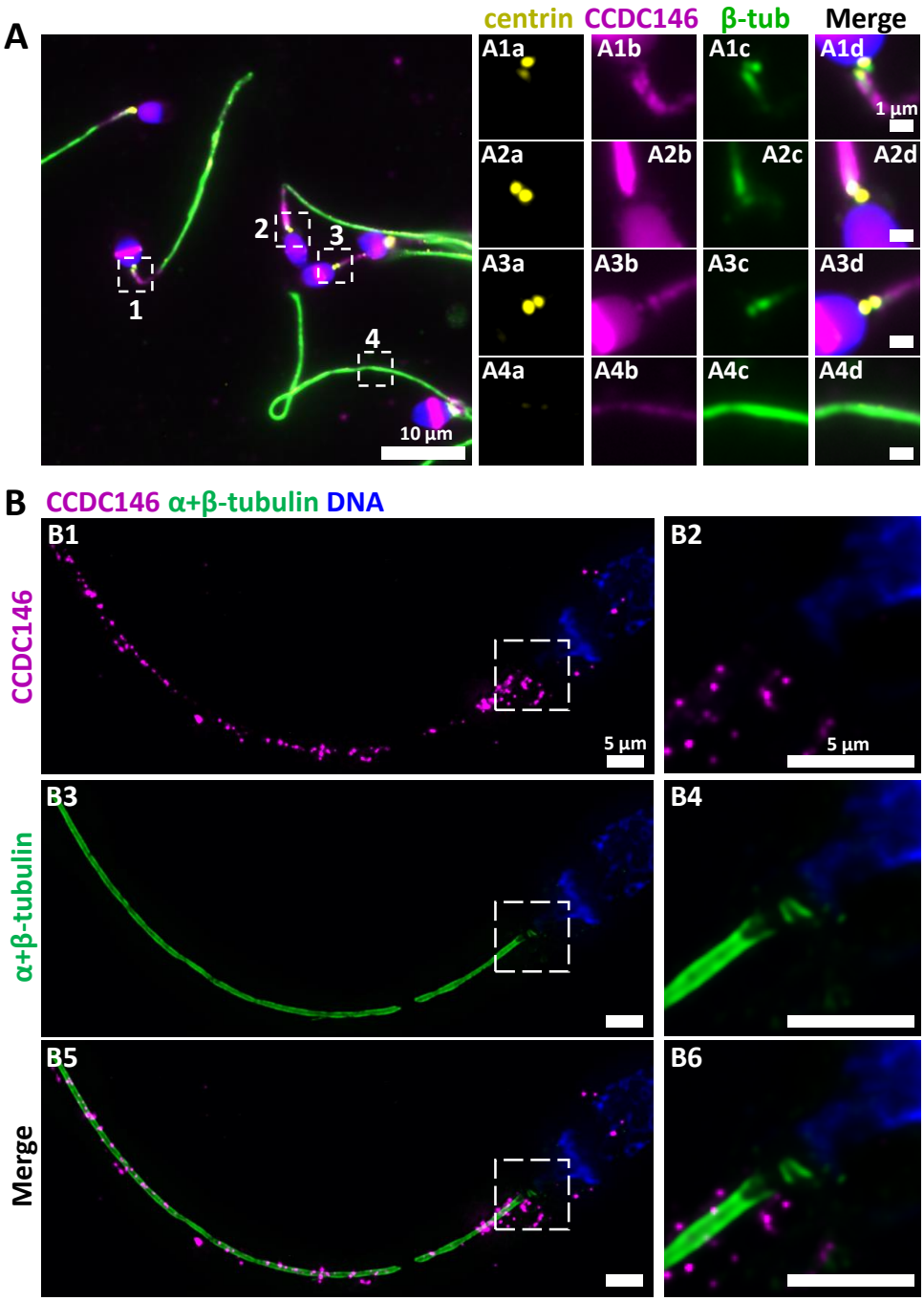
A
centrin
CCDC146
β-tub
Merge
A1a
A1b
A1c
A1d
1 µm
A2a
A2b
A2c
A2d
A3a
A3b
A3c
A3d
A4a
A4b
A4c
A4d
1
2
3
4
10 µm
B
CCDC146 α+β-tubulin DNA
CCDC146
α+β-tubulin
Merge
B1
B2
B3
B4
B5
B6
5 µm
5 µm

Figure 9

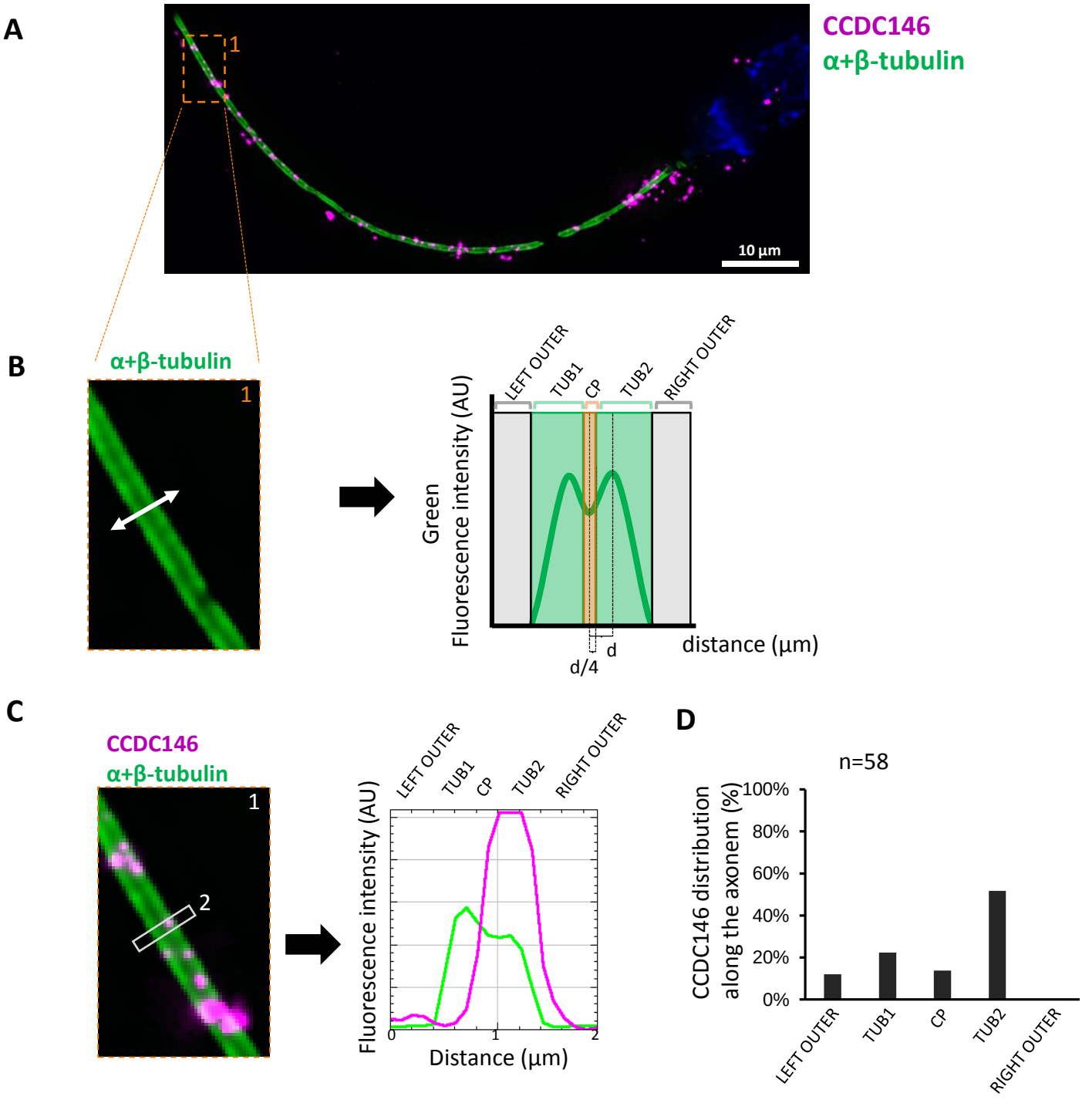

E HA (CCDC146) - Ab 2 β-tubulin

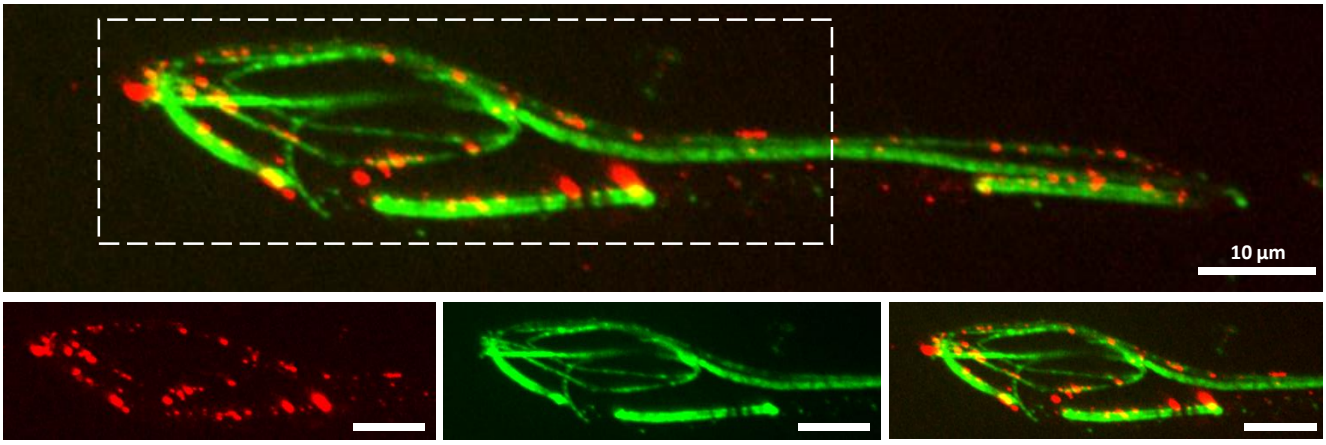

Figure 10

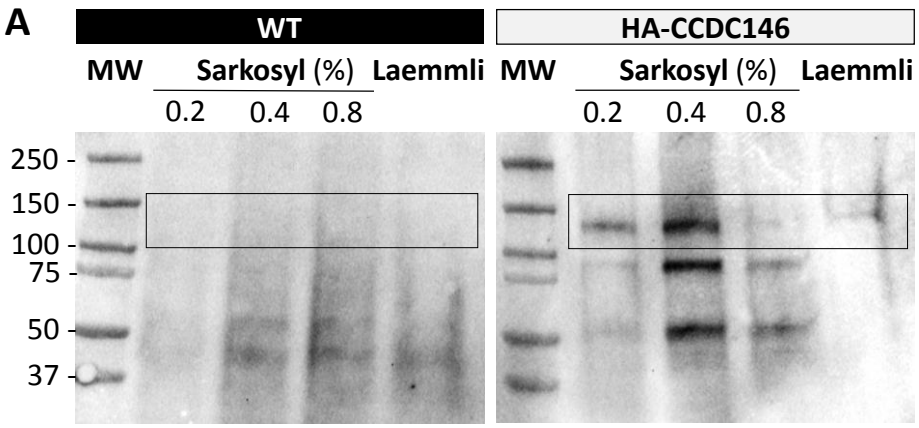
A
WT
HA-CCDC146
MW
Sarkosyl (%)
Laemmli
0.2
0.4
0.8
250
150
100
75
50
37

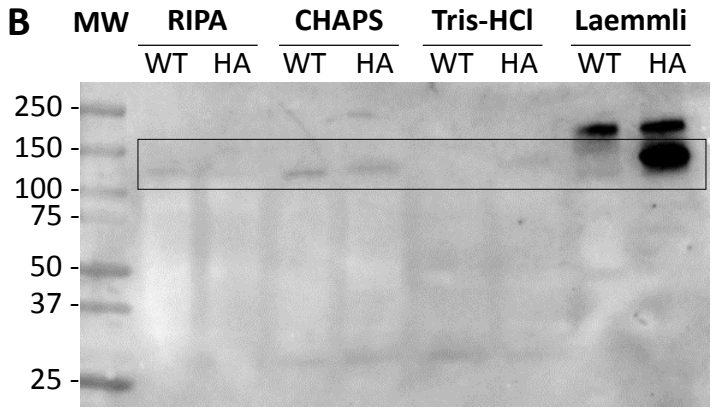
B
MW
RIPA
CHAPS
Tris-HCl
Laemmli
WT
HA
250
150
100
75
50
37
25

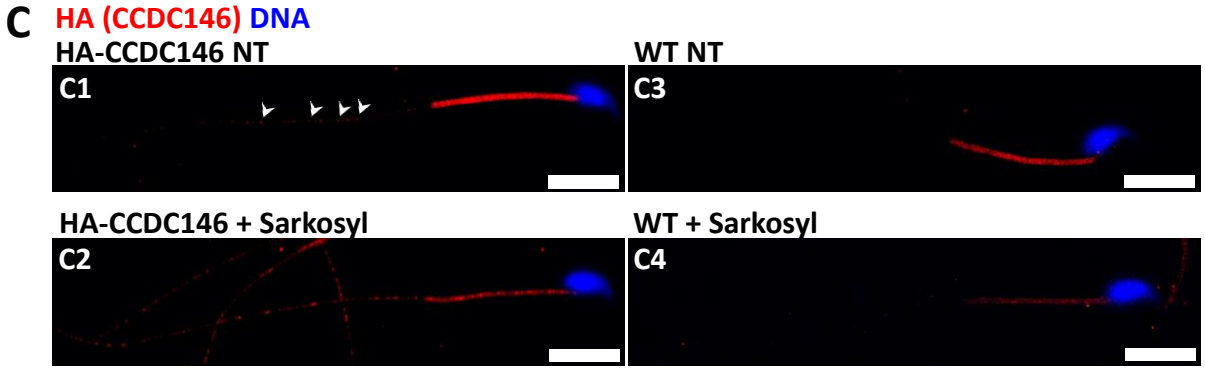
C
HA (CCDC146) DNA
HA-CCDC146 NT
WT NT
C1
C3
HA-CCDC146 + Sarkosyl
WT + Sarkosyl
C2
C4

Figure 11

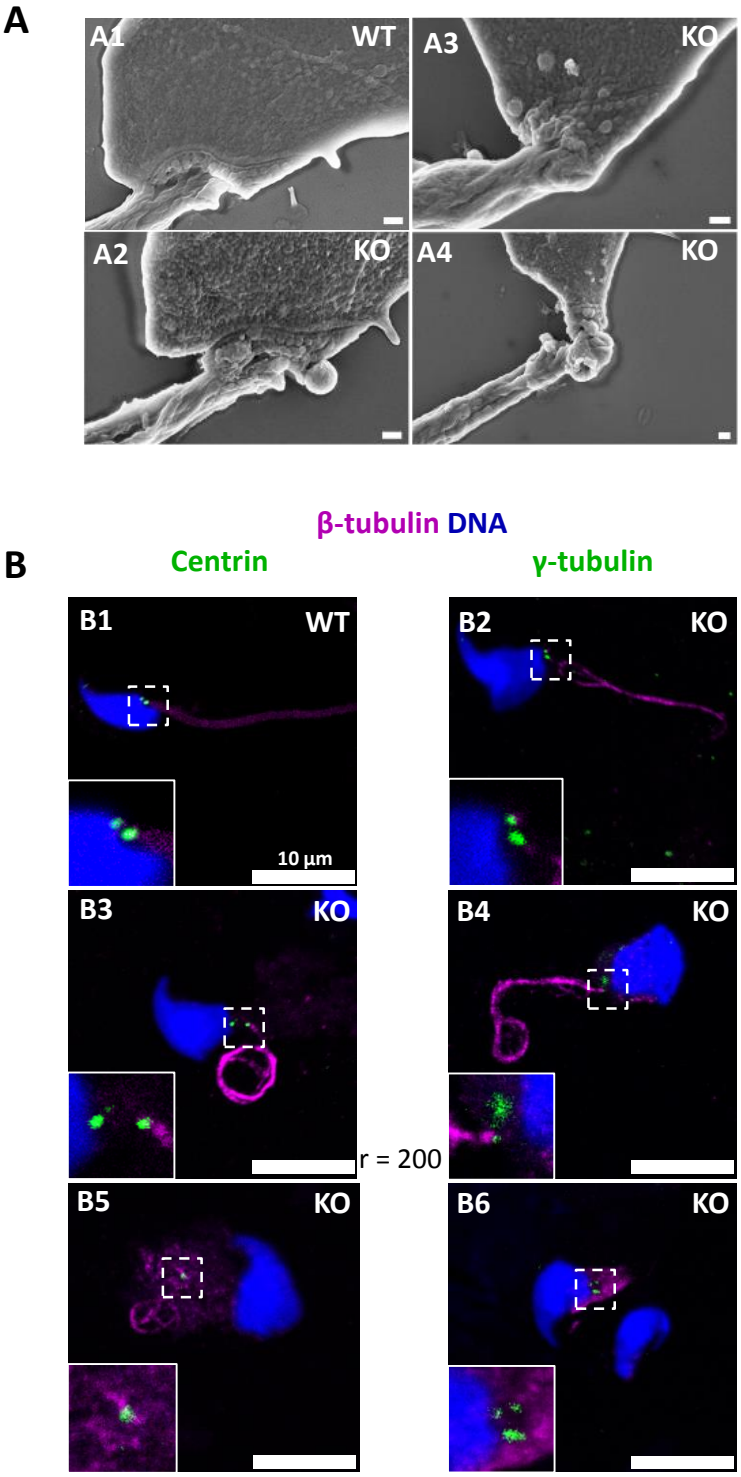
A
A1
WT
A3
KO
A2
KO
A4
KO
β-tubulin DNA
B
Centrin
γ-tubulin
B1
WT
B2
KO
10 µm
B3
KO
B4
KO
r = 200
B5
KO
B6
KO

Figure 12

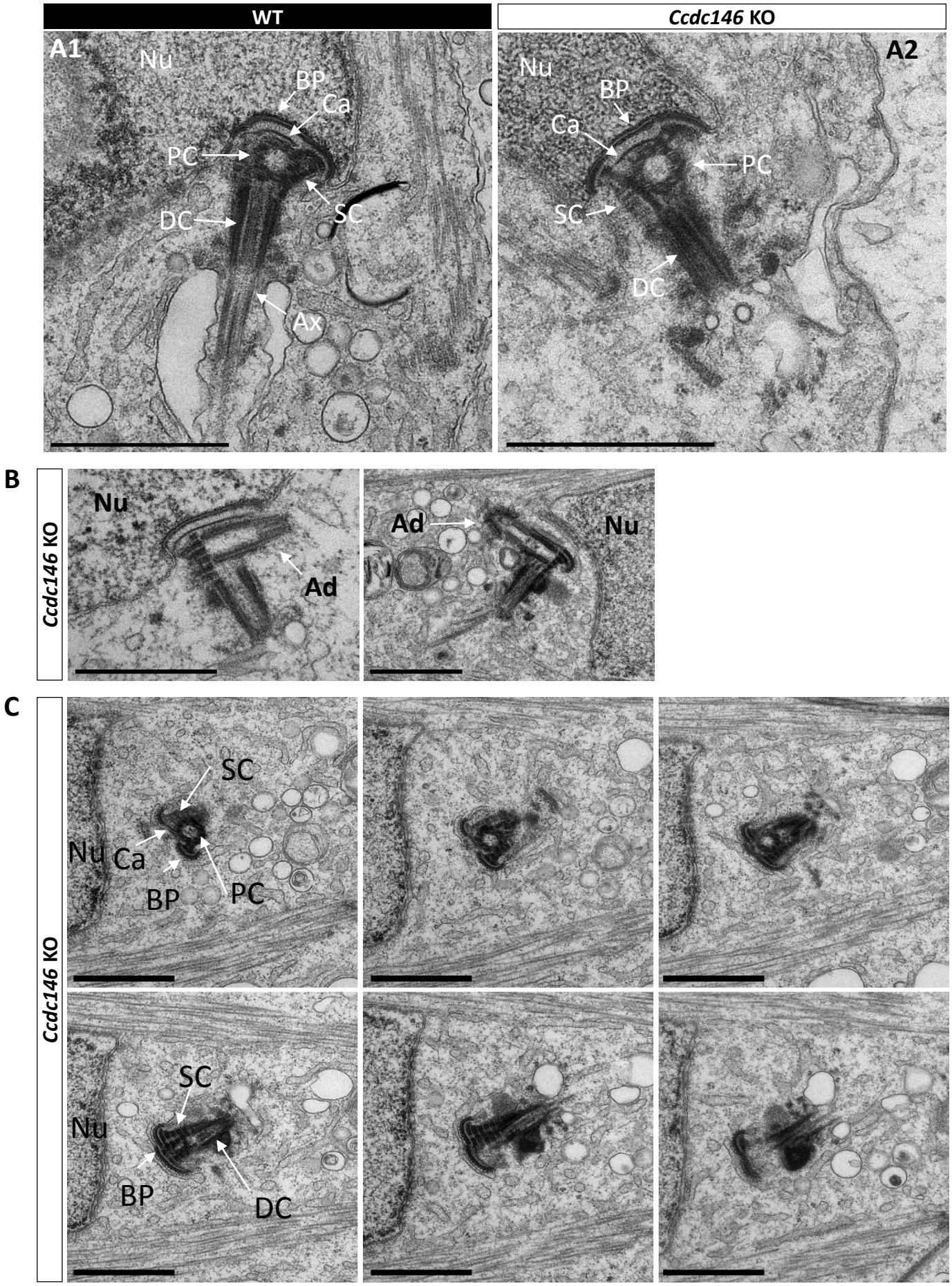
WT
Ccdc146 KO
A1
Nu
BP
Ca
PC
SC
DC
Ax
A2
Nu
BP
Ca
PC
SC
DC
B
Ccdc146 KO
Nu
Ad
Ad
Nu
C
Ccdc146 KO
SC
Nu
Ca
BP
PC
SC
Nu
BP
DC

Figure 13

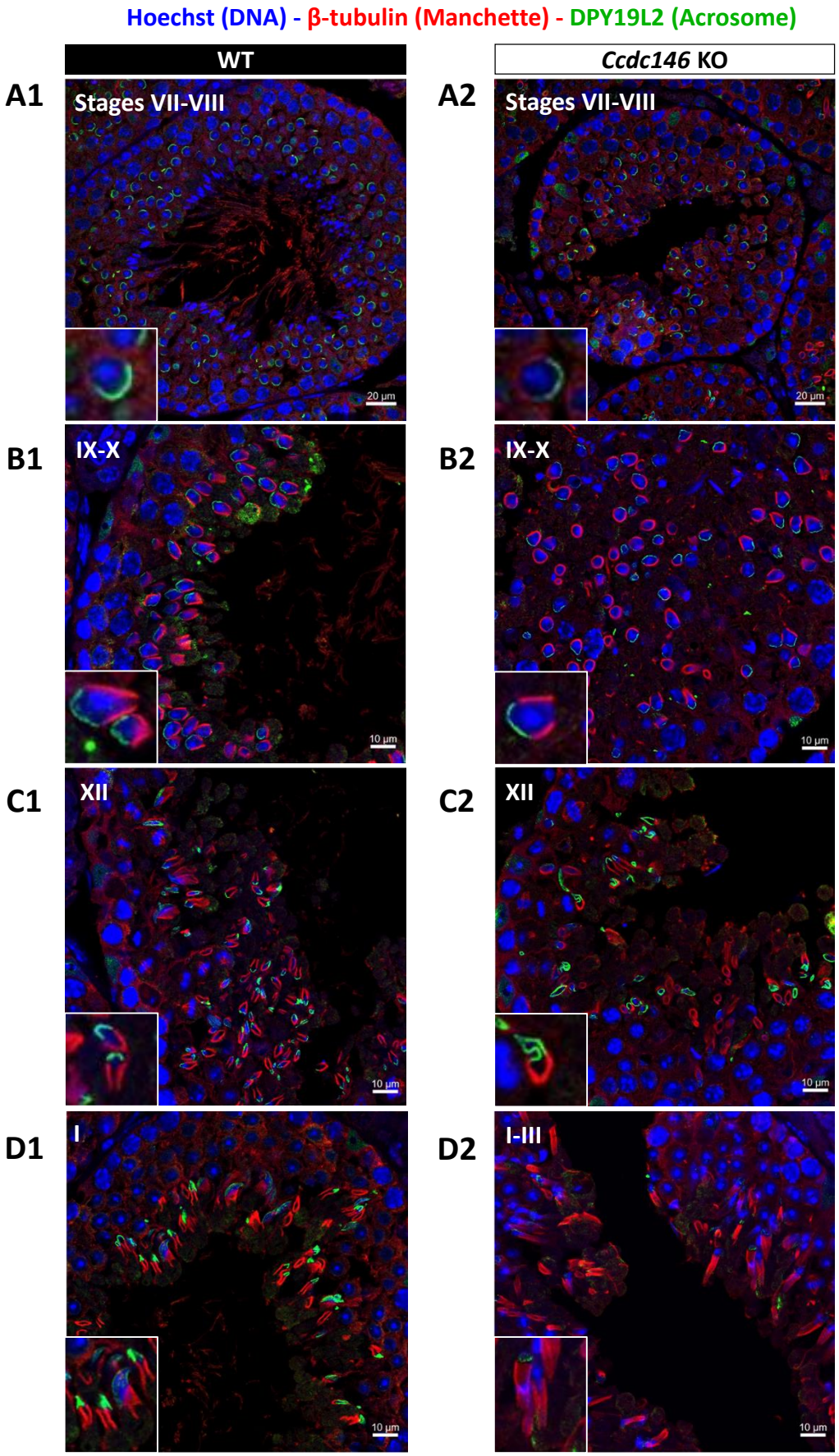
Hoechst (DNA) - β-tubulin (Manchette) - DPY19L2 (Acrosome)
WT
Ccdc146 KO
A1
Stages VII-VIII
20 µm
A2
Stages VII-VIII
20 µm
B1
IX-X
10 µm
B2
IX-X
10 µm
C1
XII
10 µm
C2
XII
10 µm
D1
I
10 µm
D2
I-III
10 µm

Figure 14

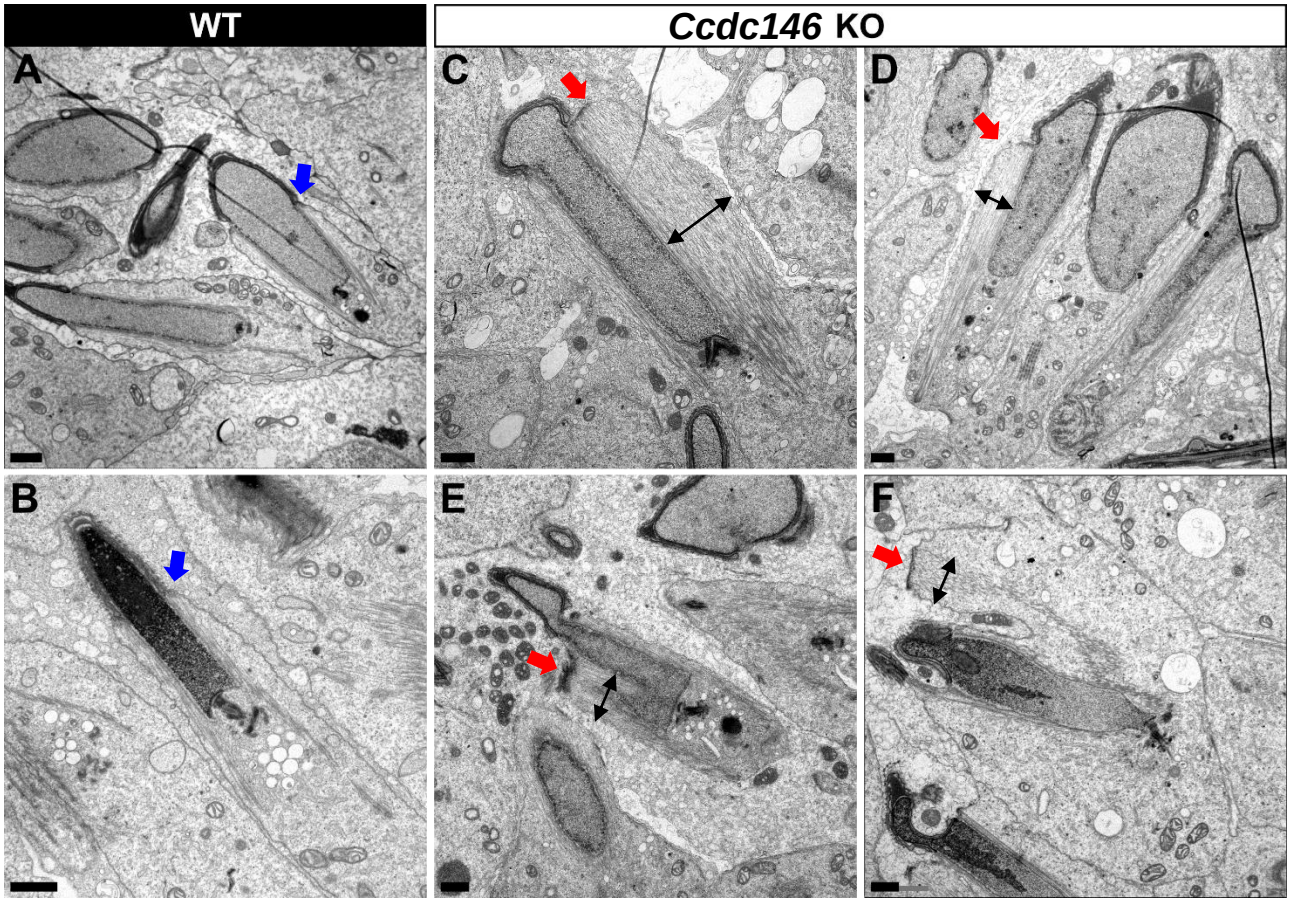

Figure 15

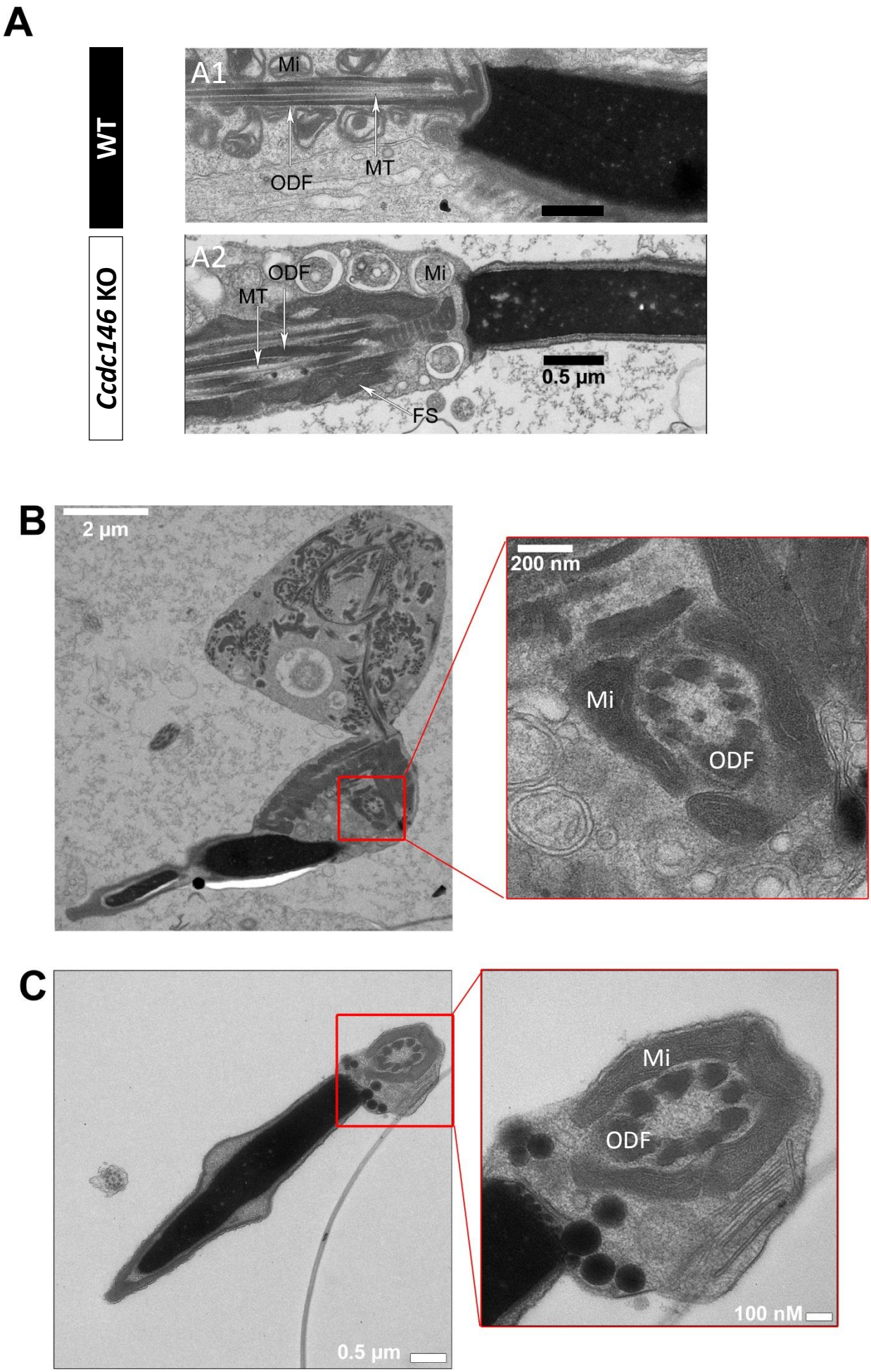
A
WT
A1
Mi
ODF
MT
Ccdc146 KO
A2
ODF
Mi
MT
0.5 µm
FS
B
2 µm
200 nm
Mi
ODF
C
Mi
ODF
0.5 µm
100 nM

Figure 16

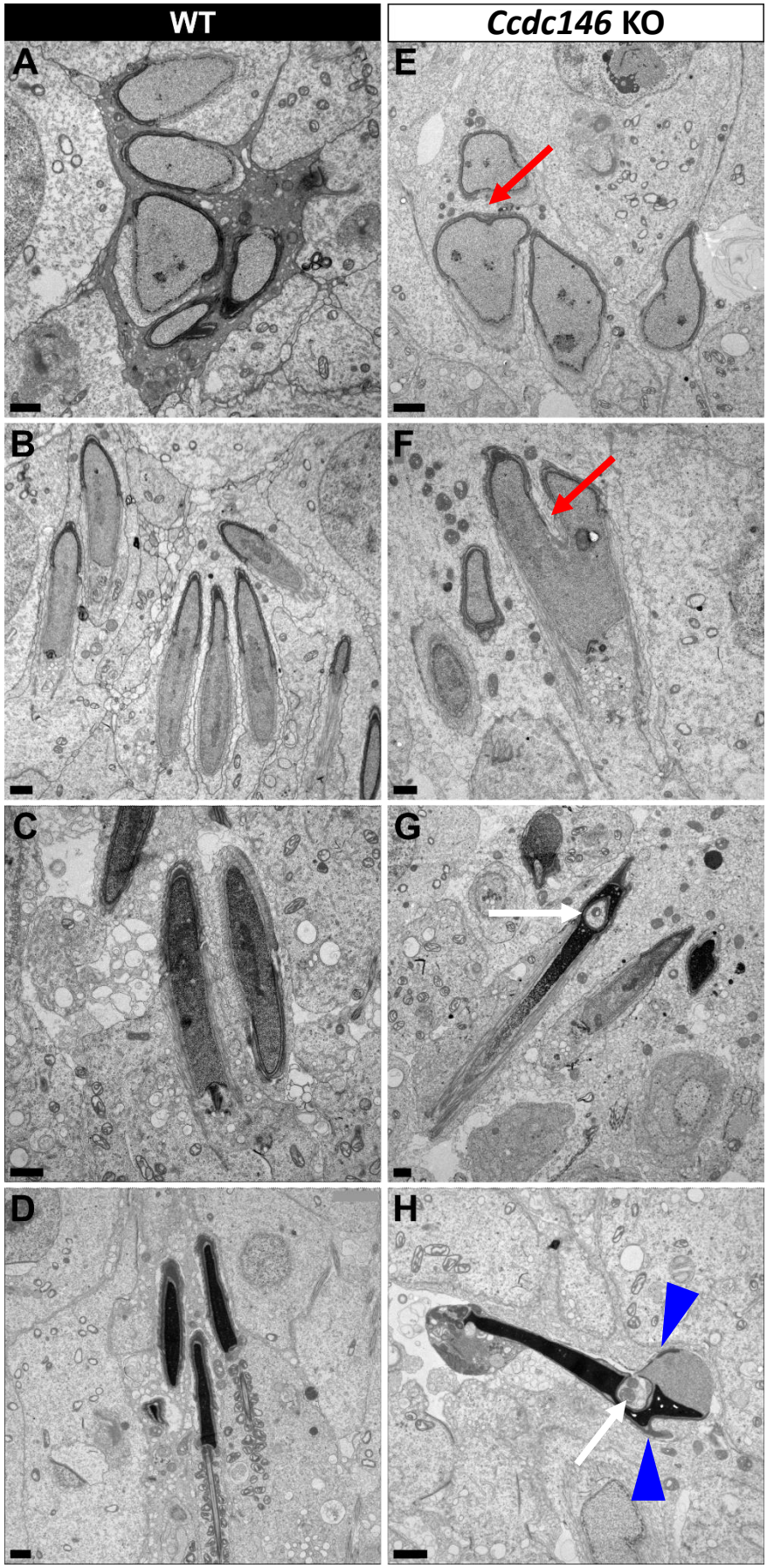

Figure 1 — Figure supplement 1 – revised version

			Semen volume (mL)	pH	Viscosity (normal:1, abnormal:2)	Sperm concentration (million/mL)	Total sperm number (million/ejaculate)	Non sperm cells/Round cells (million/ml)	Polynuclear Neutrophils	Total Motility (a+b+c) after 1h (%)	Progressive Motility (PR: a+b)	Vitality (%)	Sperm morphology : normal forms (%)	Multiple Anomalies Index (MAI)	Tapered head	Thin head	Microcephalic	Macrocephalic	Multiple heads	abnormal base (Abnormal post-acrosomal region)	Abnormal acrosomal region	Excess residual cytoplasm	Thin midpiece	Bent or misaligned tail	No tail	Short tail	Irregulary shaped tail	Coiled tail	Multiple tails
Lower Reference Limits (WHO)			**1.5**	**≥7.2**		**15**	**39**			**40**	**32**	**58**	**4**	–	–	–	–	–	–	–	–	–		–	–	–	–	–	–
	Patient ID	Age																											
CCDC146	08IF039	48	5.5	NA	2	35	193	3.2	NA	15	10	42	1	NA	NA	NA	NA	NA	NA	NA	NA	NA	NA	>10%	>10%	>10%	>10%	>10%	
CCDC146	09IF026	52	2	7.7	1	42	84	1	0	10	7	62	0	2.4	5	2	6	2	0	6	34	11	3	NA	35	37	67	18	3

Figure 1—Figure supplement 2 – revised version

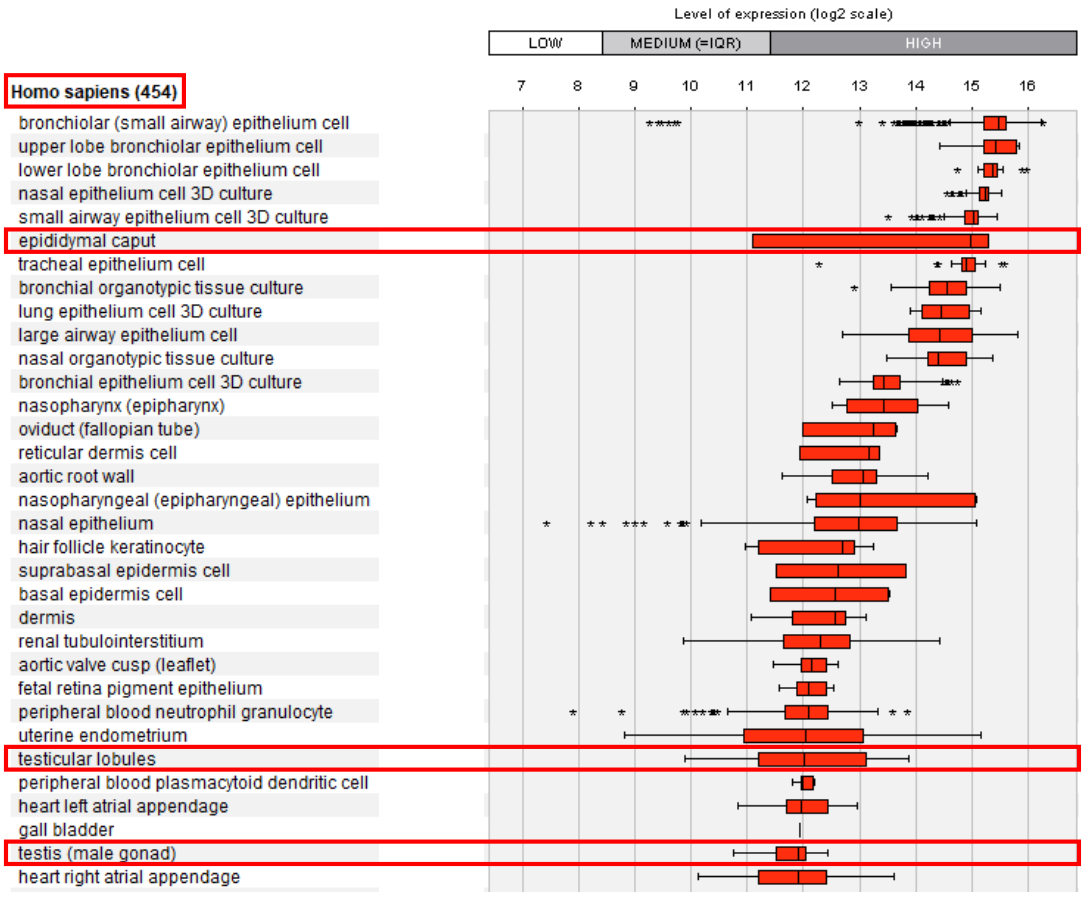

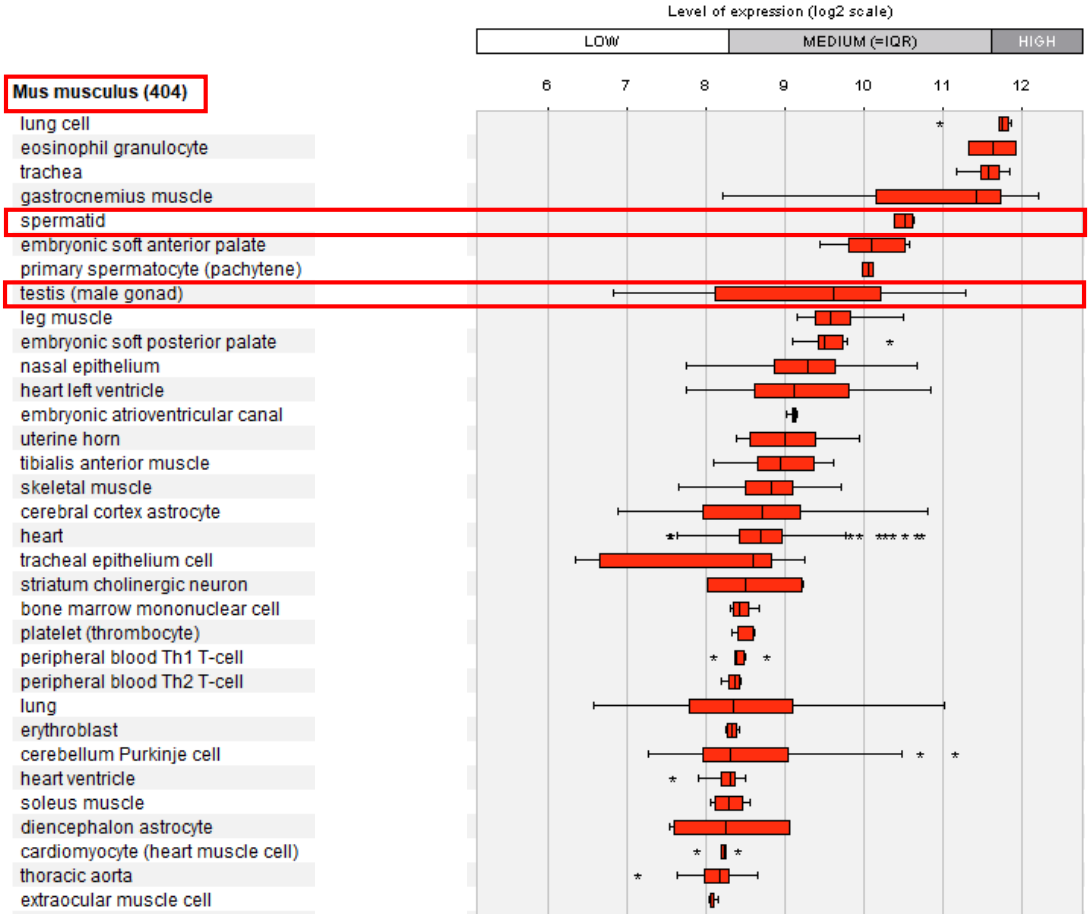

Figure 2 — Figure supplement 1 – revised version

A

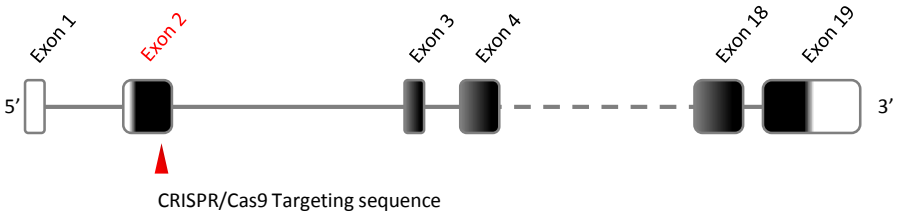

B Line 1 – Deletion 4 bp

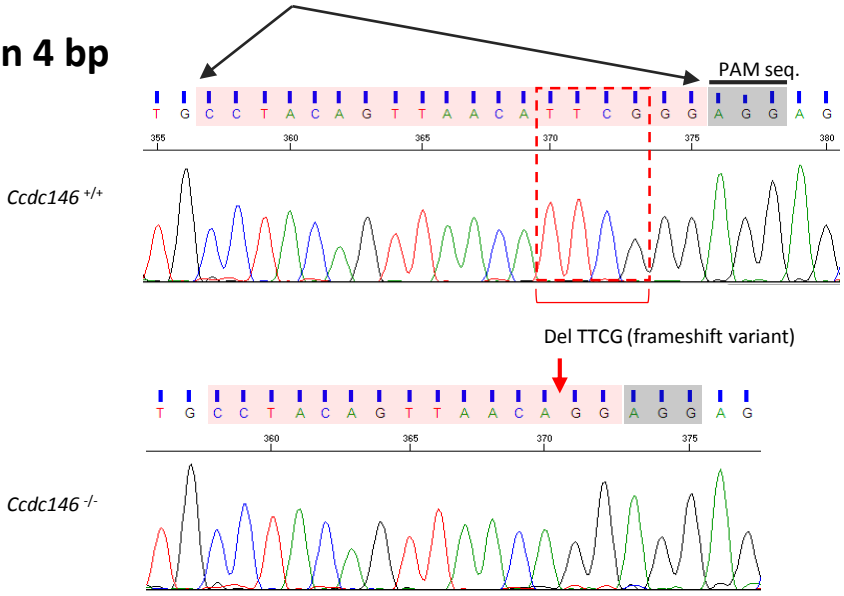

C Line 2 - Insertion 250 bp

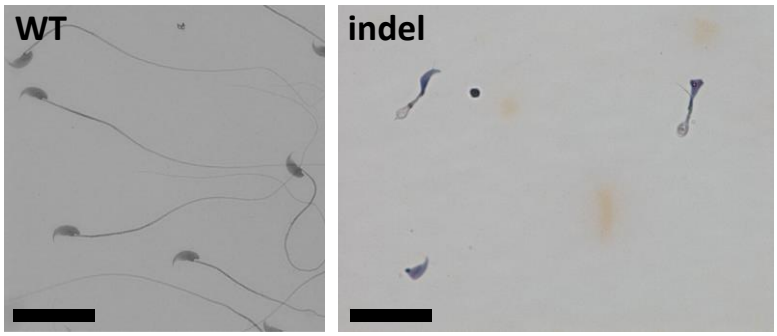

D

	Genotypes – line 2							
	WT	WT	WT	Htz	Htz	Htz	KO	KO
Sperm count (x 10^6/ml)	35	15.5	18.8	24.8	26.8	14.2	2	9.1
Vitality (%)	81.2	85.7	86.6	79.3	84.4	81.5	78.6	78.9
Progressive Motility	ND	ND	ND	ND	ND	ND	0	0
Typical forms	ND	ND	ND	ND	ND	ND	0	0
Flagellar defects	ND	ND	ND	ND	ND	ND	0	0

Figure 2—Figure supplement 2 – revised version

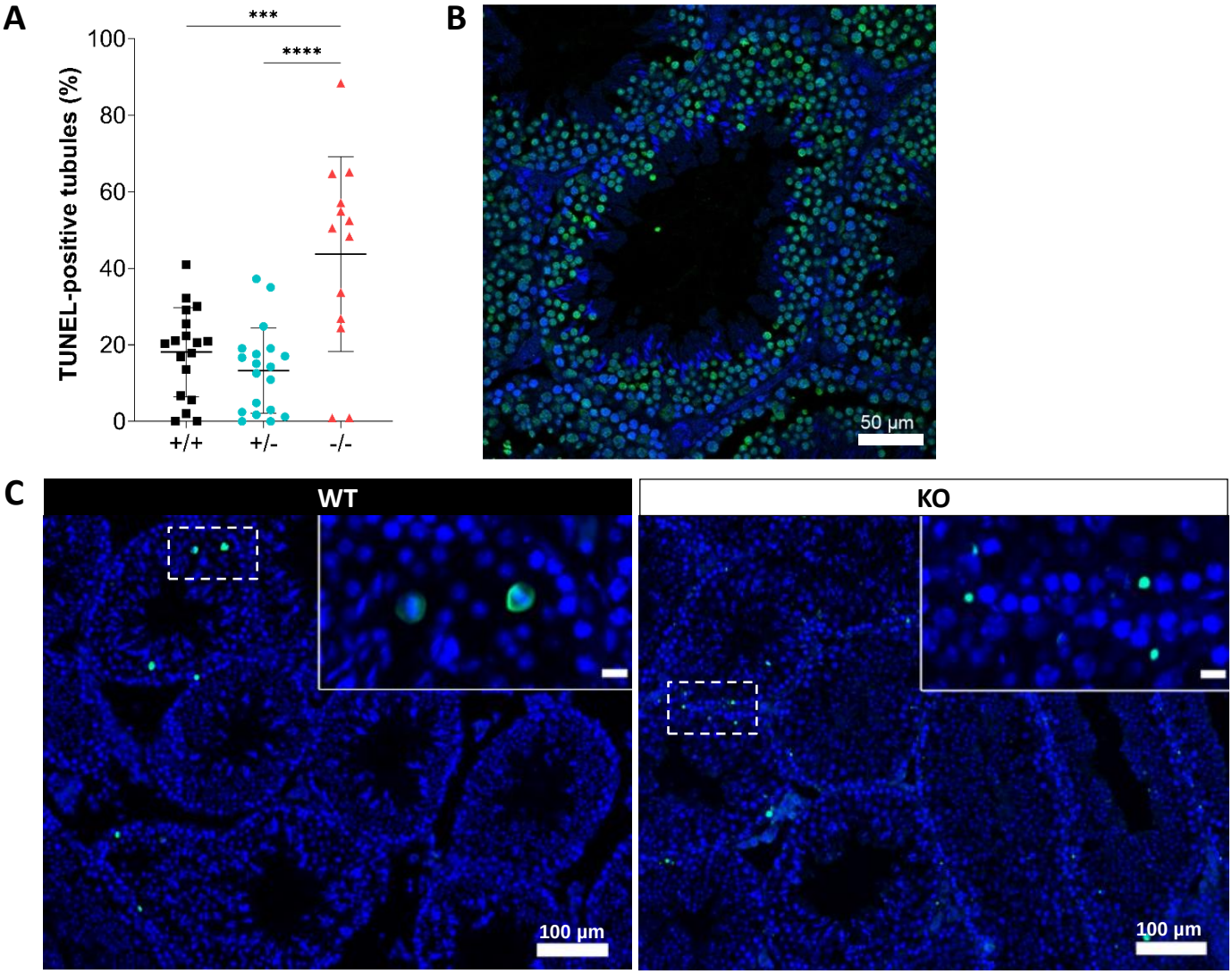

Figure 4—Figure supplement 1 – revised version

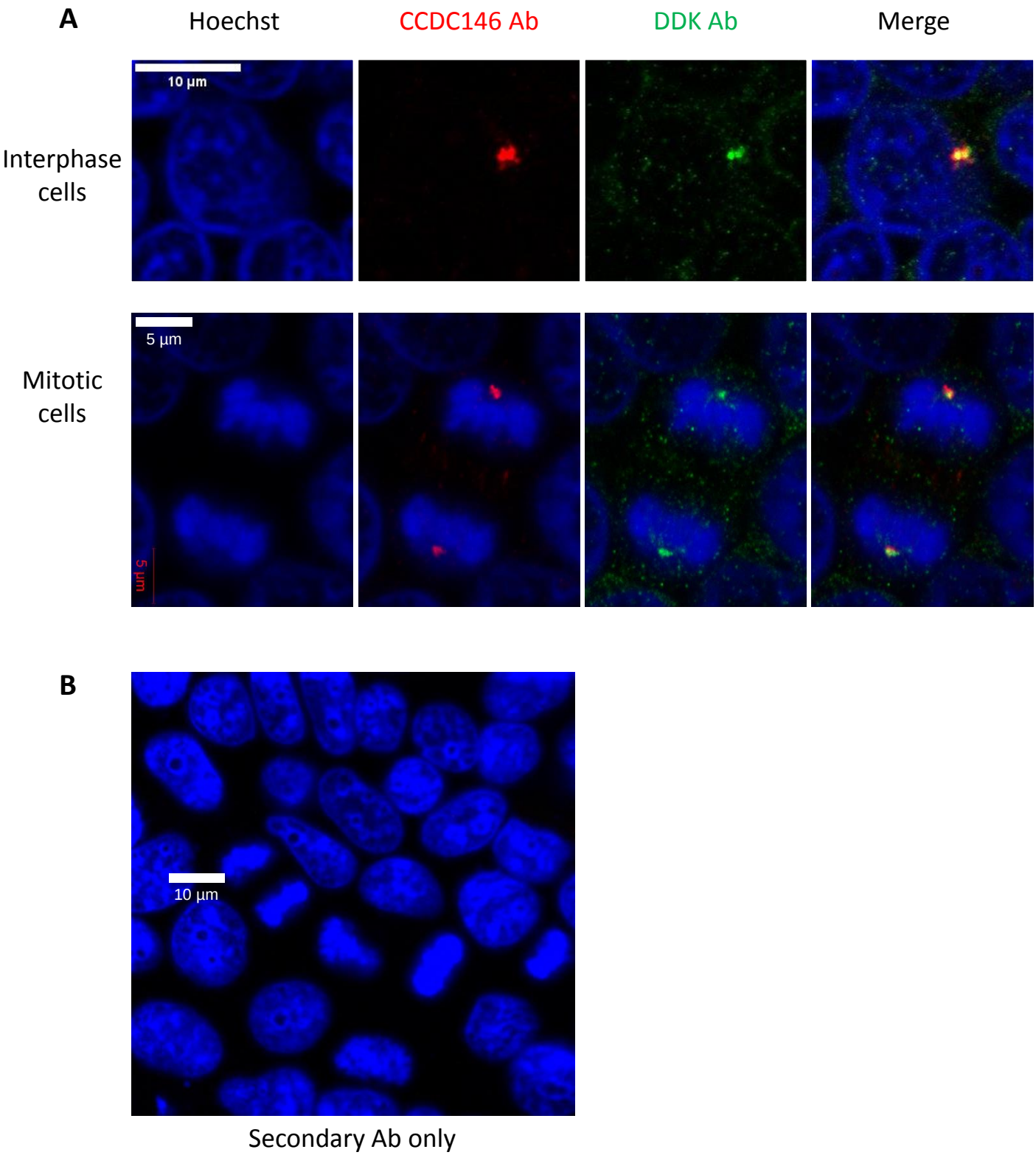

Figure 4—Figure supplement 2 – revised version

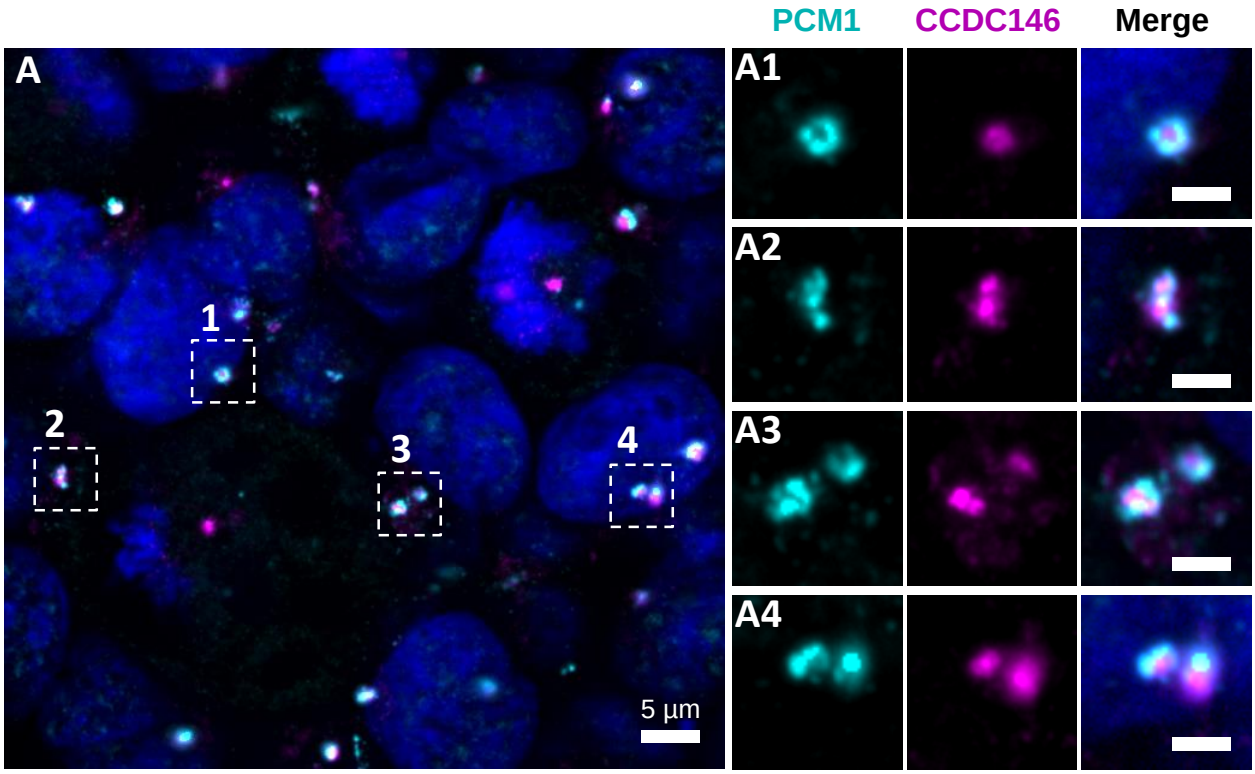

Figure 5—Figure supplement 1 – revised version

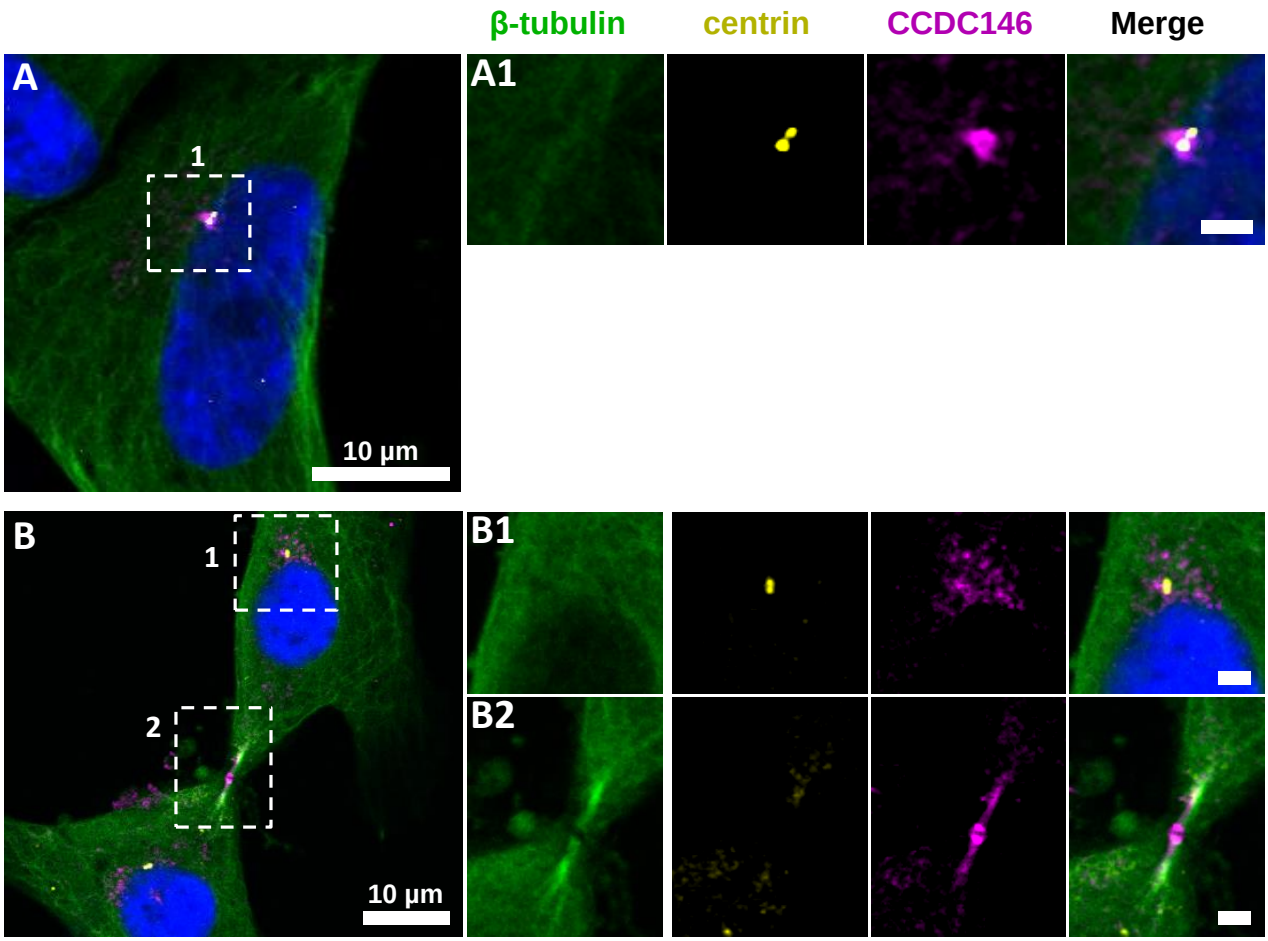

Figure 6—Figure supplement 1 – revised version

A

Strand	Sequence	PAM	On-target score	Off-target score
+	TACTTTAGAACTGTGAAAAA	TGG	27.9	29.0

B

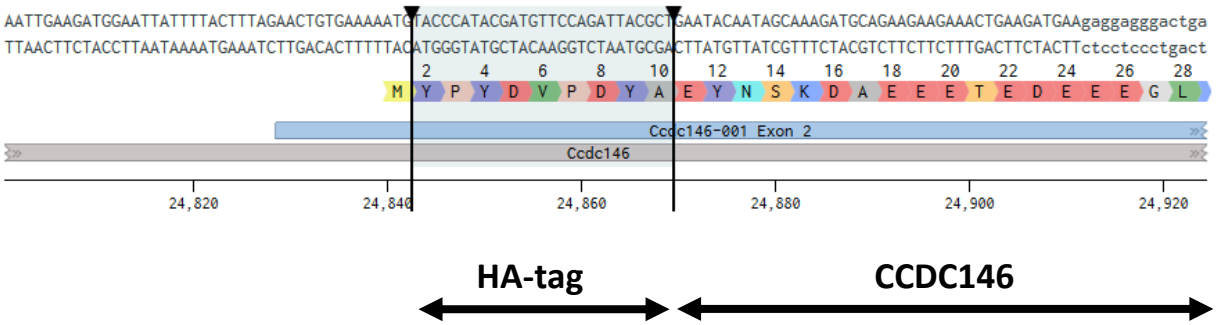

Figure 7—Figure supplement 1 – revised version

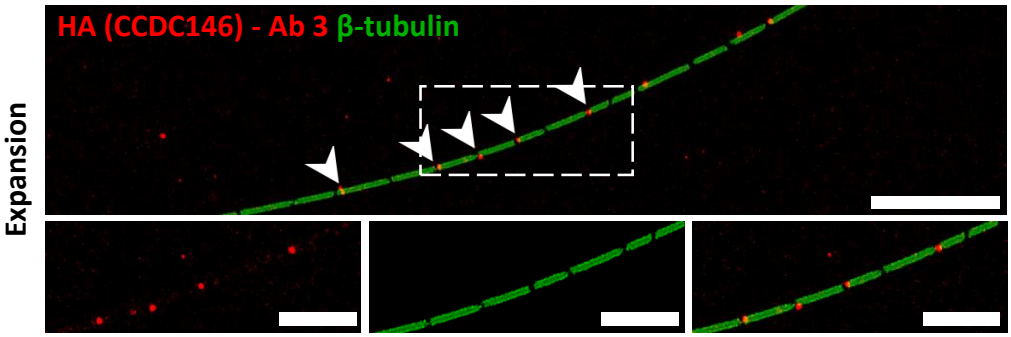

Figure 8—Figure supplement 1 – revised version

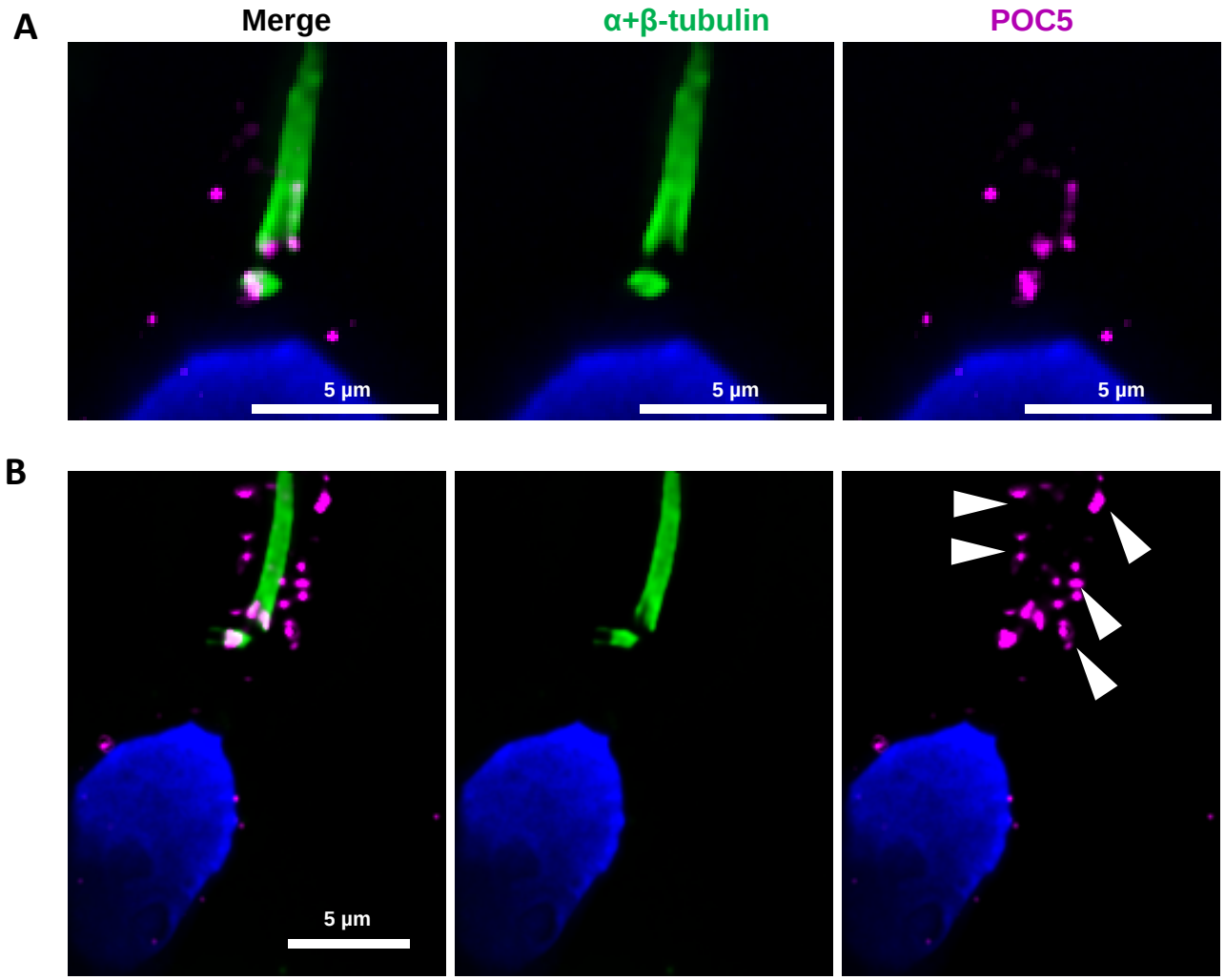

Figure 10—Figure supplement 1 – revised version

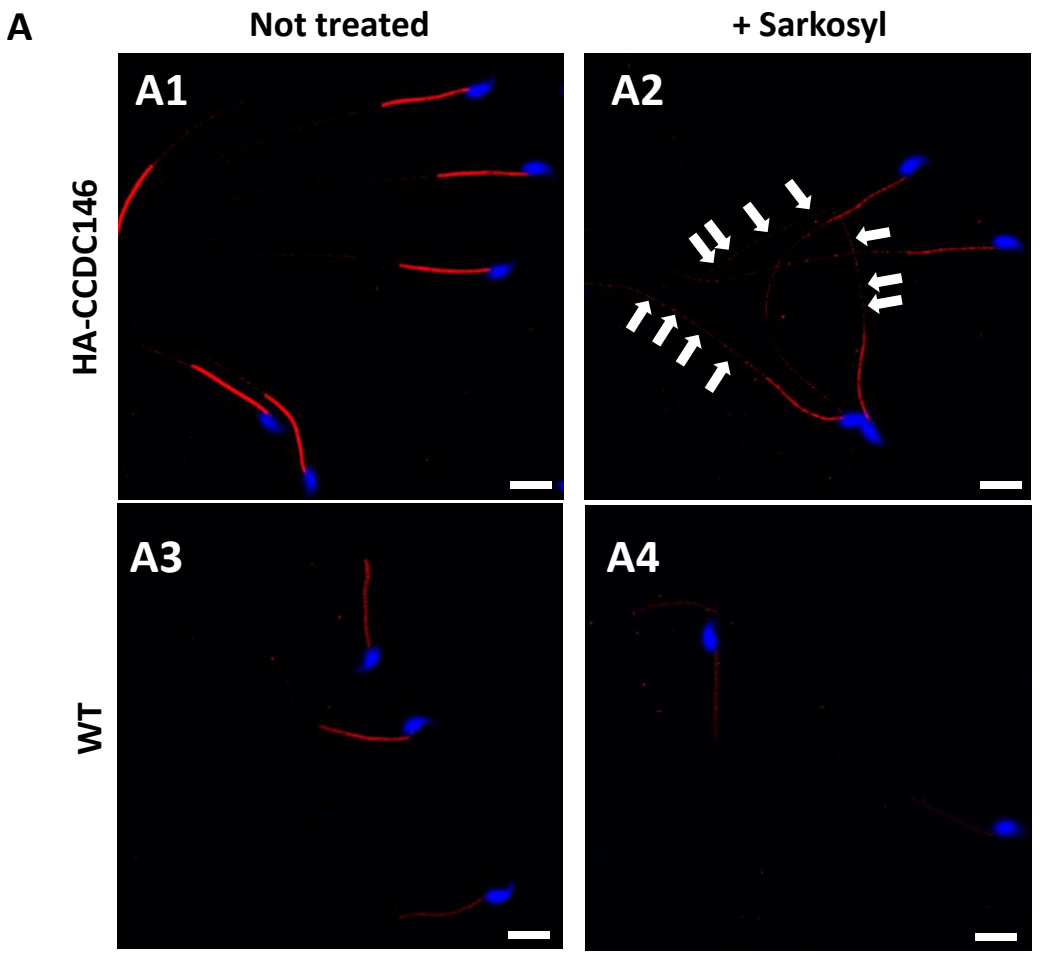

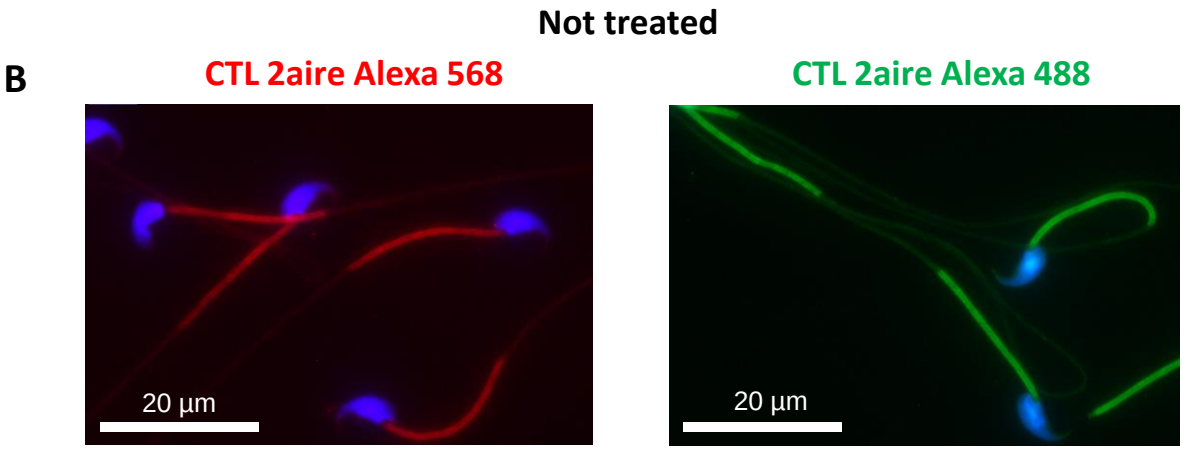

Figure 12—Figure supplement 1 – revised version

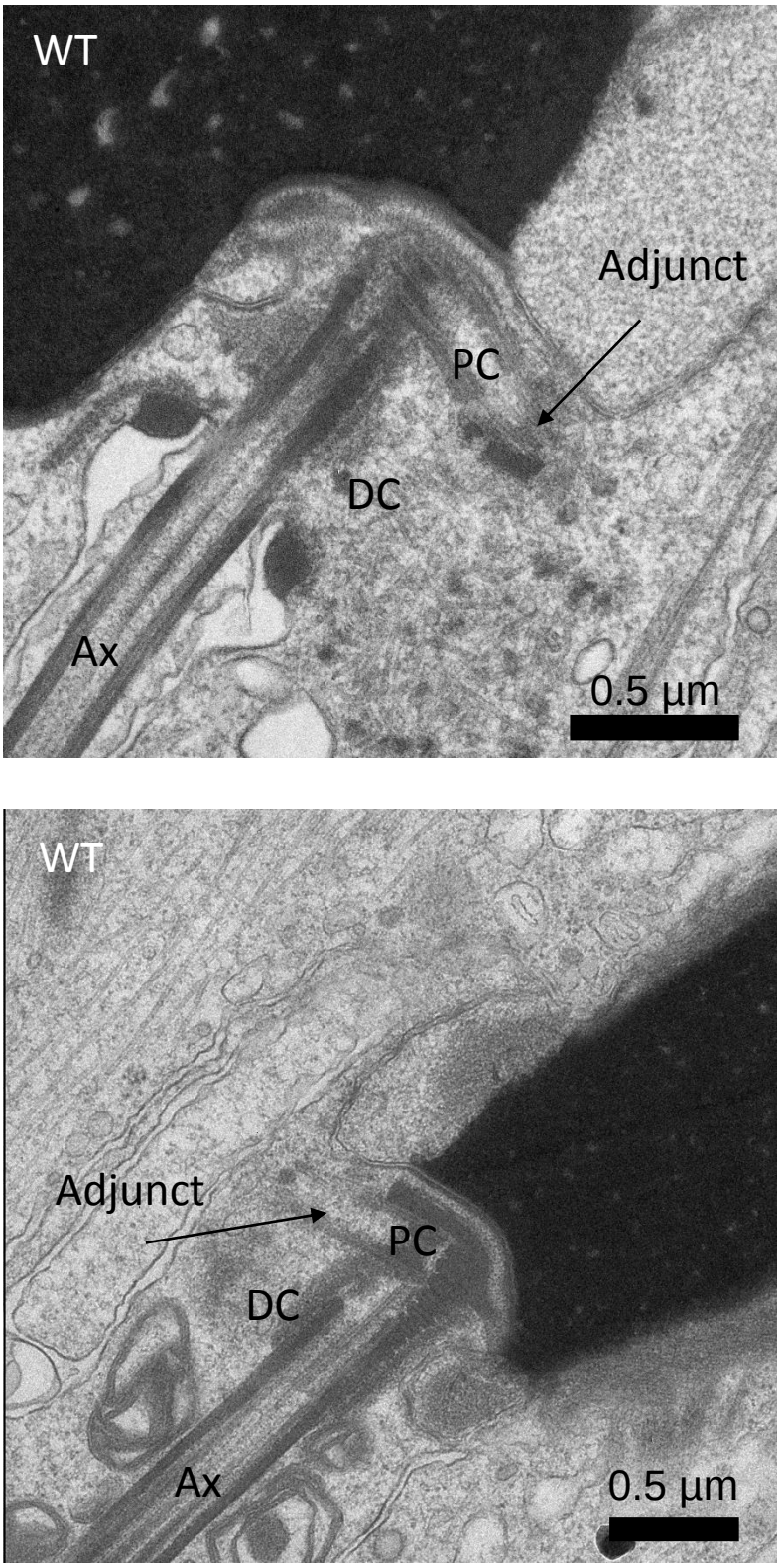

Figure 12—Figure supplement 2 – revised version

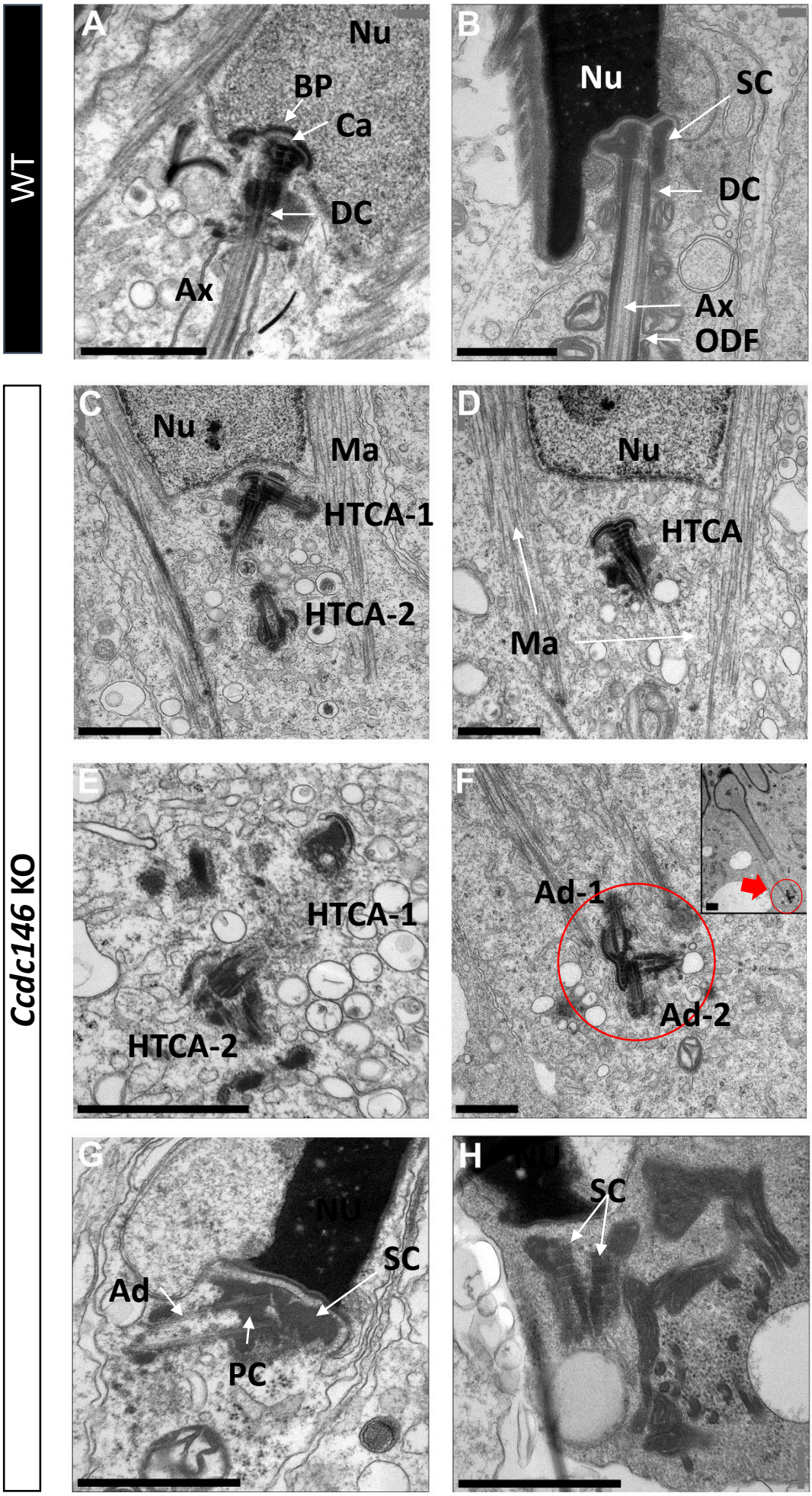

Figure 13—Figure supplement 1 – revised version

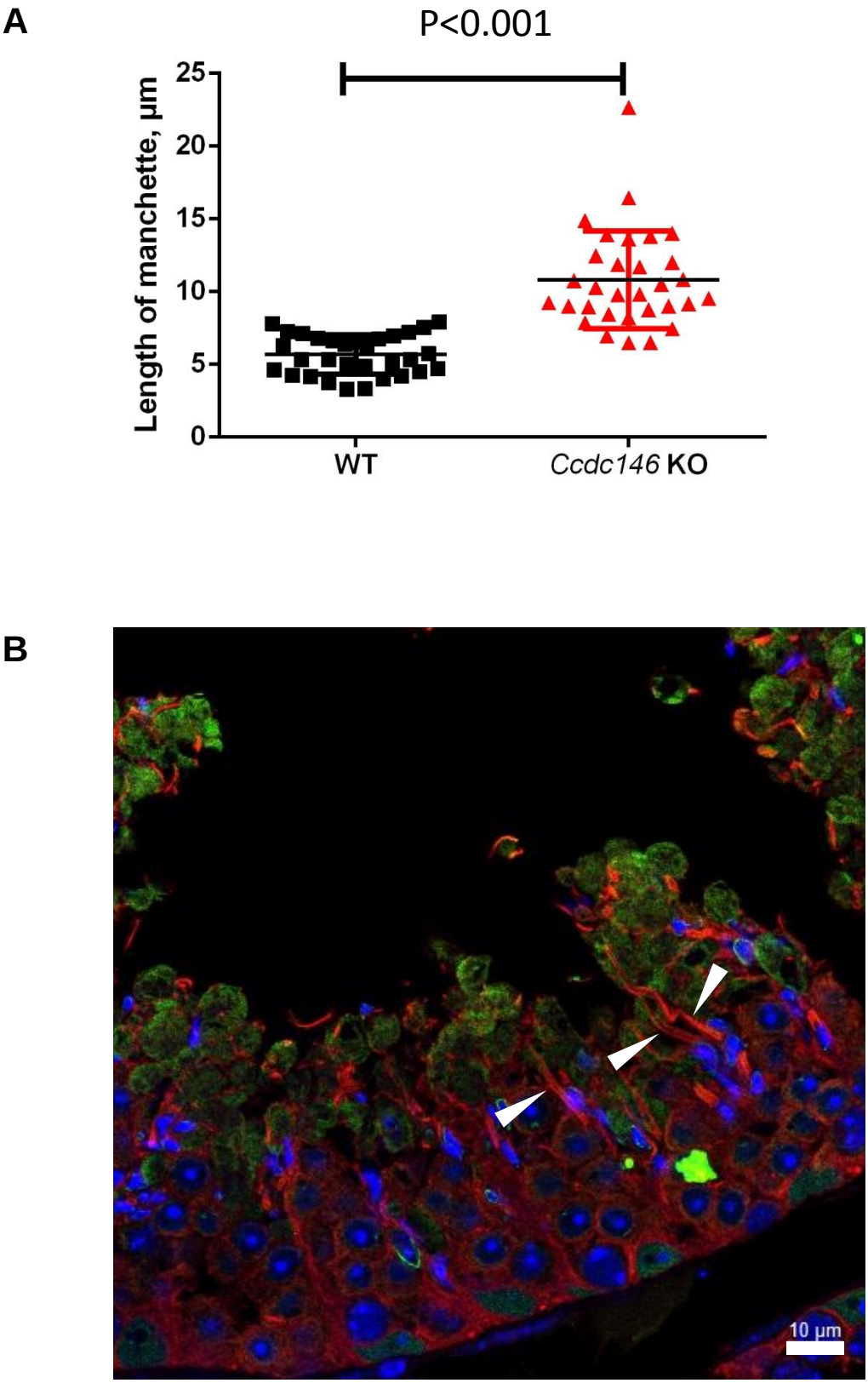
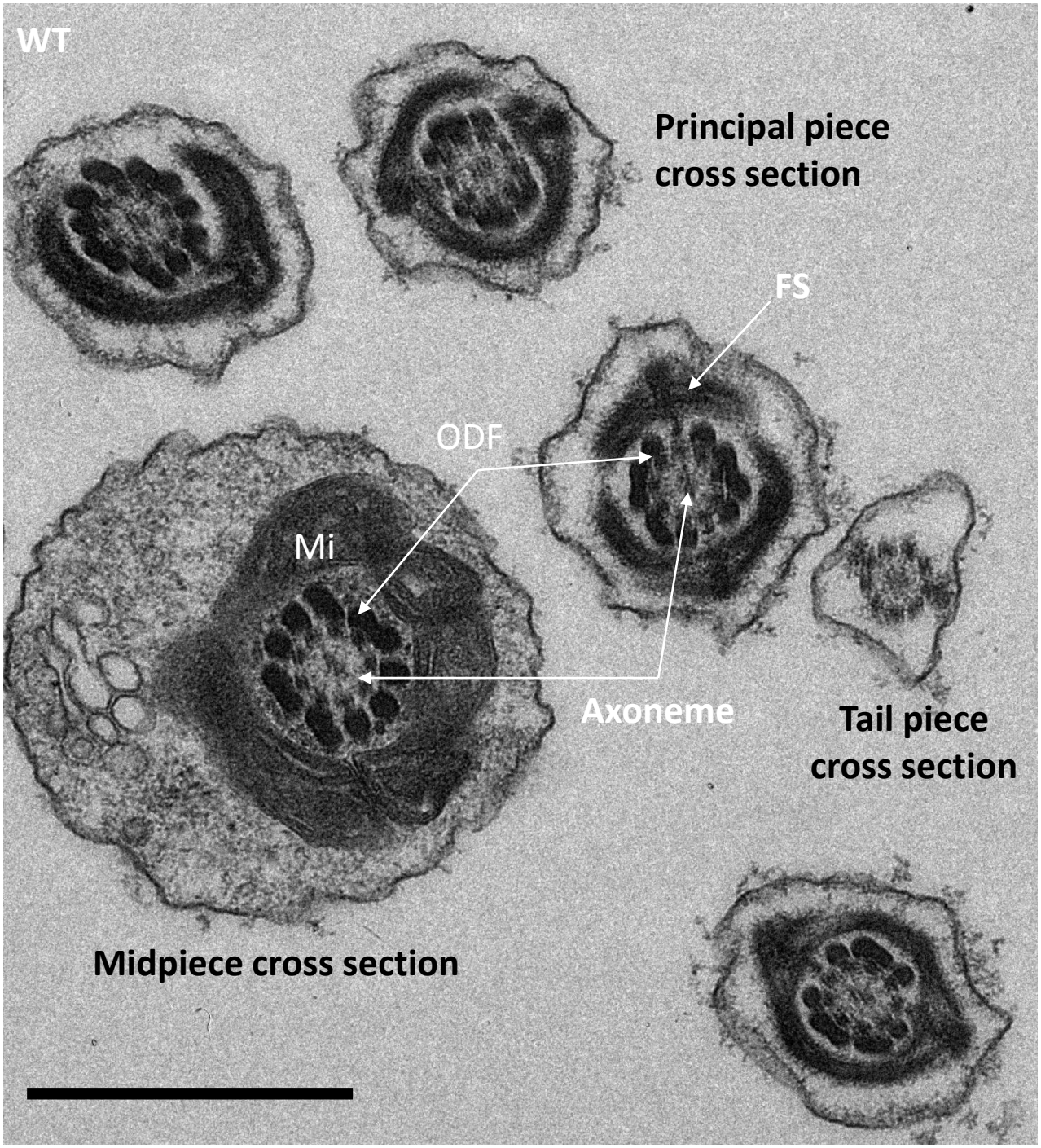
Figure 15—Figure supplement 1 – revised version